Physik Department

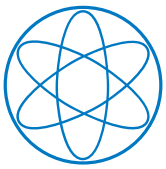

Effects of boundary conditions on cytoskeletal structure formation

Dissertation

von

Matthias Schuppler

Technische Universität München

TECHNISCHE UNIVERSITÄT MÜNCHEN

Lehrstuhl für Biophysik E27

Effects of boundary conditions on cytoskeletal structure formation

Matthias Bernhard Schuppler

Vollständiger Abdruck der von der Fakultät für Physik der Technischen Universität München zur Erlangung des akademischen Grades eines

Doktors der Naturwissenschaften

genehmigten Dissertation.

Vorsitzender: Prof. Dr. Ulrich Gerland

Prüfer der Dissertation:

1. Prof. Dr. Andreas Bausch
2. Prof. Dr. Matthias Rief

Die Dissertation wurde am 12.10.2016 bei der Technischen Universität München eingereicht und durch die Fakultät für Physik am 30.12.2016 angenommen.

Summary

Cells that compose living tissue are subjected to a multitude of mechanical challenges. They have to ensure an enormous degree of flexibility in fulfilling various functions as complex as cell locomotion or division. Essential for all of these processes is, that cells are able to actively exert and resist forces. The arising bandwidth of tasks is met by a highly complex composite network, built from three basic types of filamentous biopolymers: actin filaments, intermediate filaments and microtubuli. Each sort exhibits unique properties and is complementary involved to account for the immediate, cellular need.

The actin cytoskeleton is a protein polymer network regulated by a plethora of auxiliary proteins that crosslink, nucleate, sever, elongate or cap filaments into different microstructures. Additionally to the dynamics arising from polymerization and degradation of filamentous actin, molecular motors introduce an active, ATP fueled component, that accounts for flexible remodeling. While basic functions of the interplay between molecular motors and filamentous actin have been identified in *in vitro* assays with well defined reconstituted systems, it is still elusive how cells regulate their heterogeneous cytoskeleton in space and time. Despite the importance of these force-generating systems the microscopic mechanisms and their consequences are not well understood.

The goal of this thesis is to shed light on the regulatory potential of a boundary to the organization of cytoskeletal networks.

To this end in the first part of the thesis I developed a reconstituted active actin network comprising actin and molecular motors, where the local activation of myosin can be controlled by light. The subsequent driving of the actin filaments results in contraction of the actin scaffold, that maintains a stable connection to the unactivated passive and viscoelastic surrounding. By activating different geometries, it is shown, that only the force balances at the boundaries of the specific

geometry determine the global shape changes. The information of the initial force imbalance at the boundary penetrates the network during the onset of contraction and consequently the dynamics of the contraction is set by the length of the shortest axis of the geometry. Spatially anisotropic attachment of initially isotropic networks leads to a self organization of highly aligned contractile fibers, that are reminiscent of the order formation in muscles or stress fibers. The observed shape changes and dynamics are fully recovered by a minimal physical model: motor rearrangements are modeled by the release of elastic energy, that has been initially stored in a discrete grid of connected harmonic springs of uneven spring coefficients. The transition from initial to final configuration is fully described by the topology of the initial grid and the choice of the activated area. The temporal evolution can be accurately recovered by critical damping of the network‘s constituents.

Besides the regulation of contractility due to the release of motor activity in spatially well-defined macroscopic arrays (in cells often realized by phosphorylation of key proteins), essential cellular rearrangements of the cytoskeleton might be governed by a much simpler machanism. The results presented in chapter 4 suggest, that the attachment to a stiff boundary can act as a direct regulator of global actomyosin contractions. There, the forces sustaining at the boundaries of an active network provide resistance to internal dynamics and even arrest all contractile rearrangements. In the assay the presence of biochemically engineered crosslinkers both tunes the network elasticity and connectivity to match the motor activity and serves as attachment points to maintain a stable force balance at the boundary. Local detachment of the active network leads to an altered force balance at the boundary, allowing the motors to contract the actin scaffold towards its center of mass. This simple mechanism identified here might enable cells to control their contractile activities in space and time via the attachment to their surroundings.

The control and the characterization of force balances at the boundaries of reconstituted cytoskeletal systems are important to understand the underlying mechanisms of dynamic reorganization. The physiological boundary of the living cell is its plasma membrane. Together with the underlying cytoskeleton it accounts for numerous morphological transformations including blebbing, invagination and

adaption to different kinds of external stimuli. The mechanical properties of a plasma membrane can be reconstituted by a double layer of lipids forming a vesicle. A footprint of the force balances occurring at such a bilayer, can be derived by the measurement of the apparent membrane tension. To this end I assembled a custom optical tweezers setup, which allows to pull a lipid tether and simultaneously measure the applied force.

The instrument is used in a second set of experiments to address self-assembly mechanisms present in filopodial structures. In a reconstituted assay directed actin filament growth with and without the addition of the bundling protein fascin is investigated. By this means, it is shown how crosslinks locally stiffen actin networks and consequentially terminate polymerization.

In summary, in the frame of this thesis the role of boundary as a key regulator for active cytoskeletal networks that play an essential part in cellular dynamics has been investigated. This paves the way to increasing the complexity of reconstituted cellular systems and on the long run to reconstitute elementary cellular behavior like stress fiber formation or cytokinesis in a bottom-up approach. Furthermore the ability to access forces generated in vesicle confined geometries may lead to identification of the physical mechanisms for shape transformations and set a quantitative benchmark for further exploration of cytoskeletal mechanics.

Contents

1 Introduction

Eukaryotic animal cells lack a rigid cell wall, which controls the shape of some bacteria or plant cells. Instead this capability is provided by their cytokeleton, a complex filamentous network system, comprising only a few types of proteins able to assemble into polymeric structures, but a plurality of auxiliary proteins, which orchestrate these biopolymers to meet the immediate requirement of the cell.

Three basic types of polymers can be classified: microtubuli, intermediate filaments and actin filaments. While microtubuli are predominantely engaged in the mechanical connection of the core structures with the cellular periphery, e.g. intracellular organelle transport Hirokawa [1998], apolar intermediate filaments are required to maintain the cellular shape. Actin filaments are essential for a striking plethora of cellular functions, ranging from locomotion to cytokinesis Mitchison and Cramer [1996], Pollard and Borisy [2003], Pollard and Cooper [2009]. They exhibit internal dynamics and are structurally and mechanically adaptive, dependent on the deployed auxiliary protein.

Actin serves as a track for molecular motors like muscle or non-muscle myosin II, that generate additional dynamics. Historically, contractions of the actin scaffold by muscle myosin II has been investigated thoroughly in striated muscles, where these proteins are organized in sarcomeric structures. However, the sarcomere is a relatively young evolutionary product. Since both actin and myosin have evolved millions of years before, this suggests that different modes of actomyosin contractility must exist Steinmetz et al. [2012]. In particular, this conservation of the molecular components and the presence of contractile actin arrays in non-muscle cells indicates, that the physics of contractile force transmission can exhibit significant differences compared to the muscle Ridley [2011], Murrell et al. [2015], Mogilner and Keren [2009], Blanchoin et al. [2014].

In non-muscle cells contractile arrays are embedded and constantly attached

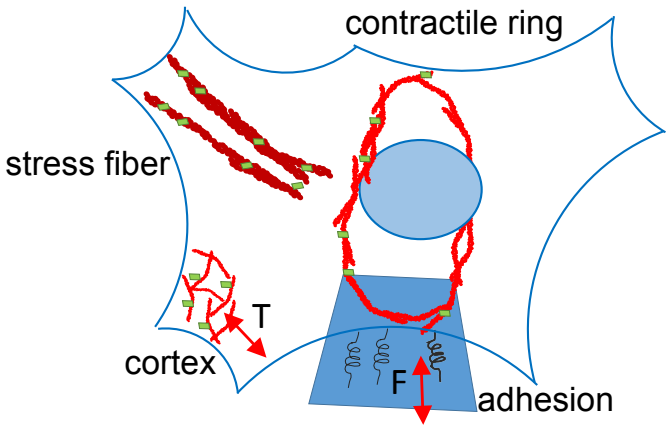

Figure 1.1 **Schematics of contractile actomyosin structures *in vivo*.** The actin scaffold (red) is arranged in varying microstructures, myosin is depicted in green and the nucleus and the plasma membrane in blue.

or connected to their biological environments, see Fig. 1.1. Actin and non-muscle myosin in the cellular cortex must be tightly regulated to account for shape change, such as observed in cytokinesis Robinson and Spudich [2004], Vavylonis et al. [2008]. The mechanochemical stresses within the cortex not only account for large shape changes but are also involved in locating endocytosis and the aequatorial plane before cell division Ungewickell and Hinrichsen [2007]. The current knowledge of the mechanical properties of cytokeletal polymers does not suffice in providing a sound mechanical characterization of how the cell resist and exert forces.

In cells the attachment of the contractile structures to adhesion sites or the anchoring within the cortex are key for their assembly and function, yet it is still unclear if such boundary conditions would be already sufficient to drive the formation of contractile cellular modules Murrell et al. [2015], Thoresen et al. [2013].

A substantial physical understanding of these underlying processes is often handicapped by the simultaneous involvement of numerous and even potentially unknown proteins. To overcome this dilemma it is possible to study reconstituted *in vitro* systems, where type and concentration of the proteins as well as the buffer

conditions are well defined.

A minimal model system consisting of actin filaments, crosslinkers and myosin-II motor proteins exhibit *internal* driving, which leads to remarkable self-organization and pattern formation. In these systems the microscopic details of competing force generation (myosin) and stabilization (crosslinkers) account for large scale structure formation. For instance the binding affinity of myosin-II motors to the crosslinked actin structures, which can be tuned by pH or ionic strength of the surrounding medium, sets the maximal force a motor filament can exert Köhler et al. [2012]. If this force is sufficiently high to deform or disrupt (crosslinked-) actin structures, the behavior of the system is dominated by the motor activity.

The architecture of F-actin networks determines how forces generated by myosin motors are transmitted. The number and the type of crosslink determines the connectivity, an important parameter for active networks. This connectivity is a measure of the length scale on which actin structures are physically coupled to each other. Within highly connected and elastic systems, by pulling against crosslinks motors generate tensile stresses, which changes the elastic properties of the network Koenderink et al. [2009] and eventually leads to global contraction in the purely viscous surrounding Bendix et al. [2008].

In the opposite case of weakly connected network, motor-induced rearrangements result in static or dynamic clusters Köhler et al. [2011], Smith et al. [2007], Backouche et al. [2006]. The activity of these heterogeneous systems depends on its connectivity, as molecular motors need tracks on which their forces can pull. A sensitively tuned balance between motor forces and binding strengthes within the actin structures is necessary to maintain a connectivity in networks, which accounts for superdiffusive dynamics or collective modes of actin clusters. Tuning initial connectivity of these active systems reveals a robust critical regime, separating between global and local contraction Alvarado et al. [2013].

Each rupture and fusion event alters the attachment of actin clusters to their neighbors and consequently the local visco-elastic environment of each actomyosin structure constantly changes. It remains elusive how the creation of a boundary itself affects the shape change as well as the dynamics of contractile actin arrays. The aim of this thesis is to address the following points to gain insight into the regulatory potential of elastic boundaries for contractile active gels.

1. To shed light on the principles underlying the physics of such active gels, it is mandatory to design appropriate **minimal model systems**, that allows to study the regulatory mechanism of a well-defined connection between active and passive components. It should allow a tight control of the relevant parameters in the system.

2. This well-controlled assay should provide the framework for a **detailed analysis** of dynamics and to dissect the relevant properties governing the active **self-assembly process**.

3. *In vivo*, increase of tension and alignment in myofibrillogenesis has been observed with correlated actomyosin activity and concerted attachment of the filamentous structures Weitkunat et al. [2014]. This raises the question whether the precise **control of the attachment** of contractile structures could play an essential role in such rather complex cell behaviors.

4. A main feature of active actin networks is their ability to contract macroscopically. For cellular rearrangements this needs to be regulated not only in space but also in time. A complex machinery ensures *in vivo* the assembly of highly dynamic steady state structures ready to induce large scale rearrangements on rather small perturbations. So far, mainly biochemical pathways of regulation, as the phosphorylation of key proteins, are in focus of research. However, for essential cellular processes including actomyosin activity, there might be different, simple and generic mechanisms. Recent investigations found evidence that force imbalances at the cell periphery can act as trigger for actomyosin activity Yonemura [2011], Ren et al. [2009]. A possible mechanism could be global arresting of myosin based contractions by attachment of the active arrays to their boundary. In chapter 4 it will be shown that global contraction of actomyosin gels can be arrested by sensitively tuning attachment to a biochemically modified interface. Induced **local detachment of the active gel entails contractility**.

5. There are numerous kinematic assays to dissect cytoskeletal mechanisms. Provided by real time microscopy, they deliver information on changing shapes, sizes and positions. Nevertheless the full mechanical picture can

only be obtained by the measurement of dynamical properties as forces, tension and elasticities. As a matter of fact, for contractile networks the measurement of transient properties is rather challenging and beyond the capabilities of (micro-)rheology. To this end a custom optical tweezers setup 2.2.7 is constructed and characterized to be able to measure forces of (active) actin gels in the confinement of a vesicle. In a first set of experiments it is used to **form a lipid tether of vesicles** solely containing aequous solution, see chapter 5.

6. During cellular migration regulated, anisotropic, actin network assembly takes place at the leading edge of the cell Schafer [2004], Pollard and Borisy [2003]. During locomotion cells produce thin and sheet-like structures, the *lamellipodia*, and long thin spikes, called *filopodia*. Together with Carina Pelzl the mechanisms underlying the formation of these structures are studied by a microrheological assay, measuring the local properties of anisotropic actin networks, which has been grown from a surface 6.

2 Materials and Methods

2.1 Proteins

2.1.1 Actin

The globular protein actin is among the three major biopolymers of the cytoskeleton present in nearly every eukaryotic cell - the only so far known exception is the nematode sperm cell Roberts et al. [1989] - and has a molecular weight of 40-45 kDa depending on the species. It fulfills numerous tasks, including intra- and intercellular transportation, cell motility and provides the mechanical stability for the cell to withstand extracellular stresses.

The actin protein used here is purified from rabbit skeletal muscle by a modified protocol of Spudich and Watt [1971]. An additional gel filtration (Sephacryl S-300 HR) step is done MacLean-Fletcher and Pollard [1980]. The G-Actin is stored in G-buffer (2mM TRIS, 0.2mM $CaCl_2$, 0.2 mM DTT, 0.005% NaN_3 at pH 8) at 4°C and used within two weeks. To account for variations of the purification yield and to guarantee comparable assay buffer conditions G-Actin is prediluted to $20\mu M$ in the same buffer. Polymerization is initiated upon addition of 10% volume of 10x AB-buffer (250 mM Imidazole 40mM $MgCl_2$, 10mM EGTA, 2mM ATP, 20mM DTT, 250 mM KCl, pH 7.5) and gentle mixing. Consequently G-Actin assembles to helical filaments with a period of 72 nm of 26 monomer subunits Bullitt et al. [1988] and a persistence length $l_P \approx 15\mu m$. Thereby individual F-actin filaments can grow up to lengths of $100\mu m$, forming an entangled and percolating meshwork.

2.1.2 Phalloidin and dyes

Phalloidin is a small molecule of 789 Da, which is extracted out of the fungus *death cap* or *Amanita phalloides*. It can only bind to actin in its polymerized form and stabilizes the filaments against depolymerization. Phalloidin can be conjugated with numerous dyes, tailored to the spectral requirements of the assay. In this work we use Alexa-647 in chapter

2.1.3 Anillin

Anillin is a protein that is able to link myosin II, F-actin and septins and is thought to play an important role during cytokinesis Zhang and Maddox [2010], Maddox et al. [2007]. Here, a fragment of *Xenopus laevis*, spanning amino acids 1-428, is cloned into pET-28a and purified from E.coli with His-tags on N- and C-termini. This fragment has been shown to bundle F-actin. After purification anillin is stored in 25mM imidazole, 25 mM KCl, 4mM $MgCl_2$, 1mM EGTA, 1mM DTT at -80°C

2.1.4 Fascin

Fascin is a monomeric 55 kDa actin bundling protein, which crosslinks actin into thin bundles of maximal about 20 actin filaments Claessens et al. [2008]. *In vivo* fascin is localized to filopodia and filopodia-like structures Vignjevic et al. [2006]. Here recombinant human fascin is purified from *E.coli* BL21 according to the method of Ono et al. [1997] as described in Vignjevic et al. [2003]. It is stored in 2mM Tris (pH 7.4), 150 mM KCl at -80°C

2.1.5 Capping Protein

Capping protein is a heterodimeric protein consisting of a 33 kDa α-subunit and a 31 kDa β-subunit. It binds to the barbed ends of actin, thereby fulfilling two functions. First it inhibits filament elongation of the barbed end Kilimann and Isenberg [1982] and activates nucleation of actin filaments Schafer et al. [1996]. Consequently in presence of capping protein the length distribution of actin filaments gets altered. Secondly, together with profilin it maintains a large pool of

unpolymerized actin monomers Kovar and Pollard [2004]. After purification it is dialyzed against 10mM Tris (pH 8.0), 50 mM KCl, and 1mM DTT and stored at -80°C.

2.1.6 Profilin

The abundant protein profilin cooperates with capping proteins to supply the cell with sufficient monomeric actin. At sufficiently high ratio to actin, Profilin inhibits actin polymerization at the pointed end, by binding to the barbed end of actin monomers. If profilin-actin complex binds to a barbed filament end, profilin rapidly dissociates, thereby promoting barbed end growth Pollard et al. [2007]. Here, mouse profilin 2 (mPFN2a) is expressed with GST-Tag in *e.coli* cells. The construct is purified, flash-frozen and stored at -80°C in 50mM Tris (pH 7.0), 150mM NaCl, 1mM EDTA and a mM

2.1.7 Formin

Dependent on the organism the properties of formin vary significantly. All formins contain the two formin homology domains FH1 and FH2. The proline-rich FH1 domain binds profilin, which is essential for the actin elongation mechanism *in vivo*. The FH2 domain is responsible for binding actin and thus sufficient for nucleation of f-actin Romero et al. [2004]. Together with profilin it accelerates barbed-end elongation Kovar and Pollard [2004], Kovar et al. [2006]. Here a mouse formin fragment (mDia1) with full FH1 and FH2 domain (549-1255) is recombinantely expressed in *e.coli*, purified and stored at -80°C.

2.1.8 Myosin II

Myosins are a large family of ATP-hydrolyzing motor proteins, that are responsible for force generation in cells. While non-muscle myosin plays an essential role in fundamental cellular processes, like migration and cytokinesis, (conventional) myosin-II drives contraction in muscular sarcomeres.

Myosin II is a non-processive motor: Upon binding of ATP, the motor‘s head domain detaches from actin and the ATP is hydrolyzed. This leads to a confor-

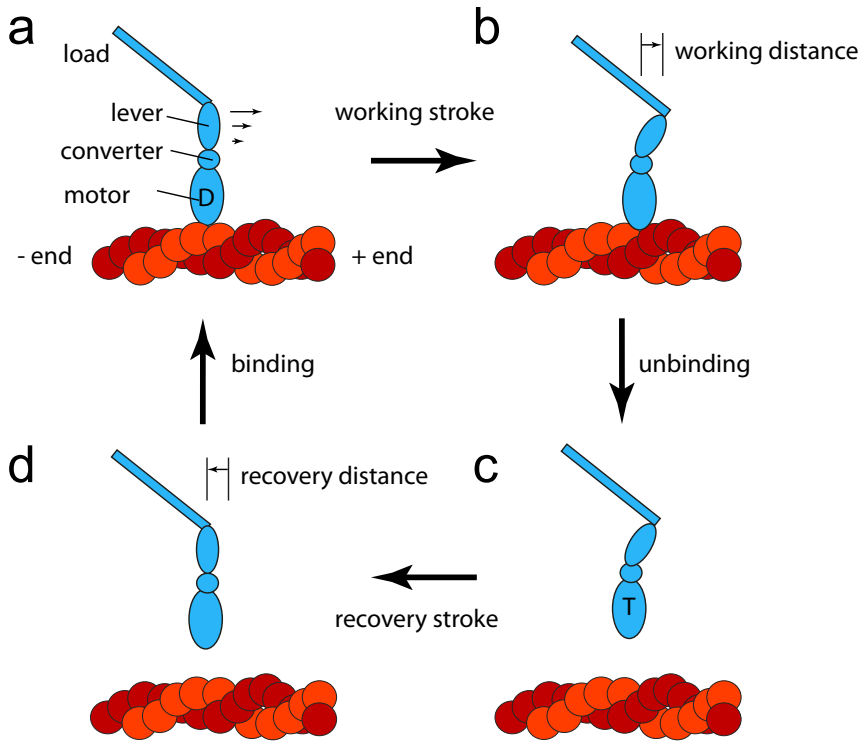

Figure 2.1 **The crossbridge model for myosin II: (a)** The release of phosphate results in a strained conformation of myosin, which gets released by the power or working stroke. The nucleotide-free myosin-II motor protein gets released upon binding of ATP. Hydrolysis of ATP results in a change of conformation, referred to as recovery stroke, as well as a rebinding to the actin filament at a position 5 nm closer to the barbed (-) end. This chemomechanical cycle of myosin-II leads to the relative movement of F-actin to myosin.

mational change of myosin-II. Its ADP·P_i state rebinds to actin at 5 nm closer to the barbed end of the actin filament than the initial position. Upon release of the phosphate a conformation strain is built up, which gets released in a conformational change to the initial conformation. This conformational change is called *power stroke* and results in a relative translocation of the F-actin and the myosin-II motor past each other, see Fig. 2.1. The conformational switch can occur up to 100 times per second Brenner and Eisenberg [1986]. This would result in a maximal sliding speed of 0.5μm/s. However, since myosin-II has a low duty ratio of ≈ 0.02 Uyeda et al. [1990], it is bound to actin only a small fraction of time. This allows

a simultaneous movement of a single actin filament by multiple myosin-II heads. This parallelization results in a maximal velocity of about 8μm/s

Skeletal muscle myosin-II gets isolated from rabbit skeletal muscle Margossian and Lowey [1982] and stored in 0.6 M KCl , 2mM $MgCl_2$ 2mM DTT, 10 mM KH_2PO_4 at -80°C.

2.1.9 Keratin

Keratin is a representative of the intermediate filaments family, which is believed to protect epithelial cells from lethal stresses. It provides the toughness and strength essential for many different parts of living organisms, including hair, nails, horns or even the tongue. Recombinant human keratins K8 and K18 are prepared as described in Herrmann et al. [1999]. Briefly proteins are expressed in *e. coli*, purified and stored in 8M urea at -80°C. Before used in assays, acidic and basic keratins are mixed in equimolar ratio and refolded during a stepwise dialysis to urea free tris buffer containing 2mM Tris - pH 9.0 at room temperature and 1mM DTT. The wild type keratin 8 is covalently labeled via changing the native serine 243 to a cystein and subsequently standardized maleimid chemistry. The fluorescent dye used in our assay is ATTO647N (ATTO-TEC GmbH, Siegen, Germany)

2.2 Methods

2.2.1 Light activated contraction

10 µM monomeric G-actin in the presence of 0.1 µM myosin-II and 50 µM Blebbistatin Kovács et al. [2004], Kolega [2004] was polymerized by adding one tenth of the sample volume of 250 mM imidazol, 40 mM MgCl, 10 mM EGTA, 250 mM KCl and 2 mM ATP. Samples were prepared at 4°C to prevent polymerization before their location in a flow chamber. To reduce surface interaction flow chambers were pretreated with 5 mg/ml casein. Samples were scanned with a 0.5 mW confocal laser spot of a commercial Leica TCS SP5 microscope at 31 cm/s for the number of n stimulation cycles at 400 nm wave length. Both for stimulation and subsequent observation a 20× (NA 0.7) oil immersion objective was used. Confocal time

lapse xyz-stacks were obtained every 90 s to observe the dynamics of globally contracting gels. Samples were enclosed in sealed chambers to avoid any drift in the network. Addition of an ATP regeneration system, consisting of 20 mM creatine phosphate and 0.1 mg/ml creatine phosphokinase (Sigma-Aldrich) has no influence on the dynamics.

2.2.2 Arrested contraction

For arrested contraction experiments, V = 1,25μl droplets of the active gel are embedded in silicon oil, containing egg-PC, Span-80 and different surfactants depending on the specific task, described in chapter 4. These droplets can be visualized entirely using a Zeiss Axiovert 200 inverted microscope with a 5x long distance objective. Images are captured with a CCD camera (Orca ER, Hamamatsu). For experiments in chapter 4, G-actin is polymerized in presence of the crosslinker anillin by addition of 10 % of 10x AB buffer of pH value 7.2 (250 mM imidazol, 40 mM MgCl, 10 mM EGTA, 250 mM KCl and 2 mM ATP). Anillin is pre-diluted in Anillin buffer 2.1.3 to a concentration tenfold higher compared to the final concentration.

2.2.3 Particle image velocimetry

To investigate the internal dynamics 1 µm Fluoresbrite™ microspheres (Polysciences) were added as tracer particles. The displacement field was subsequently calculated by a custom-written particle image velocimetry (PIV) program implemented as an ImageJ (http://rsb.info.nih.gov/ij) plugin by Q. Tseng. The PIV was performed through an iterative scheme. In each iteration, the displacement was calculated by the normalized correlation coefficient algorithm, so that an individual interrogation window was compared with a larger searching window. The next iteration took into account the displacement field measured previously, so that a false correlation peak due to insufficient image features is avoided. The normalized cross-correlation also allowed us to define an arbitrary threshold to filter out low correlation values due to insufficient beads present in the window. The resulting final grid size for the displacement field was 10 µm × 10 µm, with 98 beads per interrogation window on average. The erroneous displacement vectors

were filtered out by their low correlation value and replaced by the median value from the neighboring vectors Tseng et al. [2012].

2.2.4 Digital Image Analysis of Orientations

The orientation of actin structures in Fig. 3.9 is inferred over time. First the analyzed images are cropped to be sure to only test for alignment of internal structures unbiased by the boundary itself. Then a method based on Fourier spectrum analysis is applied. Structures with a preferred orientation generate a periodic pattern at $+90°$ orientation in the Fourier transform of the image, compared to the direction of the objects in the input image. This plugin chops the image into square pieces, and computes their Fourier power spectra. The later are analyzed in polar coordinates, and the power is measured for each angle using the spatial filters proposed in Liu [1991]. The plugin computes a histogram indicating the amount of structures in a given direction. Images with completely isotropic content will give a flat histogram, whereas images in which there is a preferred orientation will give a histogram with a peak at that direction. The area under the histogram is normalized to binning size. For an isotropic system the distribution is constant at ≈ 0.044, because it is normailzed to the chosen binning size of 8Â°. The plugin is adapted from a routine written by Jean-Yves Tinevez.

2.2.5 Vesicle production

Vesicles of chapter 5 are produced using the continuous droplet interface crossing encapsulation (cDICE) method described in Abkarian et al. [2011]. It consists of a cylindrical rotating chamber, filled with a glucose solution to collect the vesicles, a lipid in oil solution to saturate the oil/water interfaces, and decane as the continuous phase in which droplet are produced. The solution containing the buffer is injected from a glass capillary by inserting the capillary's tip in the decane. Due to the centrifugal force, droplets detach from the tip. The droplets then move through the lipid in oil solution where they get coated by a first lipid monolayer and then by a second lipid monolayer while crossing the oil/water interface. The two monolayers zip together to form a bilayer. Vesicles are collected in the glucose solution which is sucked with a micropipette once the chamber is stopped. For

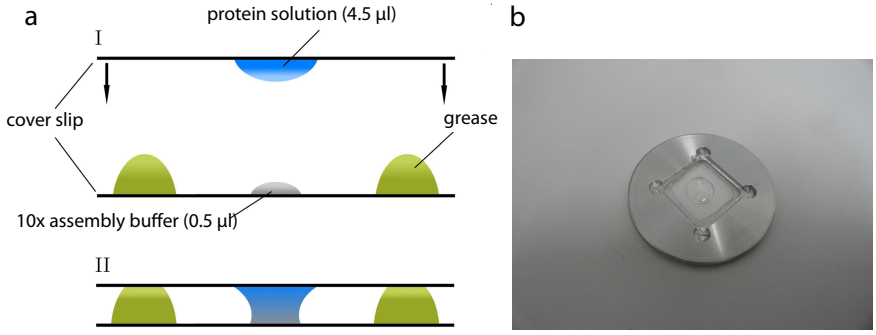

Figure 2.2 **Droplet Fusion Technique (a)** Samples are prepared by fusion of two droplets as described in 2.2.6. Schematics by Axel Stürmer. **(b)** Fused droplets in sample chamber customized for the optical tweezers instrument

the process to succeed, the osmolarity of the encapsulated solution and glucose solution have to be matched. The membrane is doped with 5% Biotin-Lipids for attachment to streptavidin beads.

2.2.6 Keratin network assembly

Network assembly is initiated by the addition of 10% of 10x assembly buffer (20mM Tris, pH 7.5, 10mM $MgCl_2$, 2 mM $CaCl_2$, 2 mM DTT, 5 mM ATP, 1M KCl) and 90% protein solution. Thereby the high speed of network formation prohibits conventional mixing with a pipette. To this end the "droplet fusion" technique has been developed Kayser et al. [2012], where a $4.5\mu l$ droplet of protein solution is applied to a cover slip. A second $0.5\mu l$ droplet of concentrated assembly buffer is applied to a second cover slip. Both droplets are then carefully merged by bringing the two coverslips closely together, see Fig. 2.2a. The small size of the sample guarantees fast distribution of the ions and a minimum shear flow. For different samples a constant final distance between the cover slips is a technical requirement for the optical tweezers assay. For this reason a customized sample holder is designed, see Fig.2.2b. Both droplets are carefully merged by approaching both cover slips close together.

2.2.7 Optical Tweezer

The current year 2016 marks the 30th anniversary of the seminal paper of Arthur Ashkin in 1986 on gradient optical traps, which first demonstrated that a focused beam of light could be used to stably trap micron-sized dielectric objects. During that period, optical traps or 'optical tweezers' have become an indispensable and versatile tool in understanding fundamental biological processes on various length scales from single molecules to cells. Since then optical tweezers have been used to study single molecular motors like kinesin Abbondanzieri et al. [2005] or rheological properties of active gels Mizuno et al. [2007]. At the same time a broad class of new applications emerge using this technique to manipulate nanometer-sized metallic objects Berthelot et al. [2013] or implement large numbers of individually structured optical traps and move them independently in three dimensions Curtis et al. [2002].

Because light carries momentum, an object that reflects or refracts a beam of light experiences a force. Although small this optical force is sufficient to manipulate a micrometer-size object, such as a polystyrene or silica bead. If the light is tightly focused by a lens, such an object will be trapped stably near the focus, experiencing a restoring force that is proportional to the spatial gradient in light intensity Ashkin et al. [1986].

This working principle can be understood applying a simple ray-optical picture, see Fig. 2.3. For a spherical particle scattering force, provided by reflection and absorption, cancels out in all directions but the direction of the light. The transmitting share of the light beam gets refracted twice by entering and exiting the bead. Due to its conservation, momentum gets transferred onto the bead, according to Newton's third law. When the particle is deflected out of the equilibrium position (e.g. by thermal forces) the momentum transfer results in a restoring force, pulling the bead back into the focus of the laser beam.

This ray optics approximation, where the trapped object is much larger than the wavelength of light, sketches one out of two limiting cases which can describe the force on a sphere. When the trapped particle is much smaller than the incident wavelength, the conditions for the Rayleigh scattering are satisfied. The particle is treated as a dipole in the electric field and its movement is due to superimposed

scattering and gradient force components. The scattering force is caused by absorption and reradiation of light by the dipole and is proportional to the scattering cross section of the bead and the total intensity of the incident trapping laser.

$$F_{\text{scatter}} \sim \sigma I_0, \tag{2.1}$$

The gradient force arises from the interaction of the induced dipole with the inhomogeneity of the electrical field near the focus

$$F_{\text{grad}} \sim \alpha \nabla I_0, \tag{2.2}$$

where α is the polarizability of the sphere and I_0 the intensity of the incident light. However, in most applications the dimensions of the trapped object are comparable to the wavelength of the trapping laser and consequently neither Mie nor Rayleigh regime approximations hold true. Thus, for an accurate description more complete electromagnetic theories have to be employed but hardly provide deeper understanding of the underlying physics.

2.2.7.1 Bead dynamics and calibration

For small displacements out of the equilibrium position the bead experiences a harmonic trap potential, therefore the optical trap acts as a Hookean spring on the trapped particle:

$$F = \kappa x \tag{2.3}$$

where F denotes the force on the bead, κ the trap stiffness and x the displacement out of the trap center. To obtain forces acting on the bead it is thus necessary to calibrate the trap stiffness κ and to measure the displacement x. The position of the trapped bead relative to the trap center is measured by imaging the interference pattern of the refracted and the non-refracted laser beam to a photodetector, such as a position-sensitive device (PSD). The detector converts the deflection of the bead into a voltage signal which can be filtered and recorded. The difference of the output voltage signal to the resting potential ΔV is proportional to the deflection

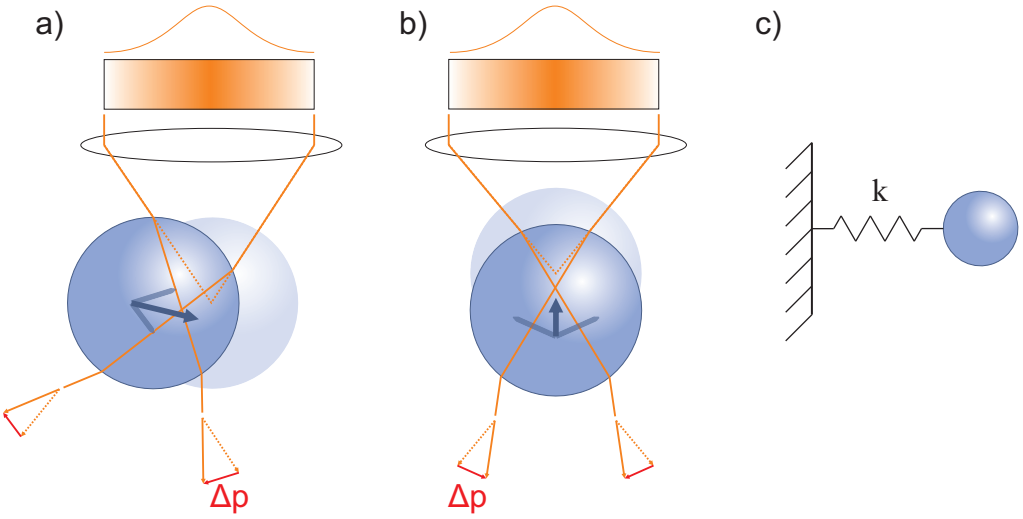

Figure 2.3 **Ray optics:** a) and b) show a cartoon of the forces acting on a bead which is displaced out of the trap center either in the horizontal a) or vertical direction b). Exemplary the optical path for two light beams is shown. The laser light is focused by an objective lens and then diffracted by the bead. The diffraction of the photons leads to a change in momentum Δp, shown as red arrows. The bead experiences the opposite momentum, light blue arrows. The overall force on the bead is shown in dark blue. For case a) acts in direction of the focus, but is slightly pointed below the focus. For a vertical displacement the resulting force points toward the focus of the lens and consequently opposing to the to the direction of light. c) For small displacements out of the trap center the trap acts as an hookean spring with a spring constant κ. Schematics by B. Pelz

Δx of the bead from the trap center.

$$\Delta x = \beta \Delta V \tag{2.4}$$

Here β represents a measure for the detection sensitivity to the deflection of the trapped particle and has to be determined to know the position in meters. Starting from the measured voltage signal $V(t)$ and using equations 2.4 and 2.3, the knowledge of β and κ is required to obtain the force and hence fully calibrate the instrument:

$$V(t) \xrightarrow{\cdot\beta} x(t) \xrightarrow{\cdot\kappa} F(t) \tag{2.5}$$

This chapter describes the two methods we use to calibrate the trap stiffness and the position detection system, both individually able to perform the entire calibration, starting with basic concepts about bead dynamics.

2.2.7.1.1 Bead dynamics The one dimensional brownian motion of a bead in a harmonic trap potential can be described by the following Langevin equation:

$$m\ddot{x}(t) + \gamma_0 \dot{x}(t) + \kappa x(t) = F_{ext}(t) \tag{2.6}$$

where $F_{ext}(t)$ is an arbitrary external force. The friction coefficient for a spherical particle is given by Stokes' law. $\gamma_0 = 6\pi\rho\nu R$ where ρ is the density of the medium, ν is its kinematic viscosity and R is the Radius of the bead. Due to the applicability of the low Reynold's number's regime, the inertia term can be neglected ($m\ddot{x} \to 0$).

If the force is assumed to be periodic,

$$F_{ext} = F_0 e^{(2\pi i f t + i\phi(f))}, \tag{2.7}$$

the stationary solution for 2.6 is

$$x(f,t) = \frac{F_0 exp(2\pi i f t + i\phi(f))}{2\pi i f \gamma_0 + \kappa} \tag{2.8}$$

For calibration purposes it is useful to Fourier transform 2.8 to the frequency

domain:

$$\hat{x}(f,\tilde{f}) = \frac{F_0 exp(2\pi i\phi(f))}{2\pi i f\gamma + \kappa}\delta(f-\tilde{f}) \tag{2.9}$$

The trapped particle is subjected to thermal motion, which is modeled with white noise, characterized by a constant power spectral density. The Fourier transform of the noise signal has a constant amplitude and random phase independent of the frequency. It can be written as $\hat{F}_{th}(\tilde{\omega}) = F_0 e^{i\phi(\tilde{f})}$. The squared magnitude of the response is:

$$|\hat{x}_{\mathrm{th}}(f)|^2 = \frac{|F_0/2\pi\gamma_0|^2}{f^2 + (\kappa/2\pi\gamma_0)^2} \tag{2.10}$$

The last formula 2.10 is already in a shape, that allows us to compute important parameters for our calibration routine. The Ornstein-Uhlenbeck theory for Brownian motion according to which $|F_0| = \sqrt{2k_BT\gamma_0}$ Berg-Sørensen and Flyvbjerg [2004], together with the Einstein Relation between diffusion constant, Boltzmann energy and friction coefficient $D = k_BT/\gamma_0$ and the corner frequency,

$$f_c = \frac{\kappa}{2\pi\gamma_0} \tag{2.11}$$

lead to a Lorentzian shape of the one-sided ($f \geq 0$) power spectral density, originating from the Brownian motion of the bead, which reads

$$P_{\mathrm{th}}(f) = \frac{2\left\langle|\hat{x}_{\mathrm{th}}(f)|^2\right\rangle}{t_{msr}} \xrightarrow[t_{msr}\to\infty]{} \frac{D}{\pi^2(f^2+f_c^2)} \tag{2.12}$$

2.2.7.1.2 Application of an external oscillation Within this method the position signal of the bead is recorded for a period t_{msr} at a frequency f_{sample}. Subsequently the power spectral density is calculated and equation 2.12 is fit to the data, thereby yielding the corner frequency f_c of the trapped bead. Inserted in equation 2.11 and with additional knowledge of γ_0, the trap stiffness could be calculated. The friction coefficient, however, is dependent on the distance to surfaces due to hydrodynamic effects and only given by the Stokes' relation if the bead is trapped far away from any surface. Furthermore the shear viscosity $\rho\nu$ of the medium depends on its temperature, which can severely deviate from room temperature due to local heating of the sample with the focused laser spot

Peterman et al. [2003].

To overcome this problem Tolić-Nørrelykke et al. [2006] developed a method which examines experimentally the drag coefficient simultaneously with the power spectrum. Thereby a piezo stage is used to drive the sample chamber sinusoidally relative to the optical trap at a single frequency f_{drive} and an amplitude A. The position of the stage as a function of time t is $x_{drive}(t) = Aexp(2\pi i f_{drive} t)$. With equation 2.7 the resulting external force is consequently

$$F_{ext} = 2\pi i f_{drive} \gamma A exp(2\pi i f_{drive} t) \tag{2.13}$$

and the contribution of this excitation to the Fourier transformed spectrum is a delta-function peak at the driving frequency.

$$P_{response}(f) = \frac{A^2}{2(1 + f_c^2/f_{\text{drive}}^2)} \delta(f - f_{\text{drive}}). \tag{2.14}$$

The sensitivity β will be determined by comparison of the amplitudes of excitation (piezo stage) and response (of the detector signal), using the measured PSD. With equation 2.4, the power spectral density in meter can be written as

$$P_{\text{response}}(f) = \beta^2 P_{\text{response}}^{\text{volt}}(f). \tag{2.15}$$

The corner frequency f_c is determined by fitting a Lorentzian and since the driving amplitude A and frequency $f$drive are known a priori, also P_{response} is known. $P_{\text{response}}^{\text{volt}}(f)$ is measured experimentally as well and hence β is obtained by

$$\beta = \sqrt{\frac{W_{\text{th}}}{W_{\text{ex}}}}, \qquad [\beta] = m/V, \tag{2.16}$$

with W_{ex} the experimentally determined power in the peak at the corresponding driving frequency. Following equation 2.14 the power W_{th} is determined by

$$W_{\text{th}} = \frac{A^2}{2(1 + f_c^2/f_{\text{drive}}^2)}. \tag{2.17}$$

For an experiment two values have to calibrated to be able analyze the data, the

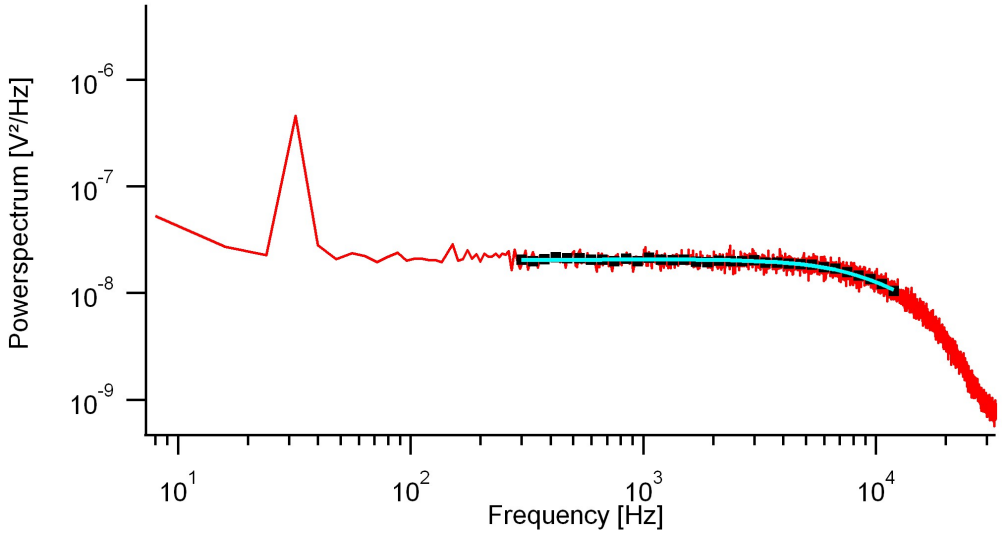

Figure 2.4 **Power spectral density:** PSD of a trapped 1 µm polystyrene bead with a corner frequency of f_c = 7654 Hz. The sample chamber is moved sinusoidally at a frequency of 32 Hz. The displayed PSD is an average of 100 individual power spectra, each recorded at a frequency of f_{sample} = 65 536 kHz with a measurement time t_{msr} = 1 s. The Lorentzian caused by thermal motion of the bead in the trapping potential can be seen, with an additional peak at driving frequency f_{drive} of the piezoelectric table. A fit to the blocked data (black) is shown in turquois.

trap stiffness κ and the distance calibration factor β. With these values the force on the bead κx and the displacement x out of the trap can be measured in their desired units. By fitting the first part of equation 2.14 to the experimentally obtained PSD, see Fig. 2.4, f_c and D^{volt} are determined. Using 2.11 and the Einstein-Smoluchowski-Relation the trap stiffness is then given by

$$\kappa = 2\pi f_c \frac{k_B T}{\beta^2 D^{\text{volt}}}. \tag{2.18}$$

2.2.7.1.3 Calibration with exponential relaxation curves One critical constraint is the device that alters the trap position. It must be very quick in its operation. Due to lack of moving parts that are subjected to inertia, the deflection of the trap through the AOD is limited by the beam diameter and the speed of sound in the crystal, in our case this response time is $\tau_{\text{response}} \approx 2\mu s$

Changing instantaneously the position of the trap from $x_0 = 0$ to $x_0 = X$, the solution of the bead position, according to equation 2.6 is:

$$x(t) = X\left(1 - \exp\left(\frac{-\gamma t}{2m}\right)\left[\frac{\gamma}{2m\xi}\sinh(\xi t) + \cosh(\xi t)\right]\right), \quad \xi \equiv \frac{\sqrt{\gamma^2 - 4m\kappa}}{2m} \tag{2.19}$$

Since the movement of a micron-sized particle can be approximated in the low Reynold's regime ($m \to 0$) this solution simplifies to

$$x(t) = X\left(1 - \exp\left(-\frac{t}{\tau}\right)\right), \quad \tau = \frac{\gamma}{\kappa} \tag{2.20}$$

With our system only the deviation from equilibrium position is detected. We keep X within the linear range of the detector, see Fig. 2.10, so the signal is proportional to $x(t) - X$:

$$V(t) = -\frac{X}{\beta}\exp\left(-\frac{t}{\tau_{H_2O}}\right) + V_0 \tag{2.21}$$

X is known from calibrating the deflection of the beam-steering unit, in this case the AOD. A decaying exponential is fit to the data and so both $\tau_{H_2O} = \gamma/\kappa = 1/2\pi f_c$ and β can be determined. Thereby, the friction coefficient γ can not be assumed to be a precisely known quantity. It varies a lot with the temperature, which is

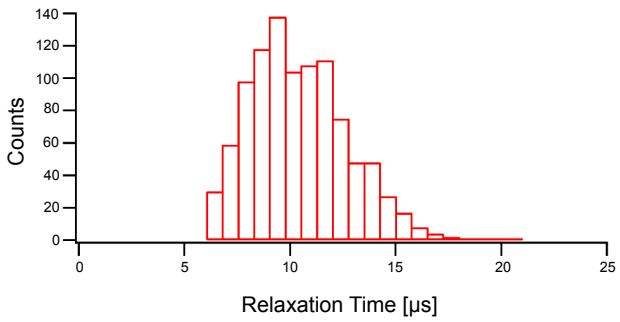

Figure 2.5 **Example for the distribution of relaxation times** τ_{H_2O}Theoretically the distribution should be symmetrical around the average value. Due to the limited acquisition bandwidth, short relaxation times are over estimated.

hard to measure in the area of the focus.

Furthermore the highest sampling rate of the data acquisition device puts a limit to this calibration method. The time between successive data points τ_{sample} should be significantly lower than the characteristic fall off time τ_{H_2O} to perform a reliable fit.

This technique is used to calibrate trap stiffness in chapter 6.2. Due to a geometrical constraint in sample preparation of the keratin networks, chamber thickness could not be reduced more than 0.6 mm. Local heating of the trap lead to significant drift, which prevented applying a reliable fit to the thermal power spectrum. The decay of the displacement peaks are fitted within a window of 3 ms to equation 2.21. The distribution of relaxation times from 1000 curves are displayed as histogram in Fig. 2.5

The mean value with standard deviation reads $\langle \tau_{H_2O} \rangle = 10.37 \pm 2.28 \mu s$. This value is kept as a constraint for the fitting routine, characterizing the finite onset time of the step strain procedure, see chapter 6.2.

In purely viscous solution the bead gets pulled into the center of the trap again. Consequently the V_0 in equation 2.21 should be zero. However, this is not the case, probably due to a systematic error as beam alignment or angle dependent transmission ratios of the AOD, as the levels correlate for different curves, see Fig. 2.6

The value for the sensitivity β can be derived from the peak signal subsequent to the known displacement step of $X = 100$ nm. The measured value for β depends

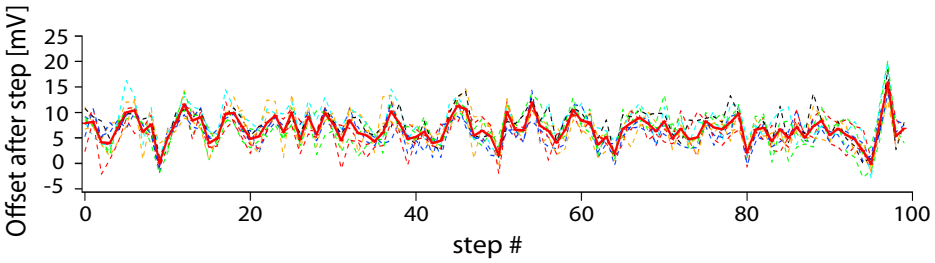

Figure 2.6 **Correlation of signal offset V_0 according to a certain displacement step:** each color of the dashed lines represent offsets for an individual bead. The red thick line is the average.

on the sampling frequency. The higher the sampling frequency, the more likely to actually measure the initial displacement position of the bead, relative to the new center of the trap. The mean value for β increases $\approx 20\%$ by sweeping the sampling frequency from 60kHz to 150kHz, see Fig. 2.7.

2.2.7.2 Custom built optical trap setup

As a part of this thesis a dual beam optical tweezers setup has been built. This chapter introduces the design of this instrument. The schematics can be seen in Fig. 2.8. For a high performance instrument various considerations have to be taken into account. The location should provide stable conditions concerning temperature, air drifts and mechanical vibrations potentially increasing the signal noise of the instrument. Light emerging the laser source gets split into its two polarization directions, resulting in two beams. One of them can be steered by an Acousto-Optic Deflector (AOD). Both beams get focussed by a water immersion objective in the specimen plane, forming two individual traps. The laser light emerging the foci is collimated by a condensor and again split up into its two directions of polarization. The back focal plane of the condensor is imaged onto two separate position sensitive devices (PSD), that measure position of the trapped particles independently. To observe the specimen plane, bright field illumination and detection is included into the instrument. For high flexibility Epi- and TIR fluorescence microscope capabilities are incorporated. The instrument provide two different wavelengths for excitation and an EMCCD camera for detection of the

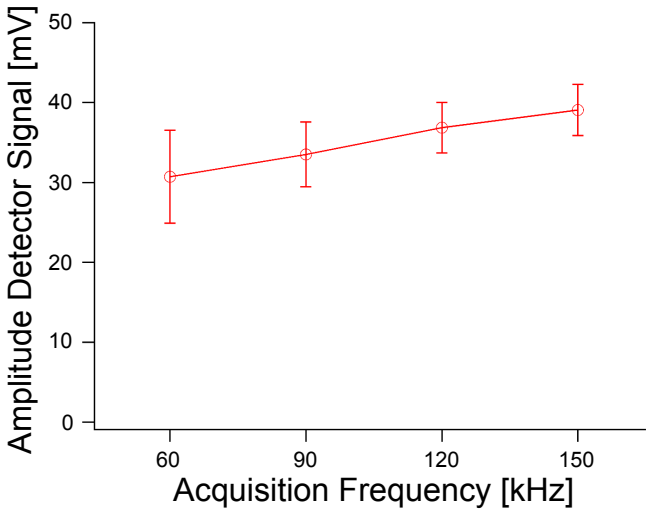

Figure 2.7 **Mean signal amplitude and variation is dependent on aquisition frequency:** experiments are performed at 150kHz, because the amplitude is highest and the variation lowest.

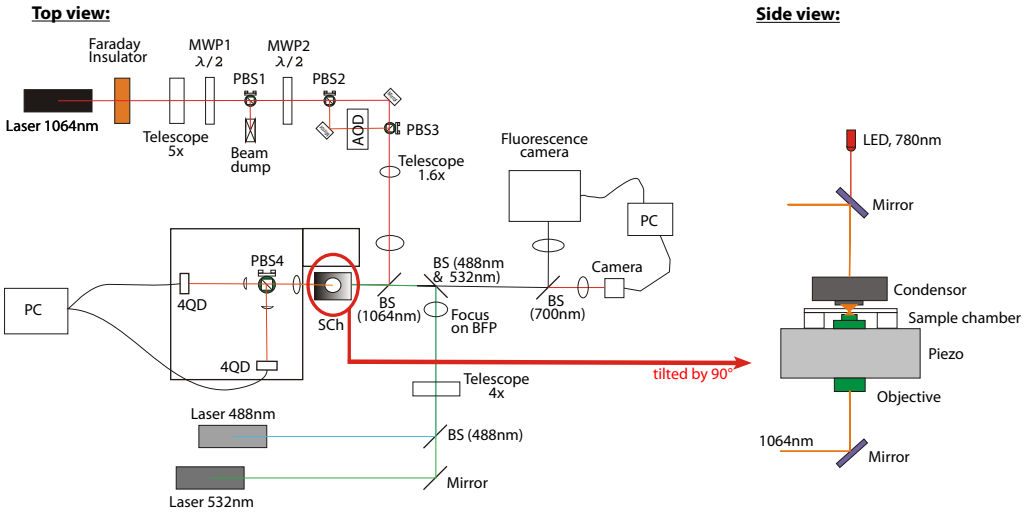

Figure 2.8 **Optical trap design:** Sketch of the optical trap design including the trapping and fluorescence parts. The trapping laser light is shown in red and orange, fluorescence excitation at 532 nm in green and 488 nm in blue. Light green represents the emitted fluorescence light. If not otherwise labeled black rectangles correspond to mirrors and blue rectangles to lenses. FI: Faraday isolator, AOD: Acousto optical Deflector, PBS: Polarizing beam splitter cube, DM: Dichroic mirror, 4QD: position sensitive device

signal.

2.2.7.2.1 Beam path The two most important individual items, that set the overall quality of the instrument, are the trapping laser and the objective. Here a linearly polarized 4 W 1064 nm Nd:YVO_4 diode pumped solid state laser (J20I-BL-106C, Spectra-Physics, USA) with a TEM_{00} mode is used for trapping. It reaches its excellent pointing and power stability properties at the highest operating power. The laser head, containing the Nd-dotted crystal, is mounted on the optical table. A multimode optical fiber transmits the pumping light from the noisy fan-cooled pumping diodes located next door to the laser head. A Faraday isolator (EOT-189.12011, Electro-Optics Technology Inc., USA), positioned in the beam path after the laser head, prevents back reflections from entering the laser head, which could lower the stability of the beam. This is convenient for futher beam alignment with auto collimation technique.

Further down stream the beam is expanded with a 5x telescope. The resulting beam diameter of 4 mm is chosen with respect to appropriate working condition of the AOD. A combination of a $\lambda/2$ plate, which rotates the laser's polarization axis, and a polarizing beam splitter cube (PBS) allows to control the overall laser power that passes onto the following optics. A further $\lambda/2$ plate sets the relative laser power of the two orthogonally polarized trapping beams separated by a second PBS. The motion of both $\lambda/2$ plates is steered with the rotational motor. Using an AOD in one of the two beams allows to deflect the beam into an angular area of $49 \times 49 \text{mrad}^2$ in two dimensions. In the sample plane this corresponds to a scan area of $\approx 40 \times 40 \mu\text{m}^2$, see Eq. 2.22. Due to coupling of phonons and photons inside the AOD's crystal the frequency of the laser gets shifted. This significantly reduces interference artefacts between the two beams Mangeol and Bockelmann [2008]. To reduce the influence of drift and noise on the two beams independently, the separate beam guidance is minimized. A third PBS recombines the beams of orthogonal polarization.

The following telescope consisting of to converging lenses plays a central role for the whole instrument. It serves two purposes, at first it matches the beam diameter to the 9.8mm back aperture of the objective to slightly overfill it - those beams off the optical axis are important to form the focus along the propagation of light. The second purpose is imaging the AOD‘s pivot onto the back focal plane of the objective, which is necessary to maintain a uniform trap stiffness across the

entire scan range of the AOD. If this condition is not fulfilled, tilting the beam out of its center position by the AOD will entail clipping by the back aperture of the objective. This affects the power going through the objective and decreases the trap stiffness. The ratio of the focal lengths f_1 and f_2 of this telescope is an important parameter for the movement d of the laser in the specimen plane, which is described by

$$d = 2 f_{\mathrm{EFL}} \frac{f_1}{f_2} \theta \tag{2.22}$$

where θ is the tilt angle of the AOD and f_{EFL} is the effective focal length of the objective $f_{\mathrm{EFL}} = \frac{t_0}{V}$ where V represents the magnification and t_0 the tube length.

The objective is used to focus the collimated beams to two diffraction limited spots inside the sample. Because spherical aberrations are minimized, a water-immersion objective (CFI PLAN APO IR 60XWI/NA=1.27, Nikon, Japan) is incorporated, which allows trapping deeper in the sample. Thereby hydrodynamic surface effect gets minimized.

The sample is mounted on a manually movable two axis translation stage, which is mounted in turn on a three axis computer controlled piezo table (P-517.3CL, Physik Instrumente, Germany) For the mechanical stability of the whole setup the design of the manual two axis translation stage and the mounting of the piezo is crucial. An oil immersion condensor (U-AAC, NA 1.4, focal length 9mm, Olympus, Germany) collimates the beam after the sample chamber. After this condensor the beams are split by polarization and the back focal plane of the condensor lens is imaged onto two position sensitive devices (DL100-7PCBA3, Silicon Sensor, Germany). This allows to detect the position of the two beads relative to the trap center.

For bright field illumination a 740 nm LED is used. The wavelength is chosen to exclude interference with trapping or fluorescence laser beams. The specimen plane is imaged onto a CMOS camera (DCC1545M, Thorlabs, USA)

2.2.7.2.2 Electronics The position sensitive devices (PSD) have a built in pre-amplifier and a output signal for x- and y-deflection and a sum signal proportional to the total light intensity impinging upon them. Before recording, all signals are anti-alias filtered with an eigth-order Butterworth filter with a 3dB-frequency

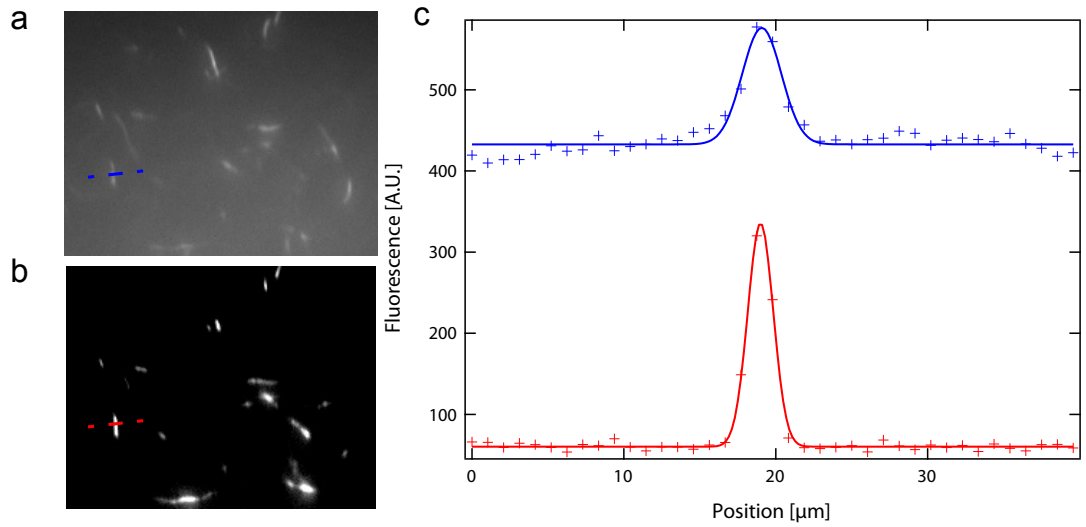

Figure 2.9 **TIRF-technique improves SNR** Fluorescently labelled actin filaments immobilized on a coverslip in **(a)** Epi-Fluorescence and **(b)** TIR-Fluorescence mode. **(c)** Fluorescence line profiles show the improved signal-to-noise ratio of the red dashed line compared to the blue. Both lines are 42μm in total length.

set to half the aquisition frequency and further amplified. (Model3384 Filter, Krohn-Hite, USA). A custom written program running on a reconfigurable field-programmable gate array (FPGA)-board (NI PCI-7833R, National Instruments, USA) is used for acquiring filtered and amplified data as well as real-time steering of the AOD, the $\lambda/2$-plates and the piezo table.

2.2.7.2.3 Fluorescence microscope Additional to the bright field illumination at 740 nm, two excitation lasers at the wavelength of 488nm and 532nm (Sapphire 488-20 CW CDRH and Sapphire 532-20 CW CDRH, Coherent, USA) provide fluorescence capacities for observing the specimen. Strongly expanded and collimated, both lasers then get combined with a dichroic mirror and focused onto the back focal plane of the objective. The focussing lens and a mirror can be moved manually with a linear translation stage. With this the sample can be illuminated either in Epi- or in Total Internal Reflection (TIR-) Fluoresence mode. The strong expansion of the excitation beam produces a constant illumination for a large area in the sample (ca $100 \times 100 \mu m^2$).

The emitted fluorescence light is separated from the bright field light with a

dichroic mirror and imaged onto an EMCCD camera (DU897D-COO Ixon3 , Andor Technology, USA).

The elimination of the background fluorescence from outside the focal plane in TIRF mode helps to improve the signal-to-noise ratio of the instrument. A sample of fluorescent actin filaments, immobilized on a coverslip, is shown in epifluorescent, 2.9a and TIRF mode 2.9b. Dashed lines indicate the scale of 40 μm and the corresponding intensity profiles are plotted in Fig. 2.9c. The signal-to-noise ratio improved from $\approx$ 1.3 to $\approx$ 5.3 as calculated by the respective ratio of the fitted gaussian peak to the offset of the distribution.

2.2.7.3 Characterization

2.2.7.3.1 Linearity of the optical trap The unambiguous derivation of the force from the detector signal is only possible where the detector response is linear to the deflection of a bead out of the trap focus. To characterize this region a bead stuck to the coverslip is scanned through the trapping focus in step-wise fashion with a piezo table, Fig. 2.10. It can be seen, that the linear region only extends about ±100nm out of the center of the trap. This sets a constraint for the trap stiffness: It has to be chosen such, that the deflection never exceeds the linear range under force.

2.2.7.3.2 Trap stiffness Indicated by eq. 2.2, the trap stiffness scales linearly with the laser power entering the trapping objective. Consequently measuring this relation is appropriate to characterize and test the function and alignment of the instrument. In Fig. 2.11 the linear relation between stiffness and intensity is shown. Blue and red data points correspond to stiffnesses of the perpendicularly arranged principal axes of the piezo stage.

With this a quantification of the spatial trap symmetry in the sample plane is possible. The slopes of the linear fits in x- and y-directions are in good agreement.

2.2.7.3.3 Spatial resolution The spatial resolution and the mechanical stability is tested by stepping a bead through the focus of the laser with a piezo table. The small increments of 2 nm at a rate of 1 Hz can be seen in Fig. 2.12 , which shows a good resolution of these steps across the entire time window of $>$20 s.

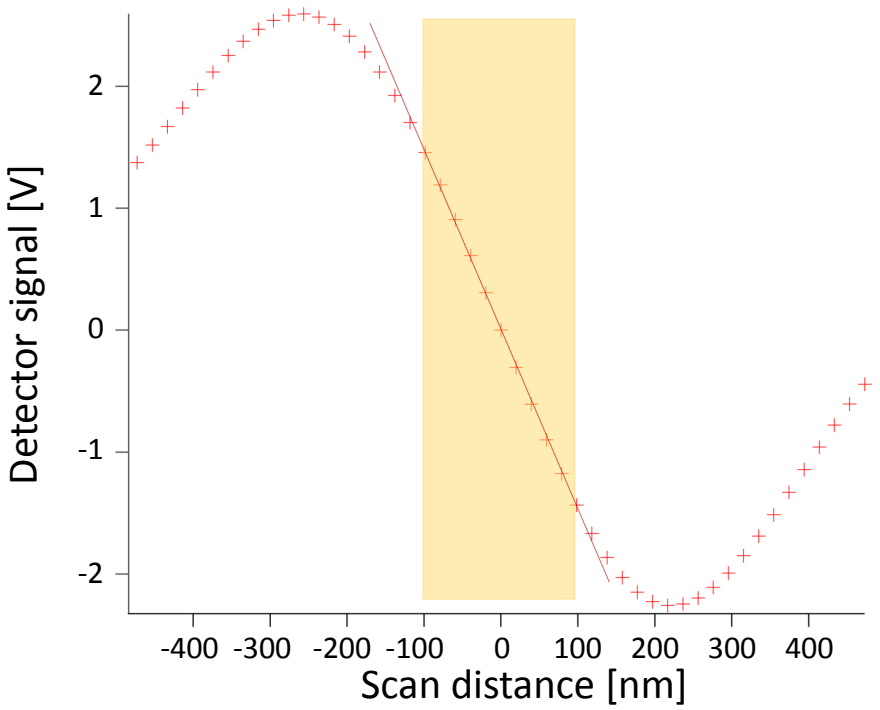

Figure 2.10 **Linearity of an optical trap:** Using the piezo stage a 1 μm polystyrene bead stuck on a coverslip gets moved step by step through the focus of the laser beam. The detector signal for each position is recorded for 1 s and averaged. The red line is a fit to the linear (shaded orange) region from about -100 nm to 100 nm, which corresponds to $\approx 10\%$ of the beam diameter.

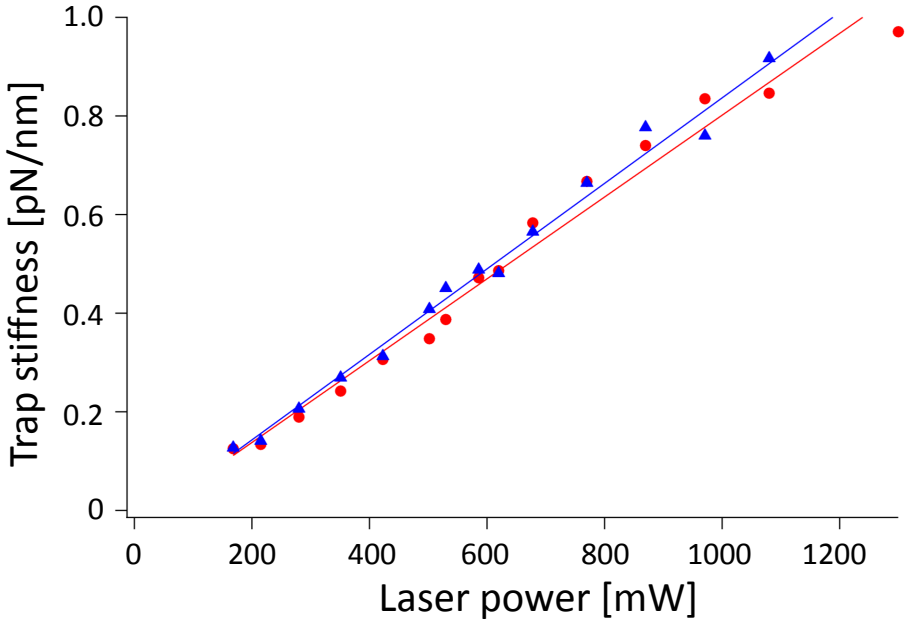

Figure 2.11 **Trap stiffness over power** Trap stiffness for 1 μm polystyrene bead versus the laser power entering the back aperture of the objective. For perpendicular directions trap stiffness in x (blue) and y (red) increase linearly with intensity.

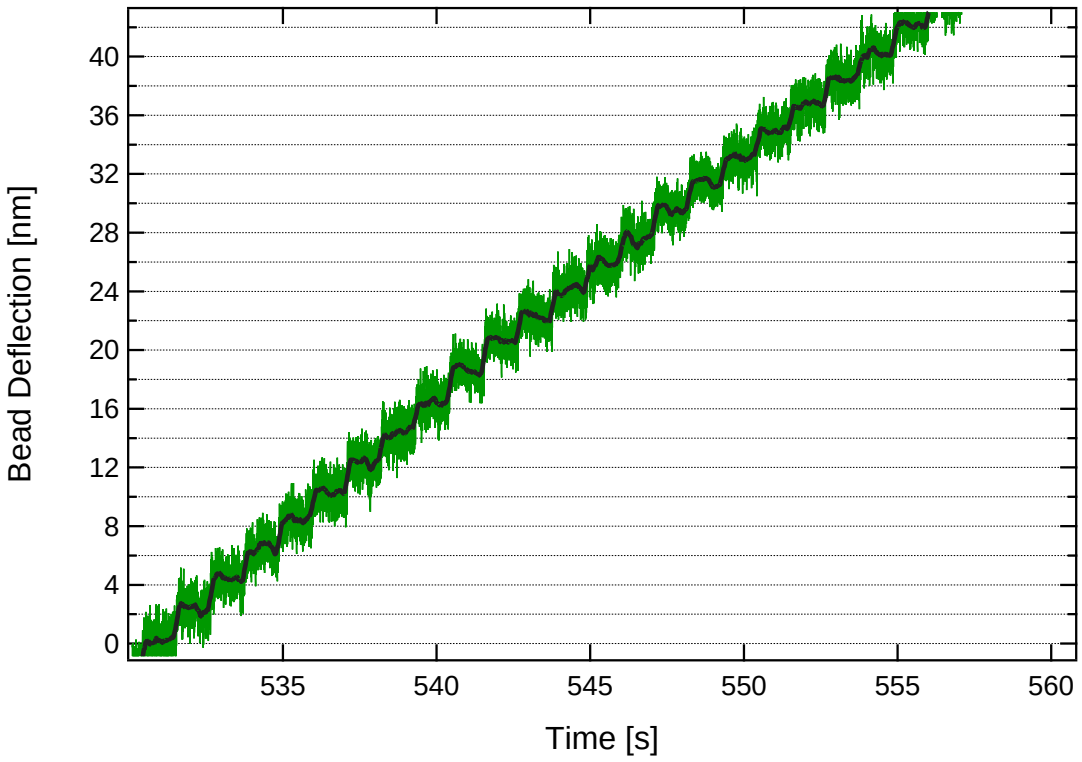

Figure 2.12 **Demonstration of the resolution of the optical trap setup** Plotted is the temporal course of a bead stuck to the coverslip and moved by a piezo table in 2 nm steps. The data is aquired with 5kHz (light green) and filtered using a 100 ms window (dark geen).

2.2.8 Microrheology

2.2.8.1 Basic rheology model

Viscoelastic materials can be rheologically modelled in order to understand their response to stress and strain. Linear combinations of springs, that represent elasticities, and dashpots (viscosities) are used to understand the behaviour on a basic level. The standard linear solid (SLS) model is the simplest model describing creep or recovery and stress relaxation. It can be seen as extension of the Maxwell model, that consists of a spring E_1 in series with a damper η, by a second spring E_0 in parallel, which describes the residual stress $\epsilon_0 E_0$ remaining in the sample, see Fig. 2.13a. In the assays of chapter 6, the reconstituted cytoskeletal networks can be rheologically described with the SLS-model: The applied strain relaxes, however a residual stress persists. In rheology stress is defined as force F per cross-section A,

$$\sigma = \frac{F}{A}, \tag{2.23}$$

which leads to a strain ϵ, which is the ratio of the length change Δl to the material's predeformed length l_0.

$$\epsilon = \frac{\Delta l}{l_0}, \tag{2.24}$$

For ideal linear elasticities, the Young's modulus E can be calculated as ratio of stress and strain:

$$E = \frac{\sigma}{\epsilon}, \tag{2.25}$$

and the ideal viscosity η depends on the rate of which the deformation is changing,

$$\sigma = \eta \frac{\partial \epsilon}{\partial t}. \tag{2.26}$$

In general, however, the current stress for a linear viscoelastic body is dependent on past strain rates. This is described by the Boltzmann's principle of superposition which relates the temporal evolution of the stress to the applied deformation:

$$\sigma(t) = \int_{-\infty}^{t} G(t-t') \frac{\partial \epsilon(t')}{\partial t'} dt', \tag{2.27}$$

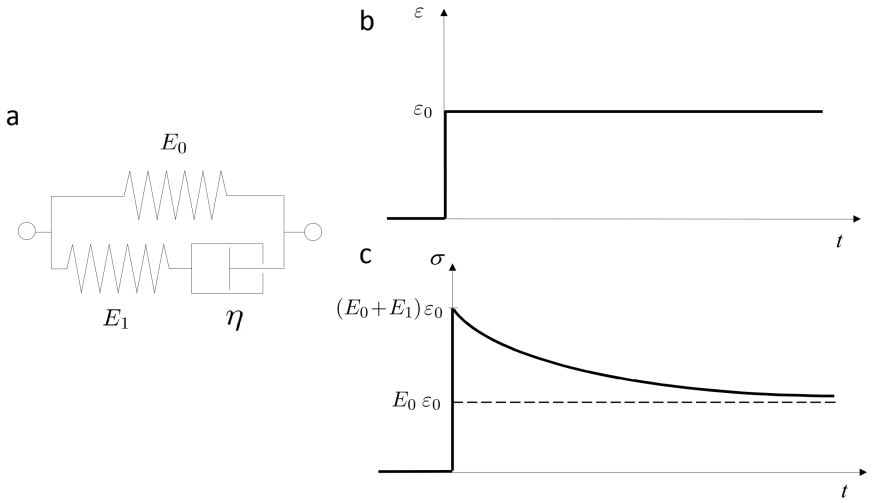

Figure 2.13 **The standard linear solid model (a)** Representation by a linear combination of springs and a dashpot **(b)** Step stain and **(c)** response of stress: instantaneous jump to the stress level $\epsilon_0(E_0 + E_1)$ followed by a single exponential stress relaxation to $\epsilon_0 E_0$ with the characteristic time $\tau = \eta/E_1$

In this equation $G(t)$ denotes the complex relaxation modulus, that can be interpreted as memory function. According to the Boltzmann principle the impact of subsequent deformations can be added up. Therefore G characterizes the material properties of the sample of interest.

2.2.8.2 The step strain measurement

In section 6, the elasticity and viscosity of the sample are measured by a step-strain experiment using a custom built optical tweezers set up, described in chapter 2.2.7. As depicted in Fig. 2.13b during a short time interval τ_0 a strain ϵ_0 is applied with the strain rate of

$$\frac{\partial \epsilon(t)}{\partial t} = \frac{\epsilon_0}{\tau_0}. \tag{2.28}$$

Inserted in eq. 2.27, this yields

$$\sigma(t) = \int_{t_0-\tau_0}^{t_0} G(t-t')\frac{\epsilon_0}{\partial \tau_0} dt', \tag{2.29}$$

Applying the mean value theorem yields

$$\sigma(t) = \frac{\epsilon_0}{\tau_0}\tau_0 G(t - t_0 - \lambda\tau_0), \lambda \in [0,1] \tag{2.30}$$

and finally for $t_0 = 0$ and $t \gg \tau_0$ follows

$$\sigma(t) = \epsilon_0 G(t). \tag{2.31}$$

Hence, if stress is monitored for sufficiently large times, the strain applied during τ_0 can be considered instantaneously.

By realization of a strain step to a SLS-body, using equations 2.25, 2.26 and 2.31 a stress answer

$$\sigma(t) = \epsilon_0 \left(E_1 \cdot exp\left(\frac{-(t - t_0)}{\tau} \right) + E_0 \right), \tag{2.32}$$

with the relaxation time

$$\tau = \eta / E_1 \tag{2.33}$$

according to Fig. 2.13c is obtained.

For step strain measurements performed in chapter 6 the concepts explained here need to be transferred Ziemann et al. [1994] to the optical tweezers assay, where a bead of radius R is used and the sample is deformed by the length Δl. With

$$\sigma(t) \to F(t) \tag{2.34}$$

$$\epsilon(t) \to 6\pi R \Delta l(t) \tag{2.35}$$

$$\epsilon_0 \to 6\pi R \Delta l(\tau_0) \tag{2.36}$$

Equation 2.32 becomes

$$F(t) = 6\pi R \Delta l(\tau_0) \left(E_1 \cdot exp\left(\frac{-(t - t_0)}{\tau} \right) + E_0 \right), \tag{2.37}$$

$$:= F_1 \cdot exp\left(\frac{-(t - t_0)}{\tau} \right) + F_0 \tag{2.38}$$

Based on Equations 2.37 and 2.38, the force curves obtained in chapter 6 are

evaluated. Material properties of the networks can be derived from fit parameters as described in detail by Maier [2014].

3 Boundaries steer the pattern formation of active actomyosin gels

Mechano-chemical stresses drive single cells far from thermodynamic equilibrium. Generated by actomyosin contractions, these cellular forces function on *internal* properties of a cell like the elastic moduli or the maintenance of their shapes. The active cytoskeleton also senses and adapts to properties of their surroundings, that are *external* cues Salbreux et al. [2012], Munjal and Lecuit [2014], Murrell et al. [2015], Mogilner and Keren [2009], Blanchoin et al. [2014]. Depending on the specific physiological task, the contractile arrays exhibit different shapes and are embedded in different environments. For instance, platelets show a uniform and isotropic contraction, whereas for cell migration in epithelial and endothelial cells the cell shape symmetry is broken to establish a front-to-rear polarity. In most of these processes the contractile parts maintain a constant attachment to their environments. So far little is known about the intricate interplay between initial assembly of contractile structures and the consecutive formation of structures. Still unclear is the contribution of boundary conditions for the built up of functional contractile modules Murrell et al. [2015], Thoresen et al. [2013].

These questions are addressed by application of the concept of active gels Prost et al. [2015], which describes force generation and dissipation with viscous and elastic model components. Several *in vitro* studies have succeeded in laying the basis for understanding the physical principles of the macroscopic contraction as a consequence of the interaction between actin, crosslinks and myosin-II, depicting the minimal system of a dynamic cytoskeletal network Bausch and Kroy [2006], Köhler et al. [2011], Bendix et al. [2008], Sheinman et al. [2015]. Current models

try to explain contractility in terms of microscopic interaction of these three key players Sheinman et al. [2014]. The length scale of reorganization is set by the type of the crosslink. The ratio both of the crosslink and the motor proteins to the actin monomer set the connectivity, the local viscoelastic moduli, the amplitude forces and within the ability to stabilize and destabilize the structures locally. Until recently the collective behaviour of these systems has been classified by their final steady state appearance, which give rise to a rich phase behavior Köhler and Bausch [2012], Backouche et al. [2006].

Within a wide range of crosslinkers, motor proteins actively contract the network into disjoint clusters Alvarado et al. [2013]. The size distribution of these clusters can be characterized by a power-law close to a critical point reminiscent of classical percolation theory Stauffer and Aharony [1994]. This theory predicts a transition state, below which a system is only locally correlated and connections between long distances cannot be found. Above this transition density of crosslinkers motors contract the well connected system into one single cluster. However, the critically connected regime spans a wide range of crosslink densities, in contrast to the expectations predicted by percolation theory.

The role of the motor proteins is not only characterized by contracting the network: the higher the density of force generators, the more crosslinks are needed to provide global connectivity, which suggests that motor proteins additionally promote ruptures in the network by forced unbinding of crosslinkers. It is known that crosslinkers bind only transiently to actin Lieleg et al. [2011] and their binding kinetics are affected by stress. Immobilized motors in a gliding assay are able to unzip propelled actin fascin bundles Ishikawa et al. [2003]. These findings entail that coordination of contractions over macroscopic length scales is achieved at *lower* motor activity. Increasing the motor density yields disruptive contraction.

Alvarado and coworkers support their experimental findings with a model of contractile actomyosin networks and additional molecular dynamics yielding two characteristic time scales. The first time scale τ_{off} describes the dependence of network connectivity by crosslinker un- and rebinding in the presence of force-generators. This characteristic crosslink unbinding time decreases exponentially with the tension T according to Bell's law: $\tau_{\text{off}} = \tau_{\text{off},0} \cdot \exp(-T/T_0) \cdot \exp(cd/T\mu\tau_{\text{off}})$ where $\tau_{\text{off},0}$ denotes the unbinding time in the absence of tension, T_0 is a charac-

teristic tension. The second exponential term accounts for rebinding, where the probability is considered, that an unbinding event is followed by a rebinding event. This probability is increased, if the crosslink density c, the characteristic mesh size d or the crosslinker‘s intrinsic on rate is increased, whereas it is decreased, if the tension T on the crosslink or the mobility μ of the crosslink is increased. By variation of only the crosslinker density c, all three regimes found in experiment can be recovered: the local, the critically connected and the global contraction regime. In addition the model shows, that it is the motor activity, that broadens the critical regime. The tension T experienced by a crosslink depends on the motor force and the local network configuration, which can change over time.

The second time scale τ_{relax} describes the time it takes for filaments in the network to relax in response to an unbinding event. In the limit of local contraction, where f and T is large, the network satisfies the relation $\tau_{\text{off}} < \tau_{\text{relax}}$; the high level of tension causes crosslinks to unbind quickly. As a consequence many concurrent cracks evolve and the network gets ruptured into many clusters. Neglecting the presence of a finite viscosity would lead to $\tau_{\text{relax}} = 0$ and networks would be disrupted only by quasi-static cracks.

In the absence of tension τ_{off} is roughly an order of magnitude higher than τ_{relax}. Once a crosslink unbinds, the network relaxes before the next crosslink unbinds. This limit corresponds to a quasistatic process Heussinger [2012]. In this limit it might be the force condition prevailing at a boundary that determines how the network evolves over time. Networks, that are fixed at rigid boundaries built up stress or rupture via a large crack sensitive to microscopic flaws reminiscent of Griffith‘s criterion Griffith [1921]. Unanchored networks contract affinely or might change shape when coupled to deformable boundaries.

In this chapter an active actomyosin system is presented, where the relaxation as a response to molecular forces is dominant over any possible unbinding event ($\tau_{\text{off}} > \tau_{\text{relax}}$). It is shown that the contractility of these model systems is steered by their boundary conditions. The force balance maintained at the boundary is responsible for shape transformations and the temporal evolution of them. Together with Martin Kroeger, ETH Zürich, a spring network model is developed, which fully recovers all shape transformations, while the observed dynamics are captured by a minimal set of critically damped harmonic springs. Anisotropic attachment of the

network leads to the formation of highly aligned contractile fibers, reminiscent of contractile modules found in cells. The following results are published in Schuppler et al. [2016]

3.1 Blebbistatin, a small myosin-II inhibitor is inactivated by blue light

In the presence of blebbistatin actin filaments and the molecular motor myosin II get assembled into isotropic networks. Blebbistatin quenches the ATPase activity of these motor proteins and greatly reduces their interaction with F-actin Sakamoto et al. [2005]. In a frequency sweep the elastic moduli of inactive gels stay almost unaffected with and without the presence of myosin/blebbistatin (Fig. 3.1b). Upon illumination with blue light of 488 nm blebbistatin locally loses this quenching function and consequently the motors get activated. Additionally, the inactivated blebbistatin stays attached at the myosin proteins, and so no further inhibition of the motors by free and still active blebbistatin is possible. Various two-dimensional geometries are activated by a scanning confocal spot. Thereby the active patterns remain connected to their surrounding inactive network (Fig. 3.1a). Forces generated by molecular motors contract the gel in a shape sensitive manner to its center of mass. The contraction persists until the motors present are too weak to induce further contraction.

3.2 Shape transformations of active gels are driven by their boundaries

Observation of an activated circular pattern shows that its shape is preserved during contraction (Fig. 3.2b, first row). Here, all tangential forces appearing at the active-inactive interface are equally balanced as a consequence of the round geometry. Due to this, forces occur only normal to the circular interface. This would entail a shape change for any geometry which is not circular. In such cases tangential force imbalances at the interface would lead to deformations altering the

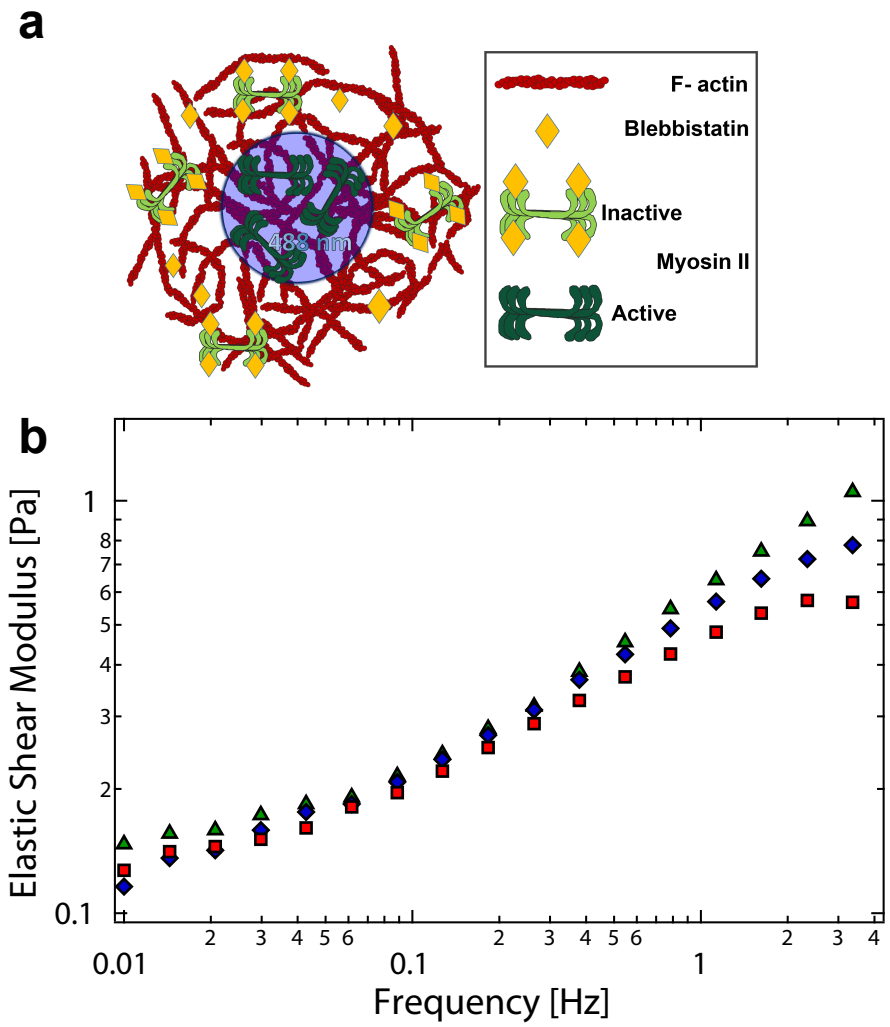

Figure 3.1 **Blebbistatin quenches myosin activity and gets inactivated by blue light** **(a)** At the beginning of the experiment myosin II filaments are activated by scanning patterns with a confocal blue (488 nm) argon laser beam for 20 consecutive cycles, thereby inactivating the blebbistatin. The activation of the myosin is stable for at least 90 min and no further activation is necessary during the further contraction. This observed permanent activation is attributed to the light induced covalent modification of the myosin II by the blebbistatin. **(b)** Rheology of the passive networks with 10 μM actin and 2mM ATP shows that elastic moduli stay almost unaffected by the additional presence of myosin and blebbistatin. Red squares: 0 μM Myosin, 0 μM Blebbistatin, blue Diamonds: 0 μM Myosin, 50 μ M Blebbistatin, Green Triangles 0,1μM Myosin 50 μ M Blebbistatin.

geometry and line curvature of the active gel while contracting. This is actually the case as for a quadratic pattern contraction changes its shape (Fig. 3.2b, 2nd row).

The resulting forces acting on every point of an interfacial line are set by their local active and passive surroundings. If for neighboring structural elements these net forces exhibit identical magnitude and direction, this part of the interface does not contribute to a change in shape. At the corners of a square the net force get changed drastically from one point to the next, entailing a force imbalance gradient along the interface. Consequently the pulling direction at a corner is different compared to an edge. During contractile rearrangements the various transpired shapes exhibit different curvatures of their boundaries, characterized by slightly altered force gradients. All these intermediate states themselves entail a further change in shape. For full squares the contraction rate for the middle of their width is higher than at the corners. This ultimately leads to a concave deformation of the full square's boundary (Fig. 3.2b, 2nd row).

If a thin hollow square is stimulated, the active part shares an additional interface with the passive surrounding. On the one hand the outer boundary is equal to the full square and should deform comparably. However, force gradients occur at the inner interface as well and global shape transformations can only be understood by taking these into account. With the same kind of argument as for the full square, inner corners are special geometrical points and experience active motor forces from an angle of 270°. Adjacent points along the inner boundary are subjected to contractile forces from only 180°. With this a strong gradient of force imbalances emerges as both the magnitude and the direction of forces get changed for neighboring points along this interface. The impact for the global shape transformation is, that the inner corners contract stronger than the outer corners, which are delayed as discussed for the full square. Initially the centers of the four long inner and outer edges hardly experience any force gradient along their boundaries. With proceeding contraction the curvature along the inner boundary tends to assimilate and the global shape transformation of a thin hollow square, differently to the full square, is convex, see Fig. 3.2b, 3rd row.

As can be seen in Fig. 3.2b, 4th row, shape transformations induced by the presence of an active-inactive interface seem to play only a role within a certain

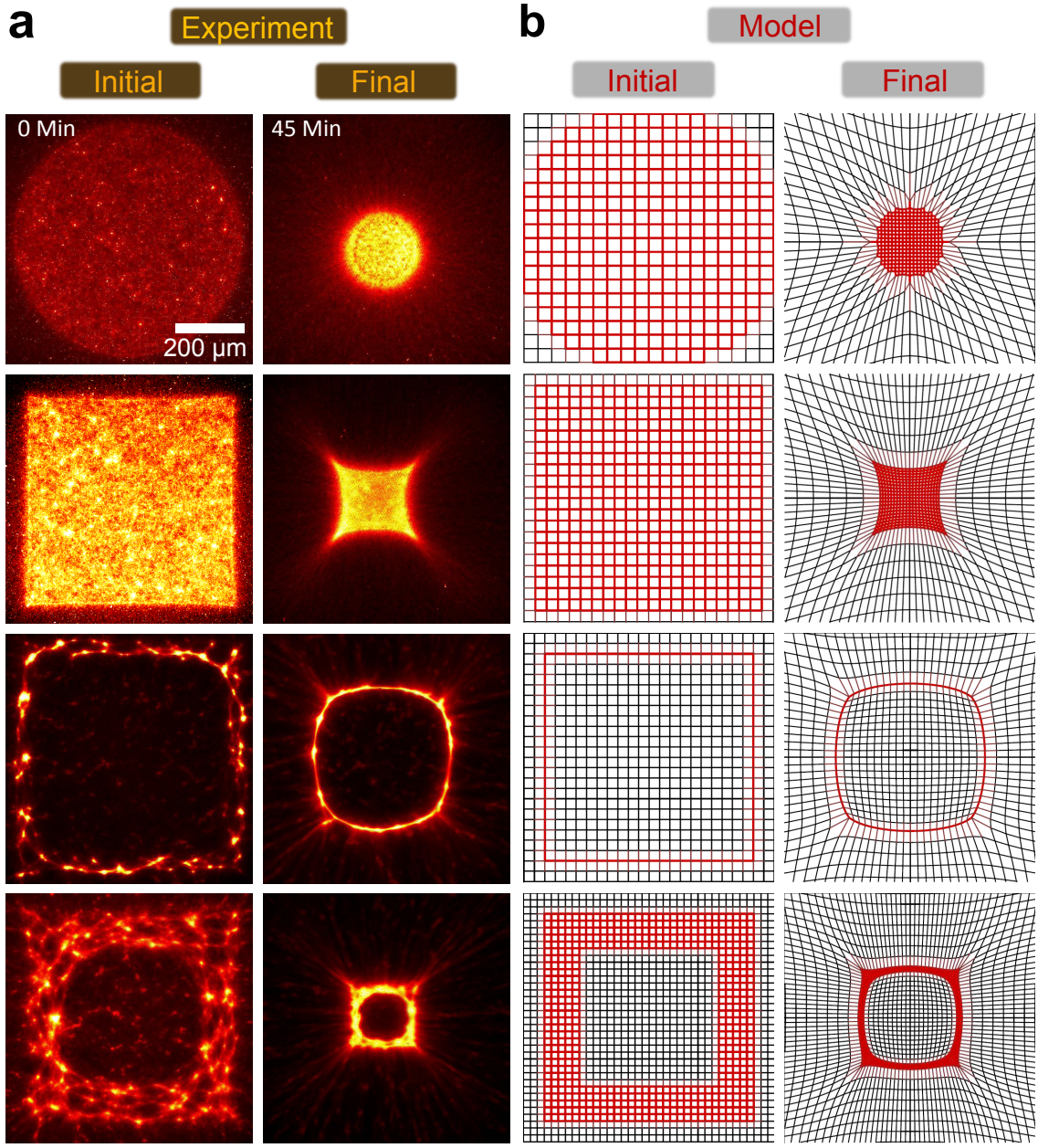

Figure 3.2 **Global shape changes of active actin gels. (a)** Start ($t_{\text{init}} = 0$ min) and end ($t = 45$ min) configuration of the fluorescently (phalloidin-Alexa 647N) labeled actin network, imaged with a 633nm HeNe laser line. During the stimulation process (< 1 min) activated molecular motors already accumulate fluorescent actin from all directions leading to an increased fluorescence directly after stimulation is finished ($t_{\text{init}} \equiv 0$ min). Circular patterns contract shape preserving whereas various initial geometries with corners entail non-affine deformations during contraction. Scalebar is identical for all figures. **(b)** Corresponding results of the spring network model (see section 3.3). The initial state is set by the activated region, the final state is obtained by efficient inversion of a sparse matrix with a suitable value for the ratio of spring coefficients $K = 0.13$ on a 30×30 square grid for all panels.

distance to these boundaries. By activating a thick hollow square the features of both the full and the thin hollow square can be observed after contraction. Concavely altered boundaries are adjacent to the outer corners while the inner boundary has become circular.

3.3 Static phenomenological simulations

A simple model, developed in colaboration with Martin Kröger, accounts for the described observations. Thereby active and passive parts of the networks are represented by crosslinked and non-tearable springs of different stiffness. Corresponding to the activation procedure, certain springs are brought into a non-equilibrium, the so-called 'activated' state. The model system initially conists of a two-dimensional array of crosslinker nodes. The nodes are set in a periodic simulation cell and are always connected to their next four neighbors by identical weak springs of spring coefficient k_w. Within the activated geometry of interest, spring coefficients are instantaneously redefined to an activated value $k_s > k_w$, see Fig. 3.3 a. With this, motor activity is modeled by the release of elastic energy, that has been initially stored in connected harmonic springs of uneven spring coefficients, that are initially identical elongated, see Fig. 3.3 b.

3.3.1 Effect of activation on shape changes

The forces acting on the nodes are thus linear with respect to their displacements. Consequently a matrix $\mathbf{A}$, determined by the properties of the initial simulation cell and the activated region as well as a constant vector $\mathbf{b}$, given by the boundary conditions fully recover the shape change of contractions. The final and force-free configuration vector reads $\mathbf{x}_{\text{fin}} = \mathbf{A}^{-1} \cdot \mathbf{b}$, Fig. 3.2c, right column, while the initial state $\mathbf{x}_{\text{init}}$ for the corresponding geometries is displayed in Fig. 3.2c, left column.

This spring network model captures the observed shape changes for any geometry. The final state can be calculated by the ratio of the two kinds of spring constants $K = k_w/k_s$. This implies that the contraction ratio should be reflected in the ratio K. Indeed, by increasing the dose of blue light via the number of activation cycles n in the experiment, the density of active motor proteins, corre-

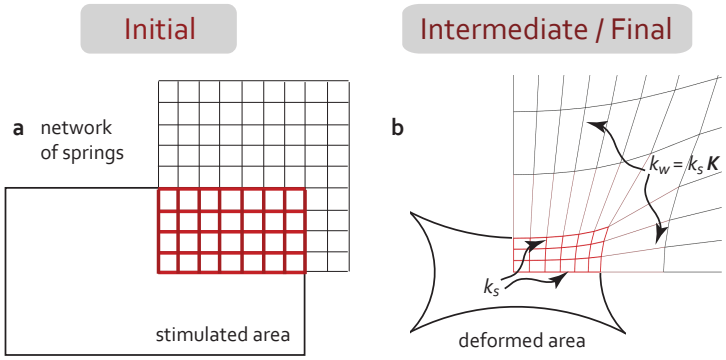

Figure 3.3 **Static model:** network of harmonic springs, that exhibits an increased stiffness within the stimulated (red), here rectangular area at **(a)** $t = 0$, and evolves in time towards its equilibrium state **(b)**.

sponding to k_s, are increased. As a consequence activated patterns with a fixed initial radius R_{init} are contracted to a smaller final size, characterized by their final radii R_{fin} (red circles in Fig. 3.4a).

3.3.2 Dependence of K on the activation dose

The activation of motors includes a repetitive scanning of the geometry for n times. After n stimulation cycles the amount of activated motors is denoted by S_n, $S_0 = 0$ and S_∞ is the amount of motors that can potentially be activated. The recursive relation $S_n = S_{n-1} + P(S_\infty - S_{n-1})$ denotes the amount of activated motors after n activation cycles, provided that activated motors cannot be activated twice. Thereby P is an activation efficiency $P \in [0,1]$, P is assumed to be constant for all activation procedures and relates the motors and the activating light. The recursive equation is solved by $S_n/S_\infty = 1 - (1 - P)^n$. Consequently as K_n is expected to depend linearly on S_n, which is the fraction of activated motors, these equation yield

$$R_{\text{fin}}/R_{\text{init}} = K = 1 + (K_\infty - 1)[1 - (1 - P)^n] \tag{3.1}$$

, which is the red solid line in Fig. 3.4a.

3.4 Motor density and size of activated patterns function on the dynamics of contraction

The contractions do not happen infinitively fast as the constituents are experiencing friction on their way from initial to final state. The corresponding velocities, in particular the maximal velocity of contraction $v_{\max}$, should depend on the density of the molecular motors. This density depends on the number of activation cycles (see 3.3.2). Indeed, with increasing density of active motor proteins, it is observed, that $v_{\max}$, measured at the boundary of an activated circular pattern with initial diameter of 775 μm, gets increased (black squares in Fig. 3.4a). The higher the motor density, the higher the force acting on the boundary. Upon activation of all available motors, further stimulation has no effect on $v_{\max}$ nor on the contraction ratio $R_{\text{fin}}/R_{\text{init}}$.

A suggestion of the introduced spring network model is, that the force on the interface gets increased proportional to the number of sequentially arranged springs. A higher force on the boundary should entail a faster contraction, especially a higher $v_{\max}$ at the boundary. This is the case as it is shown for the contraction of symmetric patterns, where the initially activated diameter $2L_{\text{init}}$ gets altered from 0 to 700 µm. At the boundary $v_{\max}$ reads out proportionate to $2L_{\text{init}}$ for circles and squares (Fig. 3.4b). Thereby $2L_{\text{init}}$ corresponds to the diameter for squares and the middle of the width for squares.

Conclusively from these experiments it is deduced that the maximal velocity of contraction $v_{\max}$ is governed by two parameters: the number of contractile units per length and the contraction velocity of each unit cell as has been suggested elsewhere Lenz et al. [2012].

Interestingly $v_{\max}$ of the boundary does not occur immediately after stimulation. This implies that initially contractile activity is not distributed homogeneously within the activated region. By engaging Particle Image Velocimetry analysis local contraction rates, defined as spatial velocity gradient dv_x/dx, are inferred, see Fig. 3.5. This reveals, that shortly upon activation contraction is merely confined to a region close to boundary. In the center of the pattern the local contraction rate starts off at almost zero, which means that there is no relative, contractile displacement between adjacent structures. As the contraction proceeds the local

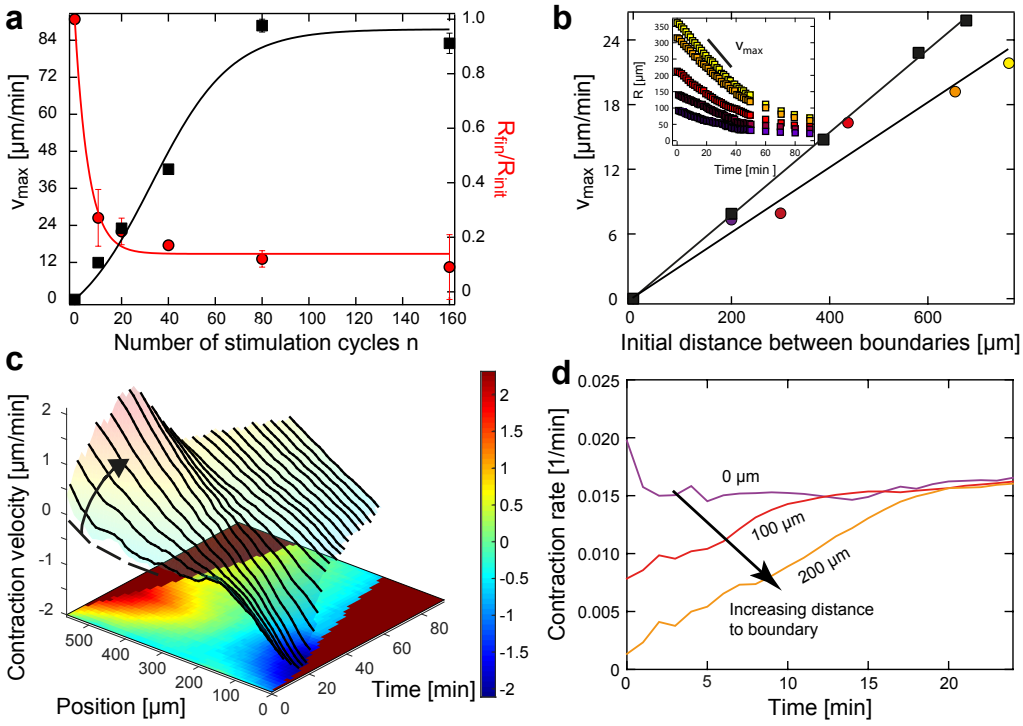

Figure 3.4 **Contraction speed depends on geometry. (a)** Final contraction ratio $R_{\mathrm{fin}}/R_{\mathrm{init}}$ (red) and maximal contraction velocity $v_{\max}$ (black) of initially identical circles (R_{init} = 388 µm) depends on the number of stimulation cycles n, corresponding to the density of active motors. Solid lines represent our calculations quantified by ratio of spring coefficients for which we find $K = R_{\mathrm{fin}}/R_{\mathrm{init}}$ (equation 3.1 with $P = 11\%$ and $K_\infty = 0.15$) and $v_{\max}$ (equation 3.13), both as a function of n. **(b)** Maximum contraction velocity versus the initial distance between boundaries for symmetric patterns (diameter for circles denoted as colored circles and the width in the middle for squares denoted as black squares) and identical $n = 20$. Solid lines represent linear fits in accordance with equation 3.4 of our minimal model, where $v_{\max} \sim L_{\mathrm{init}}$ is proportional to the initial distance between boundaries. The inset shows the radii of activated circles as a function of time for the corresponding color coded circles. **(c)** Internal dynamics during the onset of contraction of a full square (half width X_{init} = 290 µm) after $n = 5$ stimulations cycles. Color coded are the velocities of contractile structures along the x–coordinate obtained by PIV (Fig. 3.5). The boundary velocities increase to their temporal maxima in the course of time (light green → red, and light blue → dark blue) before approaching equilibrium in the long term. To visualize the symmetry and the size reduction of the contraction we show the z-projection of the corresponding 3D plot. **(d)** To determine where and when motor activity results in a contraction, the local velocity gradients dv_x/dx for three regions with increasing distance to one of the interfaces are calculated from the data in panel (c) (indicated by black bars, each covering 30 µm) and plotted over time. Close to the interface the contraction rate is high after activation and stays constant. With increasing distance to the boundary the contraction rate is close to zero and gets increased to the contraction rate measured for the boundary. Hence, motors initially contract structures only at the interface and the global ability to contract penetrates the activated area from there. We find that the maximal velocity of the boundary is observed when the center region exhibits the initial boundary contraction rate (here at $t \approx$ 16-20 min).

rates further away from the boundary get increased to the value, constantly obtained for the boundary. This value is reached earlier for structures that are closer to the boundary.

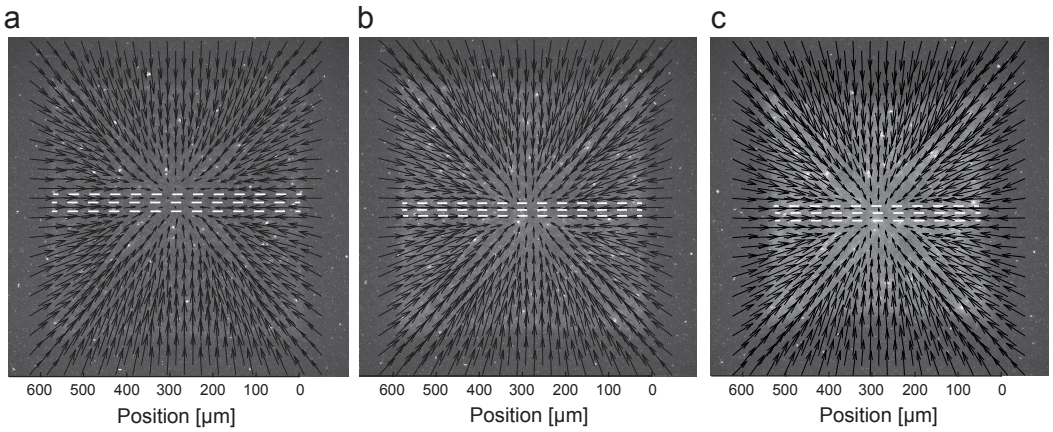

Figure 3.5 **PIV results corresponding to Fig. 3.4c** at times t = **(a)** 5 min, **(b)** 11 min, and **(c)** 17 min. The original PIV contains 4900 displacements (black arrows). Here it is shown every 8th arrow to distinguish individual ones. To evaluate contraction rates (Fig. 3.4c,d) deformation gradients along rows are chosen, whose arrows (including those of the neighboring rows) are parallel to these principal axes. All individual spatial gradients for rows are averaged to obtain the profile shown at the respective time point in Fig. 3.4c. The regions for evaluation are highlighted by light blue horizontal bars and limited by the extent of the active part of the gel, here shown in the background (gray).

These results are interpreted in the following manner: initially both the active and passive part of the gel is isotropic and local active forces are locally balanced. At the freshly created interface this symmetry is not fulfilled, since only here the forces emerge from both kinds of active and passive surroundings. And hence only at this interface force generators are able to translate the boundary. Activated motors exerting their forces further away from a boundary initially do not participate in the deformation of the interface. It is rationalized that they elevate the magnitude of tensile stresses on their neighboring structures. In turn this continuous auto-induced increase of tension allows motors to exert forces across larger regions. Once the radius of this interaction region exceeds the distance to the boundary, motors sense the presence of the boundary. They are now able to translate their forces into a displacement of the boundary and participate in contraction. Thus, the information of unbalanced forces, starting from the boundary, penetrates the

network during the onset of contraction. The maximal velocity of the boundaries is reached when all contractile structures between them sense their presence.

3.5 Dynamic coupling of asymmetric shapes

An immediate implication of this interpretation is, that the exact asymmetry in shape would determine the dynamics of the contractions. Rectangles with an initial aspect ratio $\text{Æ}_{\text{init}} = X_{\text{init}}/Y_{\text{init}} > 1$ are such geometries where, for each principal axis, the center region has a different distance to the boundary. Hence, parts of the activated area should be able to contract along the short y-direction while still being unable to contract in the perpendicular x-direction. Furthermore v_{max} should be reached earlier for the short axis Y than for the long axis X. Indeed, this is what occurs, see Fig. 3.6a. Another prediction is, that the entire interface initially deforms at the same speed, independent of Æ_{init}, which is shown in the inset of Fig. 3.6b. In accordance with the network spring model, which predicts identical aspect ratios of the initial and final states (red squares in Fig. 3.6b) the initial uniform contraction velocity around the perimeter implies a transient increase of the aspect ratio Æ_{max} (blue circles in Fig. 3.6b).

The maximum contraction speed of symmetric ($\text{Æ} = 1$) - geometries has been shown to be linear with respect to the initial distance between their boundaries (Fig. 3.4b). This could imply for asymmetric patterns that the ratio $v^X_{\text{max}}/v^Y_{\text{max}}$ of the maximal velocities of the principal axes equals the initial aspect ratio. Experimentally, however, this ratio reads $v^X_{\text{max}}/v^Y_{\text{max}} = \text{Æ}^{\nu}_{\text{init}}$ with $\nu = 0.6 \pm 0.1$ (Fig. 3.6c), which in turn gives rise to a dynamic coupling of the principal axes, resulting in either a hampered contraction along the length or an enhanced contraction along the width.

To shed light on this issue a series of rectangles with constant half length X_{init} and variable half width Y_{init} gets activated. The maximal velocity of the width increases linearly with increasing width as expected for the symmetric, undisturbed contraction, whereas the maximum contraction speed along the length gets increased non-linearly as the initial width gets larger (Fig. 3.6d). If there was no coupling, the maximal contraction speed of the length should be independent of the other dimension‘s size. Yet, the shortest side of an asymmetrically shaped,

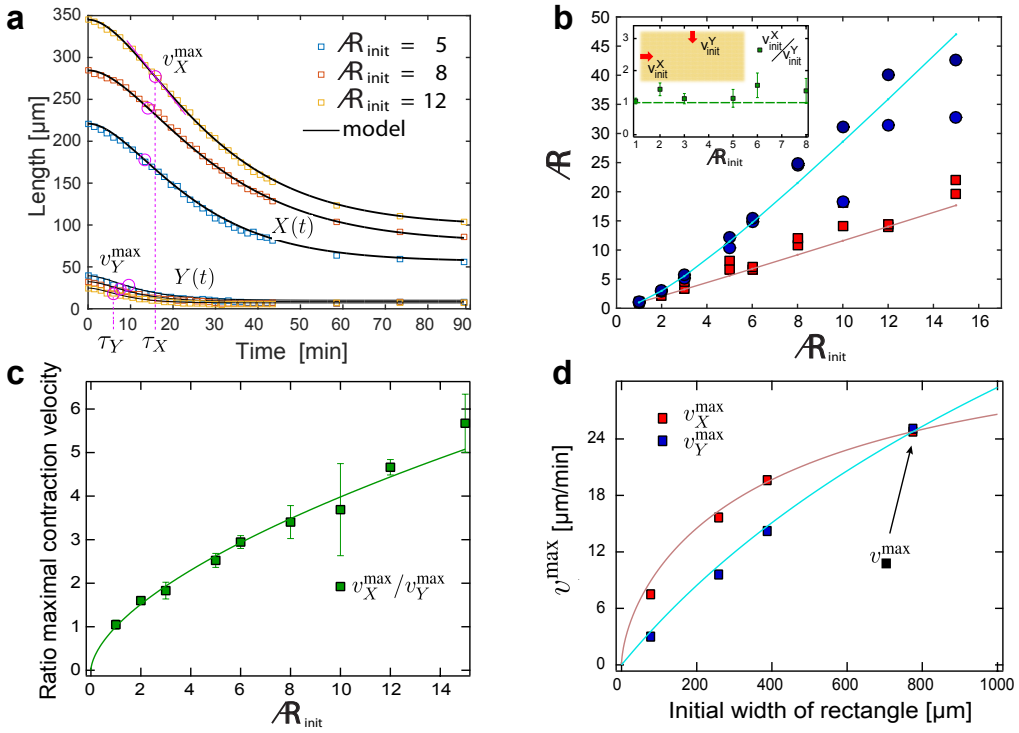

Figure 3.6 **Dynamics of contraction is set by shortest axis. (a)** Experimentally measured long axis $X(t)$ and short axis $Y(t)$ for filled rectangles with different initial axis ratio $\mathcal{R}_{\text{init}}$, with constant areas $X_{\text{init}}Y_{\text{init}}$ = 10,000 µm^2, together with equation 3.2 (solid lines), where $K = X_{\text{fin}}/X_{\text{init}} = Y_{\text{fin}}/Y_{\text{init}}$ and τ_X and τ_Y had been determined from the fits. While K is quasi constant due to identical stimulation density, the τ's depend on axis ratio (Fig. 3.8). For each dimension, the maximum velocity $v_{\max}$ occurs at a characteristic time τ that simultaneously determines the long-time relaxation behavior (equation 3.4). The contraction along the long axis $X(t)$ exhibits a strong delay compared with the contraction of the short axis $Y(t)$. The maximal contraction speed occurs much earlier in $Y(t)$ as shown in Fig. 3.8. **(b)** Characteristics of asymmetric contraction of initially asymmetric geometries: $\mathcal{R}_{\text{fin}} = X_{\text{fin}}/Y_{\text{fin}}$ (red squares) and $\mathcal{R}_{\max}$ (blue circles) both as a function of $\mathcal{R}_{\text{init}} = X_{\text{init}}/Y_{\text{init}}$, shown together with results of the minimal model (3.6). Inset: The ratio of velocities immediately after stimulation of the perpendicular interfaces is independent of the geometry. Because the velocities vanish at equilibrium, a limiting ratio of unity signals, that there is a unique acceleration and unique force strength normal to initially flat interfaces, as explained in section 3.6. **(c)** Ratio of the maximal velocities obeys the relation $v_X^{\max}/v_Y^{\max} = \mathcal{R}_{\text{init}}^{1-\nu}$ with $\nu = 0.4$. **(d)** For rectangles of constant half length X_{init} = 400 µm and variable width, $v_Y^{\max}$ (diamonds) depends basically linearly with Y_{init} as expected for the undisturbed contraction, whereas $v_X^{\max}$ (squares) gets increased non-linearly with Y_{init}, indicating a hampered contraction along the long side. The $v_{\blacksquare}^{\max} \approx 24$ µm/min value gets read off for the square case. Equation 3.11 of the minimal dynamical model predicts $v_X^{\max} = v_{\blacksquare}^{\max}/\mathcal{R}_{\text{init}}^{\nu/2}$ (red line) and $v_Y^{\max} = v_X^{\max}/\mathcal{R}_{\text{init}}^{1-\nu}$ (blue line) with $\nu = 0.4$, in agreement with these data. All network results shown here are identically activated with $n = 20$.

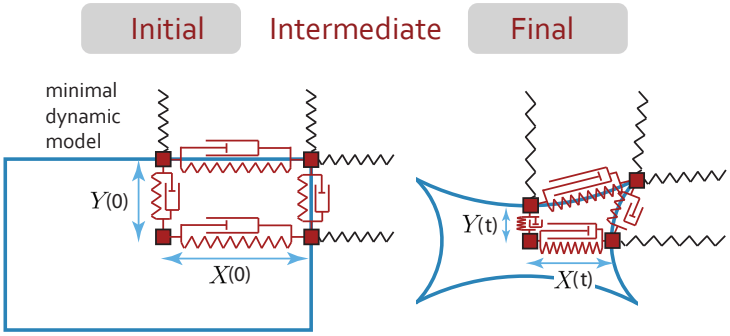

Figure 3.7 **Minimal Dynamic Model:** The minimal dynamical model is defined by a minimal amount of effective springs connecting the symmetry center with characteristic points residing on the interface between active and passive regions. The black squares represent masses, and the dashpots represent friction. The active (strong, red) and passive (weak, black) springs residing within the stimulated area and infinite surrounding, respectively, result in a net spring acting on the mass. The minimal dynamic model contains the spring coefficient for this net spring (equation 3.2), and a related compression time for each dimension. While the dynamics is governed by the compression time, the static behavior is for both models fully characterized by the same K

isotropic, contracting gel determines the overall dynamics of contraction.

3.6 Dynamic phenomenological simulations for the passive-active interface

To rationalize both the dynamics and the coupling of the contractile activity especially for asymmetric geometries, in collaboration with Martin Kroeger from ETH Zurich, the large grid of the static model gets replaced by only four effective critically damped springs, which allows to derive analytical expressions for all length changes over time. A Schematic of the so-called 'minimal dynamic model' is shown in 3.7. This is motivated as all lengths L (including the full circle radius R, mid length $2X$ and mid width $2Y$ of filled rectangles) monotonically decrease in the course of time from their initial values L_{init} at $t = t_{\text{init}} = 0$ to final values L_{fin} in a critically damped manner, see Fig. 3.6a.

All the data is perfectly fit by

$$L(t) = L_{\text{fin}} + (L_{\text{init}} - L_{\text{fin}})(1 + t/\tau_L)e^{-t/\tau_L}, \tag{3.2}$$

where L_{fin} and the characteristic time τ_L for each experiment is measured. Derivation of this equation yields the expression for the time-dependent velocity of the interface

$$v_L(t) = \frac{(1-K)L_{\text{init}}}{\tau_L^2} te^{-t/\tau_L}, \tag{3.3}$$

According to equation 3.2 the acceleration is given by $\ddot{L}(t) = (t^{-1} - \tau_L^{-1})\dot{L}(t)$ the extremal velocity is reached at τ_L and given by

$$v_{\text{max}}^L = v_L(\tau_L) = \frac{(1-K)}{e}\frac{L_{\text{init}}}{\tau_L} \tag{3.4}$$

Hence v_{max}^L is proportional to the initial distance between boundaries L_{init}. This is highlighted by Fig. 3.4b for the case of circles and squares. Additionally this linear dependence is visible from $v_Y^{\text{max}} \sim Y_{\text{init}}$ for the case where X_{init} is held fixed (see Fig. 3.6d).

In the following the consquences of this minimal set of critically damped springs are worked out for initially asymmetric filled rectangles.

At first, one further implication of the static model, see section 3.3, in particular for rectangles, is, that upon contraction the axis ratio is conserved

$$\text{Æ}_{\text{init}} = \text{Æ}_{\text{fin}}. \tag{3.5}$$

This is the case because for all filled shapes $L_{\text{fin}}/L_{\text{init}} = K$ is constant. Indeed, this is what is obtained in experiment and indicated by the red line in Fig. 3.6b.

Secondly, at small times the velocities of X and Y for filled rectangles are identical, see Fig. 3.6b (Inset):

$$\lim_{t\to 0} \frac{v_X(t)}{v_Y(t)} = 1, \tag{3.6}$$

where $v_L \equiv |\dot{L}|$. This observation is thus a simple consequence of the force imbalances (accelerations), initially acting on the boundary, being predominantely exerted by the immediate environment, which is identical for the middle of the perpendicular boundaries.

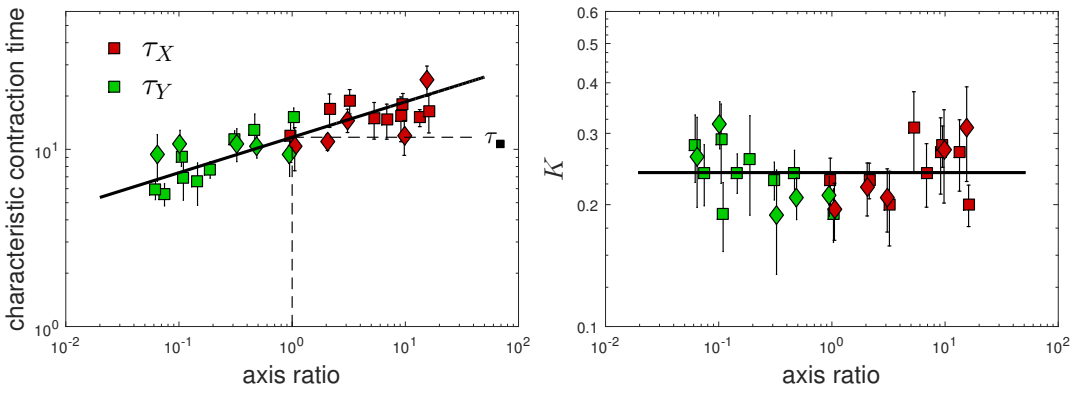

Figure 3.8 **Theory parameters for full rectangles**. They are obtained by fitting the measured $X(t)$ and $Y(t)$ to equation 3.2. **(a)** Contraction relaxation times τ_X (red) and τ_Y (green) and **(b)** K for the two directions, versus initial axis ratio (symbol a in equation 3.8). Black curves show **(a)** the model equation 3.8 for $\nu = 0.4$ and $\tau_\blacksquare = 12$ min, and **(b)** a constant $K = 0.23 \pm 0.04$, because K we expect to be unaffected by axis ratio at unchanged stimulation density. Squares and diamonds are used for series of experiments where X_{init} and the stimulated area had been kept fixed, respectively.

From these equations 3.2,3.5 and 3.6 follows, that

$$\frac{\tau_X}{\tau_Y} = \left(\frac{X_{\text{init}}}{Y_{\text{init}}}\right)^\nu = \mathit{AR}_{\text{init}}^\nu \tag{3.7}$$

with exponent $\nu = 0.5$, while a little smaller exponent $\nu = 0.4$ better captures the presented data.

As it is known from eq. 3.4 τ_L should be independent on L_{init} for $L \in \{X,Y,R\}$. Consequently τ_X and τ_Y must be functions of axis ratio *alone* given the constraint that their ratio is determined by equation 3.7. The simplest function $\tau(a)$ with $\tau_X = \tau(\mathit{AR}_{\text{init}})$ and $\tau_Y = \tau(\mathit{AR}_{\text{init}}^{-1})$ that fulfill $\tau(a)/\tau(a^{-1}) = a^\nu$ according to equation 3.7 is

$$\tau(a) = \tau_\blacksquare\, a^{\nu/2} \quad \longrightarrow \quad \tau_X = \tau_\blacksquare\, \mathit{AR}_{\text{init}}^{\nu/2},\ \ \tau_Y = \tau_\blacksquare\, \mathit{AR}_{\text{init}}^{-\nu/2} \tag{3.8}$$

With the exponent $\nu = 0.4$ these equations are compatible to the data, presented in Fig. 3.8, where $\tau_\blacksquare = \tau(1)$ for the case of a square ($\mathit{AR}_{\text{init}} = 1$). From the slope of Fig. 3.4b and eq. 3.4 the value for $\tau_\blacksquare \approx 10 - 15$ min for the typical range of K between 1/6 and 1/4.

Together with eq. 3.3 the ratio of the velocities reads

$$\frac{v_X(t)}{v_Y(t)} = \exp\left[\left(Æ_{\text{init}}^{\nu} - 1\right)\frac{t}{\tau_X}\right]. \tag{3.9}$$

which fully describes the temporal evolution of the axis ratio $Æ(t) = \frac{v_X(t)}{v_Y(t)}$. In particular $Æ(t)$ goes transiently through a maximum $Æ_{\max}$, which can be obtained by numerically solving $\dot{Æ}(t) = 0$ for t. The blue curve in Fig. 3.6b shows the dependence of $Æ_{\max}$ on $Æ_{\text{init}}$.

For the case of a filled rectangle eq. 3.4 directly implies

$$\frac{v_X^{\max}}{v_Y^{\max}} = Æ_{\text{init}}^{1-\nu}, \tag{3.10}$$

where eq. 3.7 has been inserted and which recovers the experimental data, shown in Fig. 3.6c. For the experimental data shown in Fig. 3.6d, X_{init} was held fixed, while $Y_{\text{init}} \leq X_{\text{init}}$ was varied. If equations 3.4 and 3.8 are written down for the two axes X, Y and the square case separately, the followin equations are obtained:

$$v_X^{\max} = \frac{v_■^{\max}}{Æ_{\text{init}}^{\nu/2}} = \frac{v_■^{\max}}{X_{\text{init}}^{\nu/2}} Y_{\text{init}}^{\nu/2}, \qquad v_Y^{\max} = \frac{v_X^{\max}}{Æ_{\text{init}}^{1-\nu}} = \frac{v_■^{\max}}{X_{\text{init}}^{1-\nu/2}} Y_{\text{init}}^{1-\nu/2} \tag{3.11}$$

again with $\nu = 0.4$. While $v_Y^{\max} \sim Y_{\text{init}}^{0.8}$ should thus vary mostly linearly, $v_X^{\max} \sim Y_{\text{init}}^{0.2}$ should depend weakly on Y_{init} when Y_{init} approaches X_{init}, and in overall agreement with our data (Fig. 3.6d). This representation of data eliminates the ratio of spring coefficients K, because it is contained in $v_■^{\max}$. With equation 3.8 the set of model parameters has been reduced to only two: $\tau_■$ and K_∞. These two parameters allow to predict the dynamical behavior of arbitrarily sized and shaped rectangles (or circles) as function of the stimulation dose, proporitonate to the number of stimulation cycles n.

The data in Fig. 3.4a shows, that both $v_{\max}$ and $K = R_{\text{fin}}/R_{\text{init}}$ saturate for large number of stimulations $n \to \infty$. In this limit $K_\infty \approx 0.17$ and $v_{\max}(K_\infty) \approx 84$ µm/min is determined for this set of experiments. To obtain the black curve

the equation 3.4 is written down as

$$v_{\max}(K) = \frac{(1-K)}{e}\frac{R_{\text{init}}}{\tau_R(K)}. \tag{3.12}$$

Deduced from the above discussion τ_R may be proportional to K. This yields the black curve in Fig. 3.4a

$$v_{\max}(n) = \frac{K_\infty v_{\max}(K_\infty)}{1-K_\infty} \times \frac{1-K(n)}{K(n)} \tag{3.13}$$

with the known numerical prefactor, where $K(n)$ is the red curve.

To summarize, the minimal model predicts numerous kinetic properties for the extensions of activated regions with different geometries and which are highlighted in Fig. 3.4a,b and Fig. 3.6a-d. While $v_L^{\max}$ is expected to be proportional to L_{init} for the circular and quadratic shapes, $v_X^{\max} \sim \sqrt{X_{\text{init}} Y_{\text{init}}}$ and $v_Y^{\max} \sim Y_{\text{init}}$ for $\mathcal{R}_{\text{init}} \gg 1$, in agreement with the presented data.

An interpretation about the microscopic behavior of the dynamic coupling is given in the following: while the final state is set by the different elastic properties of the polymeric network in- and outside activated regions, critically damped dynamics arise from large algebraic connectivity of the network. For an isotropic array of springs, a locally hampered ability to contract in one direction causes them to simultaneously shorten and align in this direction. As a result, these springs have already weakened at the time the hindrance gets released, and $\tau_X \sim (1+\mathcal{R}_{\text{init}})^\nu$ with the above ν and consequently $\tau_Y \sim (1+1/\mathcal{R}_{\text{init}})^\nu$ represent the dynamic coupling that allows to interpret the observations. Here a spring represents the mechanical action of a single motor filament that exerts polar forces. The motors can only operate in one direction and are preferably engaged into the direction towards the nearest force-unbalanced boundary. The friction and spring coefficient of the quiescent model gel are thus inherently coupled to allow for a maximally efficient relaxation. This is a very remarkable property this system seems to share with several natural interaction networks Paley and Baharani [2010], Ballerini et al. [2008b,a], where a critical damping is essential.

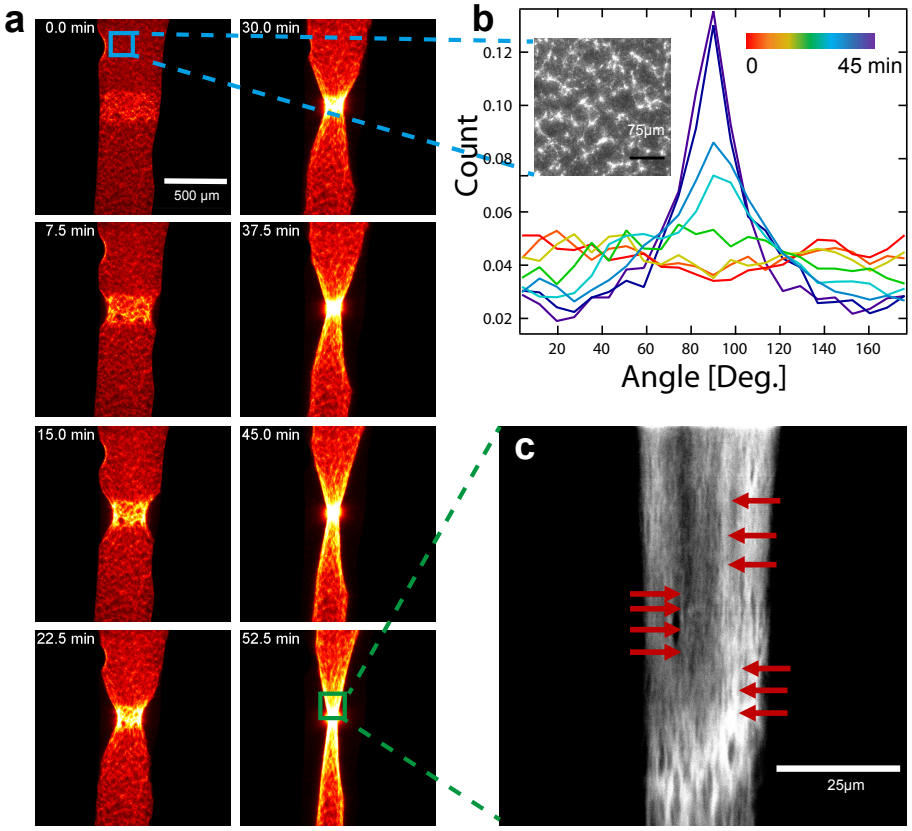

Figure 3.9 **Asymmetry induced formation of contractile fibers. (a)** Time series of a contracting array with a free boundary perpendicular to the channel axis. The stimulated area (n = 20 cycles) has an initial size of ≈ 100,000 µm^2. **(b)** Analysis of the whole images reveals the emerging orientation of actin structures parallel to the channel axis at 90°. Orientational distributions are shown for the 8 to panel (a) corresponding (color coded) time points during the contraction. Inset: Zoom into a yet uncontracted region reveals an apparently isotropic network, in agreement with the distribution at the starting point of stimulation (red line). **(c)** Zoom in after completed contraction: Red arrows denote increased alignment of actin structures as the result of motor activity and confinement of tension, quantitatively reflected by the peaked distribution (dark blue line).

3.7 Asymmetric attachment entails alignment

As yet it has been shown how the shape changes and the contractile dynamics of an active and contractile array are affected by its interplay with the inactive and visco-elastic surroundings. A free surface with negligible adhesion at the walls of a microfluidics system is introduced and with this the symmetry of attachment for the activated area. After the initial detachment of the gel from the channel walls, no restoring forces exist for contractions perpendicular to the channel axis. The active gel contracts mainly radially entailing an alignment of the filaments in the activated area along the axis of the channel (Fig. 3.9a). The strain fields produced by the contractile area penetrate deep into the inactive network. In this geometry the built up of tension is restricted to the long axis of the channel. Thus an increased order parallel to the direction of tension is observed (Fig. 3.9c). In Fig. 3.9b histograms are shown for 8 different time points during the contraction within the channel setup with a time step of 7.5 min. For the channel one can clearly see the developing peak at 90°, corresponding to the channel axis, starting from a flat spectrum, indicating the emerging alignment, see 2.2.4.

The alignment of cytoskeletal structures parallel to a free boundary is the result of the initial anisotropic attachment in concert with the large non-linear deformations induced by the actomyosin contraction. Hence, an initial anisotropy only present at the boundaries translates into a characteristic feature of the entire gel. Fiber alignment can thus be seen as a direct consequence of isotropic contraction of one-dimensionally attached gels. Such boundary driven plastic deformations might serve as directional template for biochemical and further structural polarization. This mechanical response may elucidate complex cell behaviors observed in assembly of stress fibers or myofibrillogenesis, where large deformations and mechanical tension have been shown crucial Weitkunat et al. [2014].

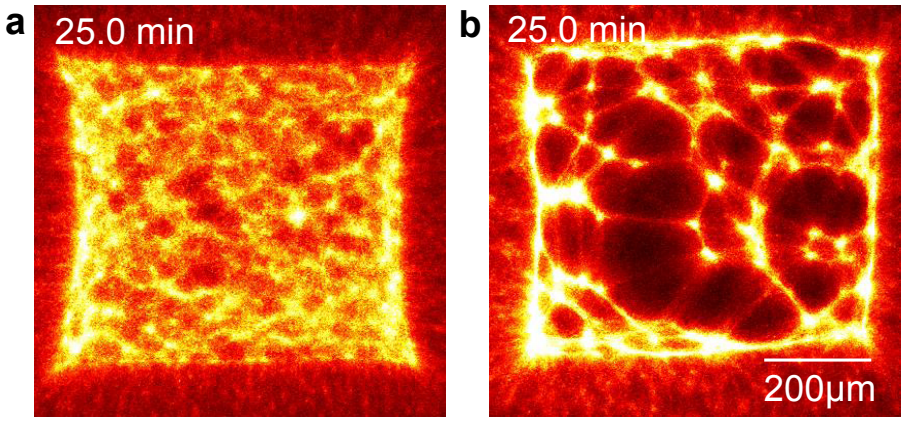

Figure 3.10 **Initial connectivity is essential for predictability of shape changes**. Upon decreasing the initial average F-actin length by the addition of 2nM capping protein the connectivity of the network is decreased (**(a)** to **(b)**). The fluorescence of the actin network is shown in the images. The gel breaks up into disjoint clusters in (b) while contracting non-uniformly. Both patterns are of identical size (≈ 600,000 µm^2) and activated during an identical amount of $n = 20$ stimulation cycles.

3.8 Initial connectivity is prerequisite for contraction

A prerequisite for the observability of shape transformations in general is the integrity of the connections between neighboring active and passive structures (Fig. 3.10a). If motor filaments create ruptures inside activated areas, the predictability of shape changes breaks down. A decrease of the initial average actin filament length $\langle l_{\text{F-actin}} \rangle_{\text{init}}$ to the regime of the persistence length of actin ≈ 17 µm, due to the presence of capping protein, results in the reduction of entanglements within the gel. After motors are switched to an active state predominantly small clusters of actin filaments are formed spontaneously (Fig. 3.10b). Due to this emerging inhomogeneity of the actin density the forces inside the active structures are no longer balanced. Once formed, the small clusters fuse and this formation of a few large clusters results in a decline of the network's connectivity. The more actin is accumulated in large clusters, the less material is available to connect different clusters with each other. During this process motors generate many concurrent

ruptures that constantly redefine the boundaries within the active pattern, ultimately resulting in a distribution of disjoint clusters.

3.9 Discussion

Taken together, the observed shape changes during gel contraction and alignment processes are the product of their initial shape and the mechanical properties of the surrounding passive matrix. Molecular motors apply forces randomly to the gel. The shape change as well as anisotropic contraction in case of rectangles solely follow from the responses at the boundaries. The presented mechanism emphasizes the influence of geometry on irreversible self organized shape changes in the micro-structure of active actin networks without any additional regulation of the motor-driven activity.

Measurements of the relationship between the deformation rate and the size of the contractile system provide insight into the underlying mechanisms governing the dynamics. For muscle fibers the speed of contraction is governed by two parameters: the size of a sarcomer, defining the length of a contractile unit and the force-velocity relation of skeletal muscle myosin, that sets the contraction speed of one contractile unit. Consequently the overall contraction rate is given by the number of contractile units per length and the rate of contraction of each unit. However, in isotropic networks, which are investigated here, a contractile unit is harder to define just by refering to a characteristic structure. As observed in reconstituted disordered actomyosin bundles, the average distance at which internal stresses generate buckling of actin filaments define at least a length scale for the contractile unit Thoresen et al. [2013]. The present system allows a precise definition of the size of the *entire* contractile array. With the linear dependence of the maximal contraction velocity on this size the concept of contractile unit cells, even for isotropic gels gets strengthened.

The extent of contraction in sarcomers is set by the overlap between thin and thick filaments. This overlap can reduce the initial length of them by approximately 30 %, whereas in non-muscle cells length reductions of actomyosin bundles occur up to 100 %. This suggests additional mechanisms such as filament deformation or even F-actin disassembly, which gets observed within contractile networks

Wilson et al. [2010] and bundles Haviv et al. [2008] *in vitro*. In the present system the extent of contraction is a function of the density of active motors. If all available motors are activated the length reductions are ≈ 85 %. Since actin is stabilized by Phalloidin it is assumed that no removal of filaments occur during interaction with myosin. This could indicate, that ≈ 15 % of size reduction in non-muscle cells are due to a motor induced depolymerization of actin filaments.

The transmission of force in filamentous actin networks is determined by their architecture. The nature and the relative amount of crosslinks set the network connectivity Köhler and Bausch [2012]. *In vitro* experiments demonstrated that the extent of crosslinking has a large impact on how contractile stresses are distributed in the network. Besides crosslinking proteins such as cortexillin, anillin, fascin or filamin A, myosin motors themselves can function as crosslinkers Murrell and Gardel [2012], Thoresen et al. [2011]. Additionally the results presented here show that the length distribution of F-actin also influence network crosslinking and entanglements. Longer filaments result in a higher network connectivity with drastic effect on contractile rearrangements.

The findings hint at a generic mechanism for the built up of structures as a consequence of the initial shape and boundary conditions. It has been shown before that the intricate interplay between shape and tension accounts for various spatial organizations on the cell and tissue level Alexandrova et al. [2008], Oakes et al. [2014], Munjal and Lecuit [2014]. Breaking a symmetry at the boundaries by introducing focal adhesion may be an essential clue for the self organized structure formation of stress fibers. The role and importance of boundary conditions is generic and may needed to be revisited in the case of larger length scales, leading for example to the structure formation in tissues. This work contributes to distinguish between purely mechanical self-organization of contractile gels within cells and adaptive biochemical responses to mechanical signals.

4 Attachment arrests contraction of active actin networks

Contractility generated by molecular motors is highly sensitive to mechanical context, as it is shown in chapter 3. In particular contraction always starts at the boundary and then progressively moves inwards. As it is discussed, this symmetry breaking might occur because filamentous actin structures within actively rearranging parts are subjected to isotropic forces, whereas F-actin close to a boundary faces large unbalanced forces. Thereby it is the specific mechanical property of the boundary that determines the amplitudes of the force imbalances. Purely viscous boundaries, where no restoring forces occur, exhibit the least resistance to rearrangements, while a highly elastic boundary should be able to prevent motors from inducing large scale rearrangements.

Historical experiments, nearly a hundred years ago, performed by Fenn demonstrated that upon shortening of muscles against an external load, which can be compared to an increase in elasticity of the boundary condition, extra heat is liberated Fenn [1923]. Huxley and Simmons proposed a model according to which crossbridges of the molecular motors proceed through the actin attached states more slowly, if an external force is applied Huxley and Simmons [1971].

Stationary adherent cells are symmetric systems. All forces generated by and acting on the cell are balanced and consequently the cell is allowed to keep its current shape and position. To initiate locomotion this symmetry has to be broken by *internal* or *external* triggers. The mechanical mechanisms that drive symmetry breaking are not understood. Recently it has been proposed that the fluctuation in adhesion strength (and myosin localization) above a critical threshold drives cytoskeletal rearrangements in fish epithelial keratocytes Barnhart et al. [2015], which are prerequisite for cellular movement.

In this chapter the existence of an arrested contractile state is presented, where the restoring forces exerted by the boundary can be sensitively tuned. Initially the active network is in a mechanosensitive state where the contractile activity of the motor proteins is balanced by the forces acting on the boundaries.

Contraction gets induced by external mechanical perturbation. Thereby the focus lies on the dependence of the induceable contraction on anillin, a protein that is essentially involved in contractile cytokeletal assemblies such as cytokinesis. This critical, arrested state of contractility is studied in a reconstituted model system of purified actin, myosin and the actin binding anillin fragment, specified in chapter 2.1.3.

4.1 Results

Actin filaments are assembled in the presence of His-tagged anillin, molecular motors and ATP into isotropic gels. The concentration of G-Actin is fixed at $c_{\text{actin}} = 10\mu M$ as well as the myosin concentration $c_{\text{myosin}} = 0.1\mu M$. The system ($V = 1{,}25\mu l$) is put into a solution containing mineral oil and a mixture of 90% Egg- and - to avoid unspecific interaction with the interface - 10% PEG-Lipids, thereby forming a large droplet with ≈ 1mm in diameter, see Fig. 4.1a,b. To increase its stability the droplet is transferred to a solution containing the surfactant *span 80*. After 1 min. the time evolution of the homogeneously formed F-actin gels gets imaged by wide field microscopy.

Varying the concentration of anillin in a wide range ($0\mu M \leq c_{\text{anillin}} \leq 10\mu M$) leads to the observation of 4 regimes Alvarado et al. [2013], Köhler et al. [2012]: In absence of any crosslinks the actomyosin network stays homogeneous and no macroscopic contraction is observed. This is coherent with the fact that the presence of crosslinks is essential for large-scale rearrangements within the active network Bendix et al. [2008]. At low anillin concentrations ($c_{\text{anillin}} \leq 0.1\mu M$), the activity of the motors break up the emerging network structures and collapses them into disjoint clusters (data not shown). With increasing crosslink concentration the connectivity within the active gel is enhanced. For $0.5\mu M \leq c_{\text{anillin}} \leq 8\mu M$ the entire network is strongly crosslinked and consequently forms one single cluster upon contraction Fig. 4.2a,d.

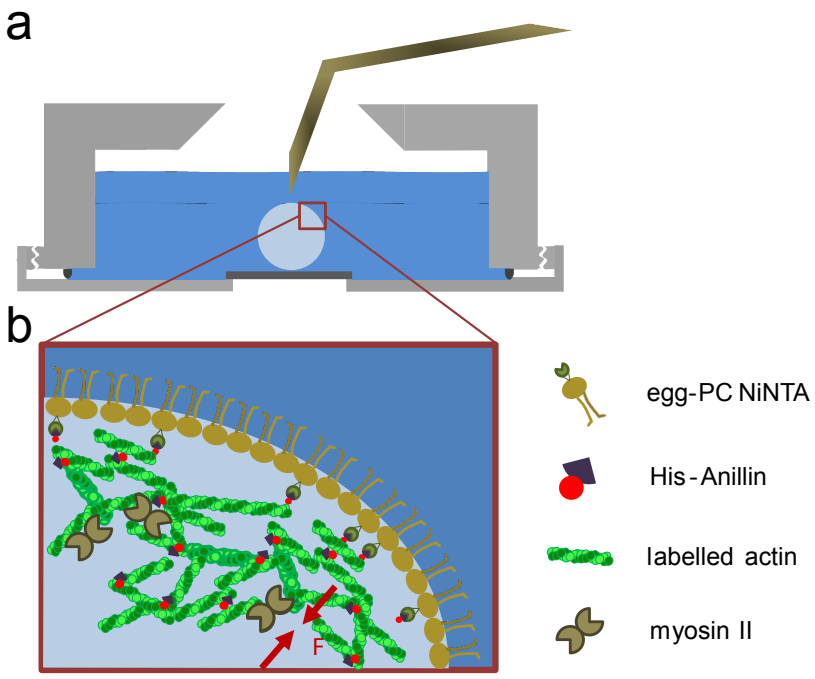

Figure 4.1 **Illustration of the droplet experiment: (a)** Droplets are put in a screw chamber (grey) filled with mineral oil and surfactant (blue region) on a silanized cover slip. The chamber is observed with a fluorescence microscope. The droplet is perturbed by a pointed capillary, moved by a micro manipulator. **(b)** The interface consists of a single layer of egg-PC lipids, 10% conjugated with PEG 3000 and 10% NiNTA respectively. Labelled actin (bright green), myosin II filaments (olive) and His-Anillin (red) assemble into an isotropic gel. Intra gel connectivity and attachment to the interface can be tuned by the relative amount of anillin to NiNTA lipids.

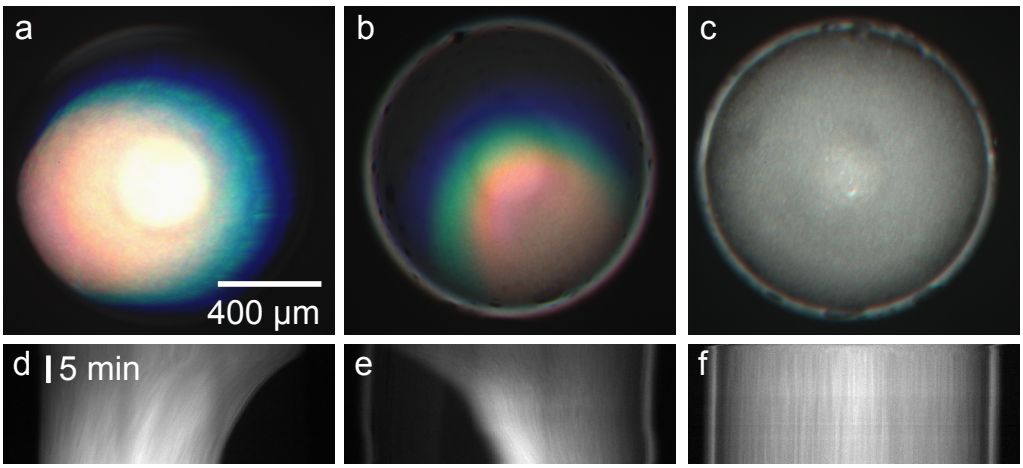

Figure 4.2 **Macroscopic contraction of active actin anillin networks.** Droplets of $1.25\mu L$ of $10\mu M$ actin, $0.1\mu M$ myosin-II in presence of $c_{\text{anillin}} = 3\mu M$**(a,b,d,e)** and of $c_{\text{anillin}} = 10\mu M$ **(c,f)** are shown as color overlay from 1 min (blue) to 20 min. (red) after initiation of polymerization **(a-c)**. The incorporation of PEG-Lipids into the droplet interface leads to a contraction without residues of actin at the interface **(a,d)** while additional 10% NiNTA-Lipids keeps some fluorescent actin located there **(b,e)**. Macroscopic contraction is stalled for equimolar ratios of actin to anillin while at lower crosslink concentrations gels globally contract. The time traces of the contractions are shown in the kymographs **(d-f)**

The higher the ratio of the crosslinks to the actin, the higher the connectivity and the higher the elasticity of the crosslinked actin structures. Bausch and Kroy [2006], Schmoller et al. [2009], Lieleg et al. [2007] A higher elasticity entails a higher load on the active motor proteins. At a prevalence of the crosslinks $\approx 8.5\mu M \leq c_{\text{anillin}}$ the actin filaments are assembled into a rigid network with a well-defined bundle thickness. It remains stable although crosslinks undergo binding and unbinding events Lieleg et al. [2008, 2011]. Motors are too weak to contract these structures and the contraction is arrested, see Fig. 4.2c,f. The phase transition from macroscopic to arrested contraction is shown in the top panel of the diagram, Fig. 4.4.

The question addressed now is whether there is a regime in crosslinker density, where on the one hand motors are still strong enough to induce contraction, but on the other hand the attachment to the boundary arrest these rearrangements. As the bending rigidity κ of the interface is too high (typical values are $\kappa \approx 10^{-11} J$ or $10^9 k_B T$) to be deformed by the motor filaments present it could function as anchor exerting a restoring force to the contractile network. To test this hypothesis 10% NiNTA-Lipids are incorporated into the droplet interface. NiNTA specifically binds the His-Tag of the anillin proteins and serves as connector between the interface and the active gel. Observing macroscopic contraction of the actin gel in such a droplet indeed shows the residues of fluorescent actin structures located at the interface, Fig. 4.2b,e. If the connectivity within the gel is low (e.g. $c_{\text{anillin}} = 3\mu M$), ruptures can occur close to the interface, Fig. 4.3.

This could imply that at a higher connectivity, respectively a higher anillin concentration, myosin-induced ruptures can be prevented. Indeed, in some cases above $c_{\text{anillin}} = 6\mu M$ the network does not contract spontaneously, see Fig. 4.4 lower panel, black and blue circles. Thereby the transition from global to arrested contraction is shifted to lower anillin concentrations, compared to the case where lipids had only been functionalized with PEG, see Fig. 4.4 (1st row), black circles.

To test the origin of this arrestment the attachment to the interface gets perturbed by a pointed capillary steered by a micro manipulator, see Fig. 4.1. To ensure it does not contract spontaneously, the gel gets observed for 10 Min. prior to perturbation. Between $5\mu M \leq c_{\text{anillin}} \leq 7\mu M$, see Fig. 4.4 (2nd row) the perturbation potentially leads to an extensive rupture to the droplet interface, Fig. 4.5a

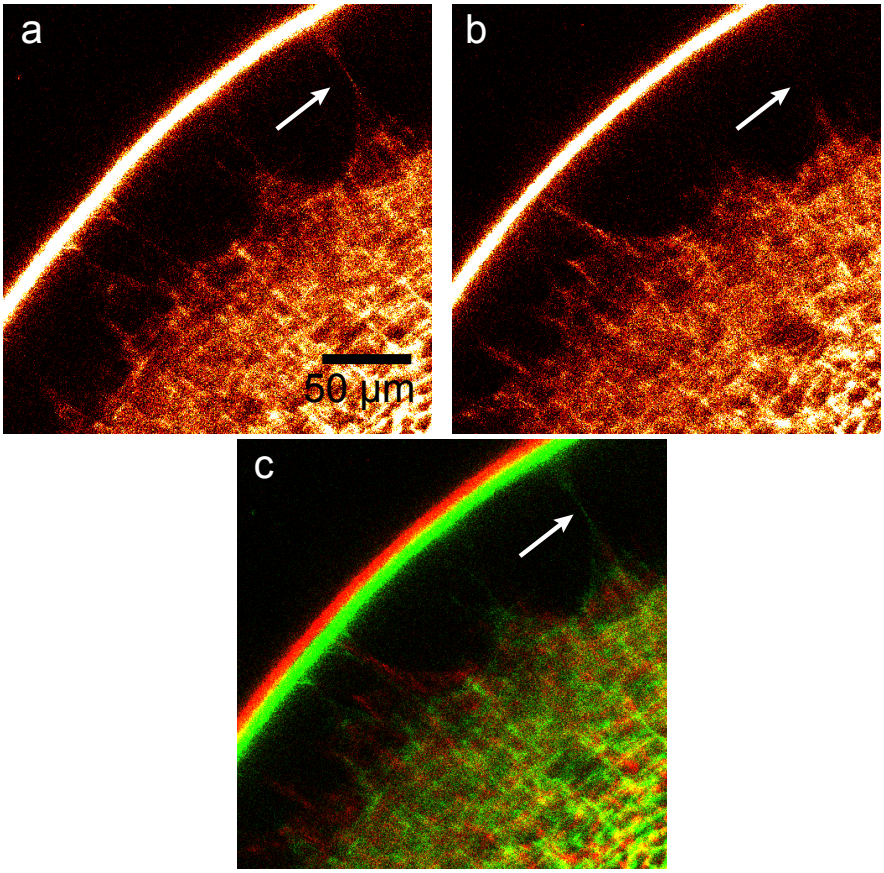

Figure 4.3 **Rupture event close to the droplet interface.** Confocal images of a contracting actin network ($10\mu M$) bundled by anillin $4\mu M$ at the droplet interface before **(a)** and after **(b)** demolition from the interface. **(c)** shows an overlay of **(a)** (green) and **(b)** (red). The arrow denotes the center of the ruptured structure. Both the network and the droplet interface relaxes upon this rupture event. Scale is identical for all pictures.

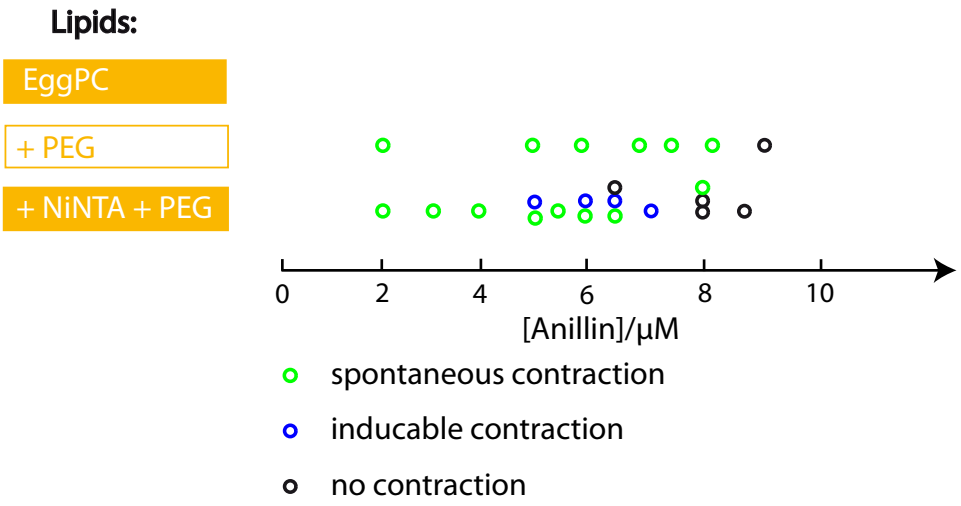

Figure 4.4 **Attachment allows arrestment of contraction** By addition of attachment sites (NiNTA) to the lipid interface, a mechanosensitive state becomes apparent (blue circles). It separates the regimes of spontaneous and impeded contraction, where motors are too weak to induce contraction because the elasticity of the actin network is too high.

(white arrow). If this new interface is created, the force balancing at the boundary of the contractile gel has changed. No restoring forces are exerted by the boundary anymore and the gel contracts towards the center of the droplet. This is visualized by a kymograph of the perturbation and the subsequent contraction of the actin scaffold, see Fig. 4.5b.

4.2 Discussion

In this chapter it is shown that myosin-driven contractility can be transiently suppressed. Thereby it is the force maintained at the boundary that arrests the rearrangements. Where connection to the boundary is disrupted by external perturbation, a mechano sensitive state becomes apparent. The initially arrested contraction gets revived and the active gel contracts away from the nascent and purely viscous interface.

Since the model system contains only a few highly purified components the requirements for this mechano-sensitive state can be quantified in terms of cross-

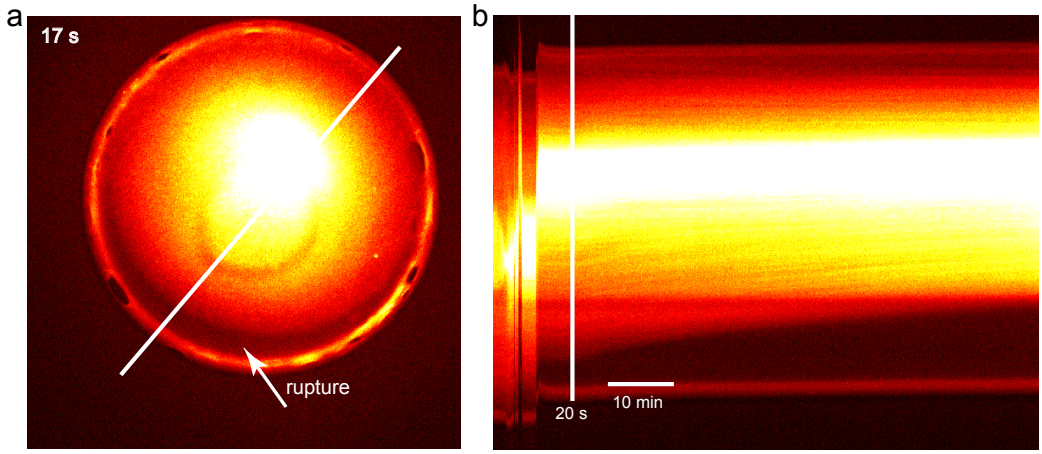

Figure 4.5 **Correlation of rupture at the interface and contraction: (a)** Snapshot of the gap between lipid interface and the contractile actin gel immediately subsequent to perturbation by a pointed capillary (white arrow). **(b)** Kymograph of the white, diagonal bar in (a). Upon perturbation and detachment from the interface the network at concentrations of $10\mu M$ actin, $6\mu M$ anillin and $0.1\mu M$ myosin II contracts without an further external activation. The first 20s (100 frames) are recorded during perturbation at 5 frames/s. The following frames are recorded at 1 frame/5s and the entire kymograph represents a time span of 62 min. The broad bright horizontal stripe results from the fluorescently labelled capillary, that has not been removed from the droplet subsequent to perturbation.

linker density (anillin fragment) at a fixed actin (10 μM) and myosin ($0.1\mu M$) concentration and the density of attachment sites to the interface. If no attachment to the interface is admitted, no mechano-sensitive state can be substantiated.

Besides the critical amount of attachment this mechano-sensitive state is thought to require a sufficiently connected network, which can transmit the contractile stresses exercised by myosin motors without occurring ruptures. The necessitiy of crosslinkers being present for actomyosin contractility is reported by some earlier articles Stendahl and Stossel [1980], Bendix et al. [2008]. Furthermore, solutions of non-connected actin filaments and active molecular motors do not contract at all Humphrey et al. [2002], Köhler et al. [2012]. Macroscopic gel contraction is arrested at high anillin densities, above an anillin/actin ratio of ≈ 0.9. In this regime most of the F-actin is assembled into crosslinked bundles structures exhibiting both a high connectivity and elasticity. Motors present are too weak to induce large scale rearrangements. Qualitatively similar reports are published for reconstitued systems based on actin, myosin II and a different crosslink as filamin A Stendahl and Stossel [1980], Janson et al. [1991] or fascin Kane [1983].

Contraction of crosslinked actomyosin networks are induced by the internal stresses generated by molecular motors. Contraction rates are dependent on the motor density as shown in the last chapter 3. These shrinkage rates have been reported for other systems of bundles of F-actin filaments *in vitro*, where *Dictyostelium* myosin II has been added Tanaka-Takiguchi et al. [2004] or stress fiber in non muscle cells Katoh et al. [1998]. Shrinkage velocities of $0.1–1\mu m/s$ have been measured for these system, which is the same order of magnitude observed here. However, in the case of induced contraction, the contraction velocity is about an order of magnitude less than that. A reason for that might be the increased elastic modulus of the network due to extensive filament elongation and crosslinking, as networks in the perturbed case do not contract spontaneously.

Actomyosin exhibits complex dynamic behaviors in many systems. Organization governing their self-assembly emerge from the tight interplay between contractility, actin turnover and adhesion. Multiple feedbacks between tension, flow, (de-)polymerization and anchorage could explain the various behaviors observed in cells Levayer and Lecuit [2012].

In non-muscle cells contractility is spatially and temporarily regulated at var-

ious length scales from subcellular compartments to tissues. Thereby, regulation is achieved by localization of contractile forces, typically by phosphorylation of myosin II promoting both enzymatic activity and filament assembly. However, the manner in which these forces are transmitted through the cytoskeleton and the response of the actin network to internal stresses will influence the duration and the extent of the cellular shape change and is determined by the network's architecture.

It has been shown that self-organization produce adaptable systems that do not have to rely on complex sensing machinery. The dynamics of actomyosin are directly subjected to the mechanics of their environment. Consequently their steady state localization adjusts to external changes without complex answers including transcription of genes. This is reported for cell migration, where the behavior of the leading edge is permanently adjusted to the substrate mechanics Barnhart et al. [2011].

The dynamics of these contractile networks are dependent on the environment they are embedded in, as shown in chapter 3. With this study it is shown that these boundaries can potentially provide resistance to the internal dynamics. It is likely, that forces sustained at a boundary lead to a build up of internal tension within the active and contractile phase. Ultimately this could play an important role for the self-organization of stress fibers, which occurs at an increased level of tension within adherent cells Aratyn-Schaus et al. [2011].

External cues like chemotaxis have been extensively studied in neutophils or *Dictyostelium*, see Iglesias and Devreotes [2008]. However, even stationary neutrophils located in uniform baths of chemoattractant break symmetry and start moving Zigmond et al. [1981]. This indicates that a directional cue is not required. In addition, nonchemotactic cells, including fish epithelial keratocytes and keratocyte fragments, are able to break symmetry and initiate motility in the absence of external cues Yam et al. [2007]. There, symmetry breaking is associated with rearrangement of actin polymerization and actin network flow patterns. The forces generated by myosin-dependent actin flow are transmitted to the substrate by adhesion complexes, but the manner in which adhesions contribute to symmetry breaking is not well understood. The reconstituted model system presented here shows that internal variations in the network-boundary adhesion can contribute

to the reorganization of actin networks.

5 Surface tension of vesicles

Mechanics of cortices play an important role for the fate of cells Salbreux et al. [2012]. Actions including exo-/endocytosis, spreading, rounding-up before cytokinesis are examples of cortical mechanics that are elementary for the cell. The cortex comprises three different components that interact mechanically with each other: A thin, crosslinked meshwork of actin filaments, the plasma membrane and proteins that link the cytoskeleton to the membrane. Various behaviors of the cortex have been reported and examined extensively in literature Leduc et al. [2010], Gauthier et al. [2012]. Among these are blebbing and membrane nanotube formation, which are sensitive to the distribution of mechanical tension within the cortex.

Additionally molecular motors able to pull on F-actin regulate the mechanical properties of the cytoskeletal cortex in concert with crosslinking proteins. It has been shown by local laser ablation of the actin cortex that bleb expansion is driven by intracellular pressure Tinevez et al. [2009] and that there is a critical cortical tension for bleb formation below which bleb growth cannot be induced. The bleb size above this critical tension increases with increasing tension which can be modified by the activity of molecular motors.

Studying the mechanisms of the mentioned behaviors *in vitro* have turned out really challenging, since the contributions of the components are intricately interfering.

In this part of the thesis I want to introduce a technique to measure lipid bilayer tension of vesicles with optical tweezers.

5.1 Theory of Membrane Tubes

By pulling an almost flat piece of membrane at a point by a bead, a narrow tube is formed. As membranes are under tension, the surface of them gets reduced as far as possible. In case of a vesicle the minimum surface configuration is reached when the membrane gets retracted to its original locally almost flat conformation. The connection to the point of pulling is maintained by the narrow tether, which, compared to the GUV exhibits a negligible surface area. The final radius of this tether is set by the balance of the bending rigidity, which resists against the thinning of the tube and the surface tension of the lipid bilayer, that tends to decrease the diameter of the tube.

5.1.1 Free energy of membranes

To study tube formation quantitatively the elastic theory of two-dimensional bilayers has been developed over the last decades Sackmann [1995], Seifert and Lipowsky [1995]. In the earliest work Helfrich [1973], Canham [1970], the membrane is treated as thin sheet and locally characterized by its mean curvature

$$H = \frac{1}{2}\left(\frac{1}{R_1} + \frac{1}{R_2}\right), \tag{5.1}$$

where R_1 and R_2 are the two principal radii of curvature. The energy of the membrane, the so-called Helfrich-Canham free energy, is defined as

$$\mathcal{F}_{\mathrm{H-C}} = \int \left[\frac{\kappa}{2}(2H)^2 - \kappa 2HC_0\right] dA. \tag{5.2}$$

Here κ is the bending rigidity of the membrane and C_0 is its spontaneous curvature. The integral goes over the entire surface of the membrane. The equilibrium shape of the membrane is gained by minimizing Eq. 5.2, while fulfilling system-specific boundary conditions. In case of vesicles with constant membrane area A_0, total volume V_0, the total free energy function, which has to be minimized, becomes:

$$\mathcal{F} = \mathcal{F}_{\mathrm{H-C}} + \sigma A - pV - fL \tag{5.3}$$

with σ as surface tension, p denoting the pressure difference between outside and inside of the vesicle.

5.1.2 Formation of lipid tubes

To obtain the lipid bilayer tension, the point force pulling at the membrane is f and the end-to-end distance of the membrane in this direction is L. The radius R of the lipid tube, one can derive from Eq. 5.3. For a cylinder of R (yielding H=1/2R) and Length L, omitting spontaneous curvatures ($C_0 \to 0$) the free energy reads:

$$\mathcal{F}_{tube} = \left(\frac{\kappa}{2}\frac{1}{R} + \sigma R\right) 2\pi L - fL. \tag{5.4}$$

Minimizing with respect to R results in

$$R_0 = \sqrt{\frac{\kappa}{2\sigma}} \tag{5.5}$$

for the tube radius. Thus, the free energy can be written as

$$\mathcal{F}_{tube} = 2\pi\kappa L/R_0 - fL. \tag{5.6}$$

Consequently the force necessary to hold the tube can be calculated by taking the derivative of $\mathcal{F}_{tube}$ with respect to L equal to zero:

$$f_0 = \frac{2\pi\kappa}{R_0} = 2\pi\sqrt{2\sigma\kappa} \tag{5.7}$$

If a pulling force f larger than f_0 is applied, the free energy becomes negative and the tube grows to infinity. If $f < f_0$, the free energy is positive and the tube retracts.

5.2 Membrane nanotube extrusion

Measuring the apparent tension σ of liposomes is not a straight forward exercise, as any adhesion itself tends to alter the membrane tension. In common assays like

micropipette aspiration Waugh and Evans [1979] the membrane tension is set to a fixed value by the suction pressure. Here σ is calculated from the Laplace Law Waugh and Evans [1979].

$$\sigma = \frac{\Delta P}{2} \frac{r_P}{1 - \frac{r_P}{R}}, \tag{5.8}$$

where R is the radius of the liposome, r_P is the inner radius of the pipette and ΔP is the applied suction pressure.

An approach to reduce perturbation of σ by the measurement procedure is presented here. A custom-built dual-beam optical tweezers set up is built, see Section 2.2.7, where one trapped bead is held fixed while the other trapped bead can be steered by an Acousto-Optic Deflector (AOD). Great unilaminar vesicles, containing 5% Biotin-Lipids are formed with the cDICE-Technique as briefly described in the methods section 2.2.5. Streptavidin coated beads of $2\mu m$ in diameter are attached to the membrane and trapped by the two laser beams. With this two point forces are applied to the vesicle and thereby the contact zone, which would influence the membrane tension of the vesicle is minimized, see Fig. 5.1a. Moving one bead with the AOD at constant velocity leads to the formation of a membrane tether and the force opposing this lipid tube formation is measured from the displacement of the bead from the center of the laser trap. After the initial tether formation, the tether force stays essentially constant as the tube elongated, until in some cases the tether ruptured, see Fig. 5.1b. The tether force ranged between 4 and 10 pN.

5.3 Discussion

In recent studies on biomimetic vesicles containing artificial active and passive actin cortices a polymorphism of blebbing, tether extrusion and shape change gets observed and can be qualitatively explained by protein concentration dependencies, the density of anchoring points between the membrane and the actin network and the activity of molecular motors within the cortical network Loiseau et al. [2016]. To elucidate the underlying mechanisms more quantitatively this pulling assay could be applied to these reconstituted systems to measure the apparent

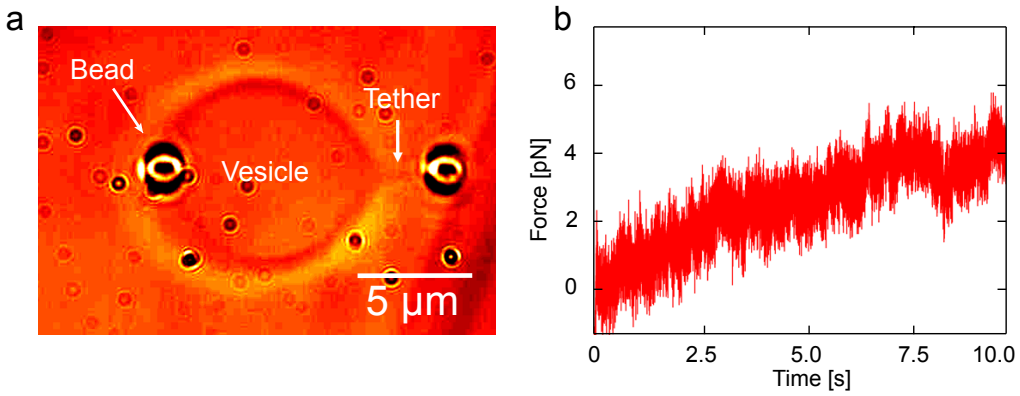

Figure 5.1 **Lipid Tether Formation: (a)** Two bead assay showing the attachment of two beads to a vesicle via a streptavidin biotin bond. The white arrow denotes a lipid tether, which formation is dependent on the surface tension of the vesicle. **(b)** Typical force vs. time curve for the formation of a membrane tube pulled out of a vesicle. The plateau value corresponds to the tube force $f_0 \approx 4pN$.

membrane tension as a sum of the in-plane tension in the bilayer and the adhesion energy between the bilayer and the cytoskeletal network.

6 Microrheology with Optical Tweezers

Efforts to understand the mechanical response of various biopolymer networks at the micro scale have been made by developing several microrheological techniques, which are suited to characterize their viscoelastic behavior. Thereby optical tweezers have been shown to be particularly useful as they offer several advantages and can be employed in active and passive mode. As most microrheological techniques, they rely on the temporal observation of the displacements of small particles. They allow access to local properties of the sample, which for a heterogeneous probe might be very different from the macroscopic and consequently spatially-averaged probes. By suddenly displacing the trap, an embedded particle is subjected to a step-like increase in force. Subsequently the position of the bead is monitored over time. This temporal evolution and the final equilibrium position of the bead allows to calculate viscoelastic properties of the sample. Although this approach does not capture the complete material response across different time scales, it provides a simple description of the material and can be fitted to simple linear viscoelastic systems as the standard linear solid model (sequential arrangement of a spring and a dashpot in parallel with a second spring - see Chapter 2.2.8 characterization for details).

In this chapter the optical trap is used to measure the local elasticity of reconstituted actin cortices, that exhibit nucleation, elongation and crosslinking. In a second part it is used to determine the elastic properties of keratin networks as a function of their concentration.

The actin cytoskeleton is a dynamic network which is able to exhibit different local micro-structures like filopodia or stress fibers. Thereby spatiotemporal control of F-actin polymerization is essential for the specific architecture of the

network. The mutual interplay of filament nucleation, elongation and crosslinking is governed by the presence of auxiliary proteins. It is the rate of nucleation, which determines whether chemically identical polymer networks will be built from sparse and thick or dense and thin bundles Falzone et al. [2013]. Most studies in the field are based on the simultaneous process of nucleation, elongation and bundling. The temporal evolution is then studied by changing the ratios of the individual rates, e.g. by introduction of point mutations at crucial binding sites. Here, a different approach is pursued, where the crosslinkers are added consecutively to the nucleation and elongation of actin. The focus lies on the formation of parallel actin structures grown from a surface. It is shown that the cross-linking process changes the elasticity of these actin networks. Subsequent to the addition of crosslinkers the polymerization is retained by an opposing force, which is provided by the crosslinked scaffold.

For reconstituted intermediate filaments networks, the final network structure is also provided by the inter-dependence of elongation and lateral assembly of their unit length filaments. By addition of salt, keratin filaments - consisting of keratin 8 and keratin 18 proteins - assemble into isotropic networks. In the context of network formation Kayser et al. [2013] showed the rivalry of two independent kinds of association processes to play an important role: filament elongation and their lateral aggregation into bundles. As both of these processes take place at the same time, their interplay governs the assembly dynamics and consequently the initial protein concentration sets the final network structure.

6.1 Elasticity of anisotropic actin networks

It has been shown that the nucleation rate determines the final structure of crosslinked actin networks Falzone et al. [2012], that are far away from thermodynamic equilibrium Schmoller et al. [2008]. In most experimental studies the rates between the network assembly processes are set by the initial conditions, e.g. monomer concentrations of actin, crosslink and nucleator, pH and ionic strength. Thus, it remains elusive how the presence of crosslinks affects the properties of pre-polymerized actin gels or the polymerization itself, when polymerization is spatially confined to a surface. It is shown that crosslinking arrests actin filament

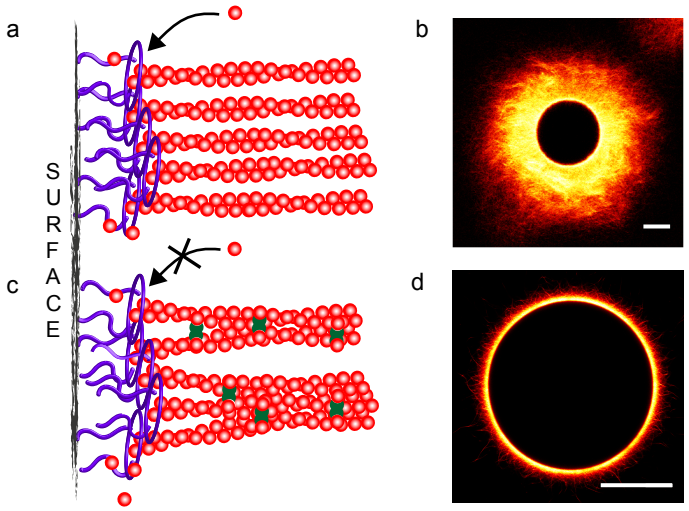

Figure 6.1 **Cortex growth is terminated upon addition of fascin** Schematics of the formin (lilac lassos) moderated actin polymerization with fascin (green) **c** and without **a**. Once Fascin crosslinks parallel oriented F-actin no cortex growth is observed. Confocal images of polydisperse beads with a pure actin cortex **b** and a crosslinked cortex **d**. Scalebars denote 50μm, Fig. adapted from Pelzl [2015]

elongation by changing the mechanics of the growing networks, see Fig. 6.1a,c.

The actin nucleator formin is attached via His-Tag to a NiNTA functionalized spherical surface, where actin monomers (c_{Actin} = 5μM) are incorporated into growing filaments with defined polarity 6.1 b. Competing polymerization in bulk is prevented by the presence of profilin (c_{Profilin} = 10μM) and capping protein c_{Cap} = 0,15μM. Capping protein binds to the barbed end of actin and prevents elongation while polymerization of the pointed end is not feasible for profilin actin Pelzl [2015].

With polymerization at the surface actin filaments are pushed radially outward and form a dense, entangled cortex. The growth of this cortex stops once actin monomers in bulk are depleted to the critical concentration, where off- and on-rates are balanced. Upon further addition of actin monomers cortex growth is resumed. If the cortex is polymerized in the presence of the crosslinker fascin (c_{Actin} = 1μM), a thin layer of dense actin with numerous spikes is formed 6.1 d.

The thickness of the crosslinked actin cortex is dependent on the formin density at the surface and the time point of fascin addition Pelzl [2015]. If fascin is added with a temporal delay towards the initiation of polymerization, it bundles the

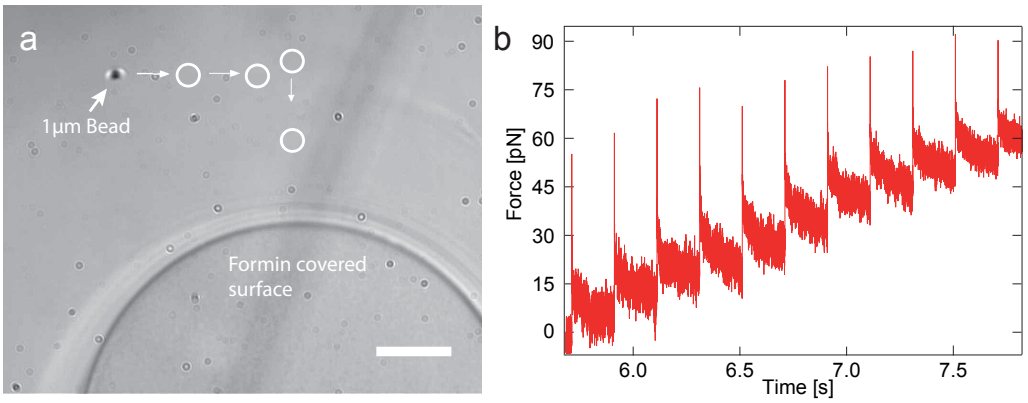

Figure 6.2 **Step strain measurements reveal elasticity of the cortex a**. Bright field image of a NiNTA bead of $\approx 75\mu m$ in diameter and a trapped particle ($\varnothing = 1\mu$ m). White circles represent the paths of radial and tangential path of probing. Scalebar denotes 20μm. **b** and a crosslinked cortex **d**.

actin and consequently contracts the cortex for $\approx 60\%$. Further polymerization of the actin is terminated. Monitoring the network around beads for up to 12 hours shows a constant cortex thickness.

This could imply that the addition of fascin causes an arrest of polymerization, because the crosslinked network is stiffened. Bundling of actin would increase the opposing force at the filament´s barbed end at the bead surface.

To test this hypothesis, the elasticity of the cortex before and after the addition of fascin is measured by optical tweezers. Step strain measurements are performed at initial distances of 12 μm and 20 μm relative to the formin-functionalized surface, see Fig. 6.2a. Typical response curves are shown in Fig. 6.2b. The spike corresponds to the sudden displacement of the bead. For each step the trapped particle gets relaxed to an equilibrium position, where the forces exerted by the trap and the sample are balanced. These forces and the positions, relative to the previous step, are used to calculate Young's modulus E_0 for this particular step - see Sec. 2.2.8. To extract E_0^{tan} in the tangential direction, 70 steps for pure actin cortices and 57 steps for actin-fascin cortices are evaluated.

For pure actin cortices the elasticity reads $E_0^{tan} = 0.14 \pm 0.35$ Pa, see Fig. 6.3 left blue bar. This is comparable to micro-rheological data, which for actin concentrations of 24μM shows a plateau value $G_0 = 0.2$ Pa Gardel et al. [2003]. However in

the system studied here, the local concentration of actin within the cortex is much higher as the bulk concentration, so the Young's modulus measured in the cortex should be even higher as well.

For the fascin cortex a tangential Young's modulus of E_0^{tan} = 4.3 ± 2.4 Pa is measured, see Fig. 6.3 left green bar. According to the concentrations used in this assay, a plateau modulus of $G_0 \approx 6$ Pa has been measured in macrorheology Lieleg et al. [2007], which is in the same order of magnitude. However it has to be taken into account that the local actin concentration in the cortex is higher. If it is assumed that cortices contain a few hundred micro-molar and that the ratio of fascin is between 0.1 and 0.2, this would yield an elastic plateau modulus $G' \approx c_a^{2.4}$ on the order of a few kPa, which is different compared to our data. Thereby the power law measured by Lieleg et al. [2007] is extrapolated. Additionally the elasticity of the actin network depends on the ratio R of fascin to actin, as it is shown by Lieleg et al. [2007] and co-workers. In the current assay fascin is added after or during polymerization of actin. Consequently the distribution of fascin happens mostly by diffusion and can not be regarded homogeneous Pelzl [2015]. Taking this into account the elasticity of the cortices depend on the amount of crosslinkers and with that on their location in the sample.

The striking difference of the cortices to the macrorheological bulk systems is the architecture of the networks. While the bulk network is isotropic, here the filaments grow radially outward and are consequently oriented parallel to one another. This could imply an anisotropic mechanical response for tangential and radial directions. To test this hypothesis step strain measurements in radial directions are employed. For the pure actin cortex the elasticity is $E_0^{rad} = 0.005 \pm 0.25$ Pa, Fig. 6.3 right blue bar, while for the fascin cortex it reads E_0^{rad} = 1.0 ± 1.6 Pa, Fig. 6.3 right green bar. Both values are below the ones in the tangential direction, which indeed indicates an anisotropic response of the crosslinked cortices.

6.2 Elasticity of isotropic keratin networks

Motivated by mechanical studies on networks of actin, where the rheological answer has been shown to depend on the meshsize, the mechanical properties of keratin networks should also depend on their meshsize.

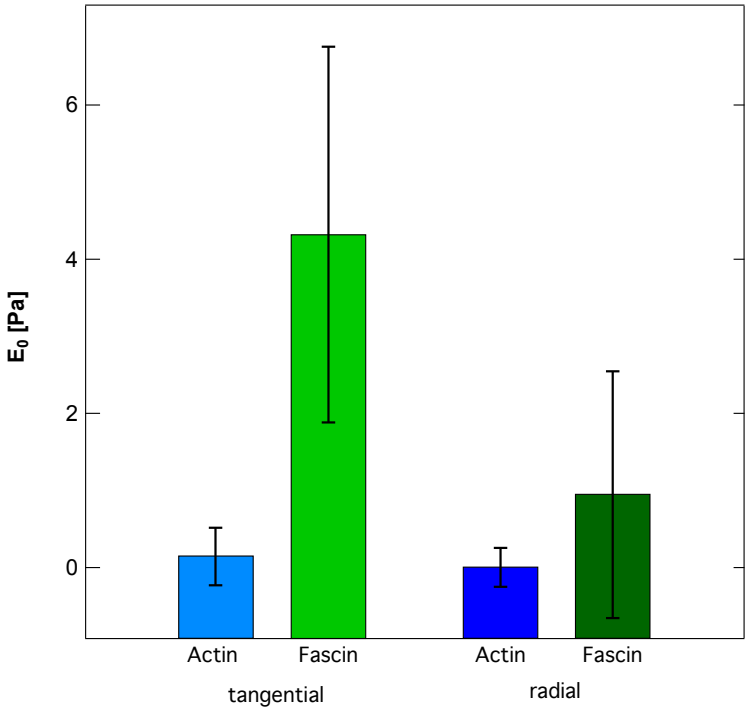

Figure 6.3 **Anisotropic elasticities measured by optical tweezers setup** Results are shown for radial and tangential directions, respectively for both pure actin cortices and cross-linked actin-fascin cortices.

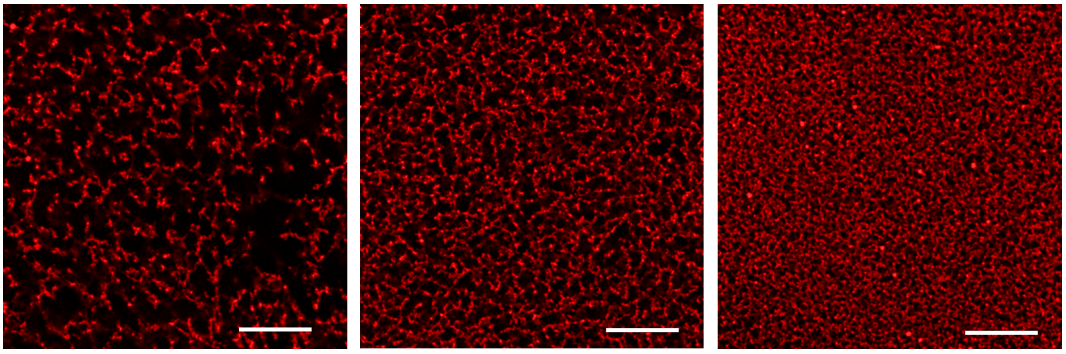

Figure 6.4 **Initial concentration of Keratin proteins set the meshsize of the resulting network structure:** Confocal images of networks at concentrations of c_K = 6μM (left), c_K = 9μM and c_K = 12μM - scale bar denotes 50μm

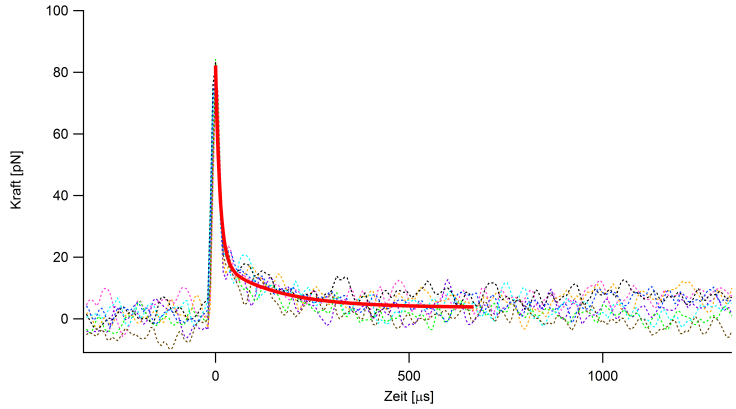

Figure 6.5 **Double exponential decay of the force to the averaged plateau value of 9 pN** Overlay of 8 peaks of a step strain measurement within a network consisting of 9 μM. Red thick line represents the fit of the averaged data to equation 6.1

In Fig. 6.4 three different final structures are shown. With increasing protein concentration the characteristic meshsize ξ decreases, as shown in Kayser et al. [2012]. Networks containing 4 different monomer concentrations and a constant dilution of 1μm sized beads, are assembled: 7 μM, 9 μM,11 μM and 13 μM. Step strain measurements, described in 2.2.7.1.3 and 2.2.8, show a double exponential relaxation of the force signal according to equation 6.1, see Fig. 6.5.

$$F(t) = F_2 \cdot exp\left(\frac{-(t-t_0)}{\tau_{H_2O}}\right) + F_1 \cdot exp\left(\frac{-(t-t_0)}{\tau}\right) + F_0. \tag{6.1}$$

Briefly the first and fast relaxation describes the response of the bead in buffer and is considered a strain step, accomplished after τ_{H_2O}.

Every single force peak within the linear stress-strain-regime is monitored and fit with the parameters F_2, F_1, F_0, τ_{Network} and τ_{H_2O}. Using these parameter the two elastic moduli E_0, E_1 and the viscosity η are calculated, see 2.2.8

$$E_0 = \frac{\tilde{F}_0}{6\pi R_{\text{bead}} \Delta l}, \tag{6.2}$$

$$E_1 = \frac{\tilde{F}_1 \cdot \exp\left(-\frac{\tau_{H_2O}}{\tau_{\text{Network}}}\right)}{6\pi R_{\text{bead}} \Delta l}, \tag{6.3}$$

$$\eta = \tau_{\text{Network}} \cdot E_1 \tag{6.4}$$

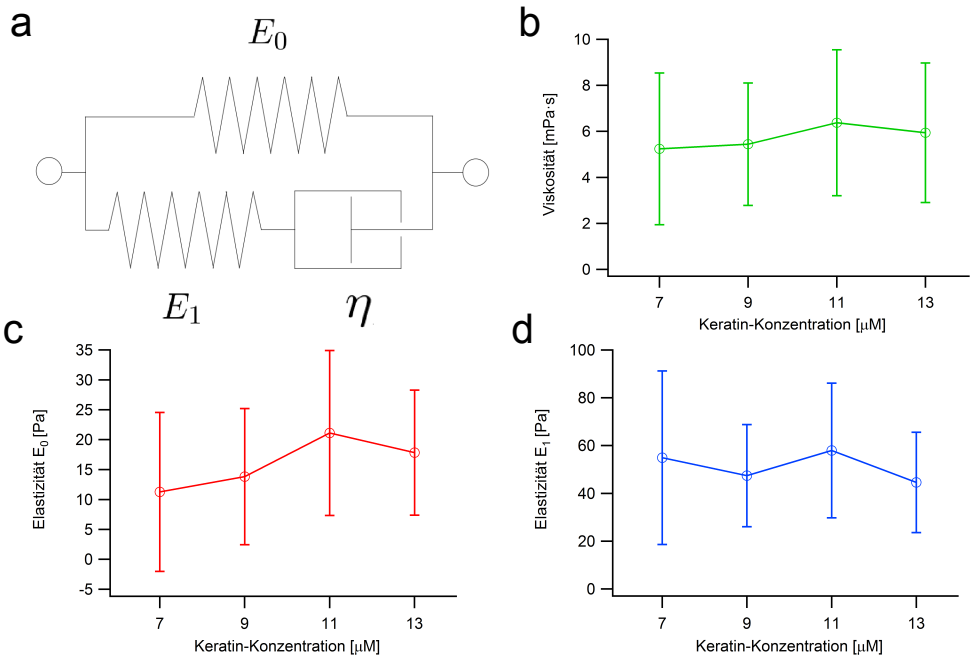

Figure 6.6 **Elastic properties are independent of meshsize** Mean values according to (**a**) the SLS model of (**b**) η, (**c**) E_0 and (**d**) E_1. The standard deviation of the values are large, because of the heterogeneous substructure of arrested networks

The exponential factor in Equation 6.3 corrects the force amplitude F_1 to the value it obtains after the intercalation time τ_{H_2O} of the switching to the new step. $\tilde{F}$ is the offset-corrected plateau value, see 2.2.7.1.3. According to the Poynting model E_1 is the elasticity that gets relaxed via η during τ_{Network}, while E_0 is tensed for $t \to \infty$ and entails the continuous, linear increase of the stress level.

Macrorheological measurements on a commercial Anton Paar setup Deek et al. show that the plateau value G_0 of the elastic shear modulus G', which describes the elasticity at low frequencies, in $c_K \in [10{,}15]\mu$M is between $1 \leq G_0 \leq 5$Pa. Since the plateau value relates to Young's modulus $G_0 = E_0/2(1+\nu) = E_0/3$ for incompressible materials of Poisson's number $\nu = 0.5$, the values obtained here are in good agreement.

While keratin networks exhibit a homogeneous morphology on length scales above $5\mu m$, EM and STED images particularly reveal a heterogeneous substructure Kayser et al. [2012]. This is due to the previously mentioned simultaneous elongation and crosslinking of keratin filaments, which results in a kinetically ar-

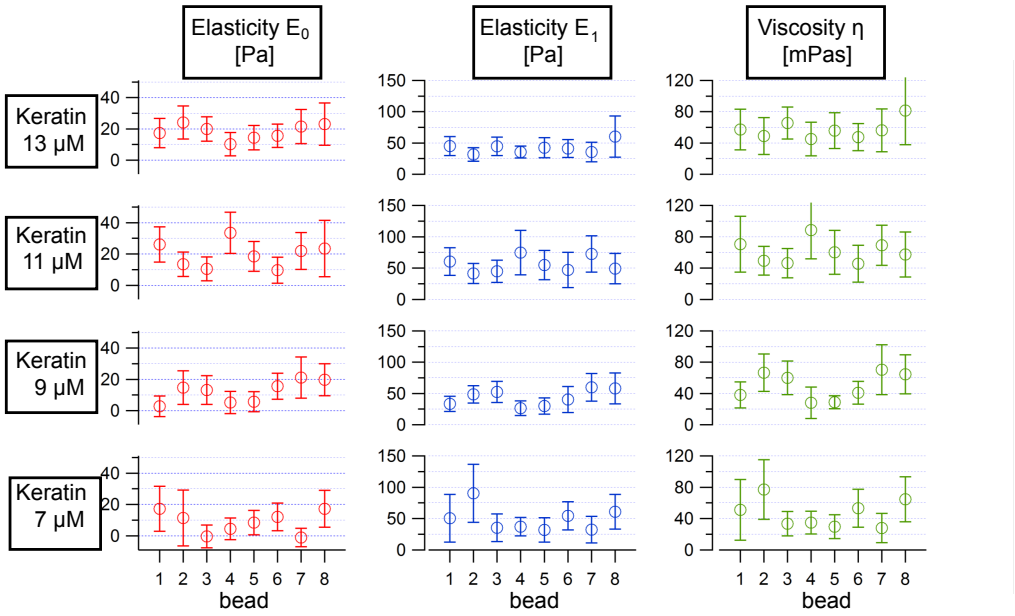

Figure 6.7 **Mean values of E_0, E_1 and η for 8 different spots within the same network**
Error bars represent the standard deviation of the mean values.

rested cluster bundle phase. As the beads used here with 1μm diameter are on the size scale of single clusters, this could imply that the rather large variation of the moduli in Fig. 6.6, where all measurements have been pooled, is a consequence of averaging these heterogeneous, local properties of the networks. To account for that in Fig. 6.7 the obtained values are broken down to a single spot within the network. This shows the expected strong variation of the network parameters. In contrast, the uncertainty for measurements of a single bead is lower, since the averaged standard deviation is smaller by a factor of ≈ 2.

Moreover for increasing keratin concentrations the spatial variations of mechanical answers decrease, indicating an increasing homogeneity of the network, see table 6.1.

Concentration	7 [μM]	9 [μM]	11 [μM]	13[μM]
Deviation of mean E_0	82.7%	58.4%	39.2%	26.0%
Deviation of mean E_1	40.5%	29.7%	42.5%	21.0%
Deviation of mean η	38.7%	35.3%	24.0%	20.6%

Table 6.1 **With increasing keratin concentration the mechanical network answer gets more homogeneous** Standard deviations of the mean values decrease with decreasing mesh size.

6.3 Discussion

The microrheological step strain methodology is outlined and described in chapter 2.2.8 and used to measure viscoelastic properties of reconstituted isotropic and anisotropic cytoskeletal networks. As demonstrated by these applications optical tweezers are a convenient tool to study heterogeneous samples locally without averaging over a large sample volume. However, if used for microrheoloy, important considerations have to be taken into account. Bead size, material and surface chemistry will govern interactions with the surrounding medium of interest. Bead surface chemistries might create depletion zones around the bead, effectively isolating the bead from the sample of interest. The bead material sets its index of refraction, which in turn determines the stiffness of the trap and the maximal force, that can be applied.

Another important point to consider is the geometry and the size of the sample chamber. Local heating due to the impact of the infrared laser could lead to strong convection, which leads to drift in the sample. To decrease convection issues it might be helpful to decrease the dimension of the sample chamber in direction of the beam as far as possible Peterman et al. [2003].

The stiffness of the trap should match the purpose of the measurement: the stiffness is dependent on the power of the trapping laser and the refraction index mismatch between the bead and the surrounding medium. If the trap is relatively stiff compared to the storage modulus of the surrounding medium, the measured values of the sample will be inaccurate. On the other hand, stiff traps are important especially for active microrheological techniques used here. The beads are dragged through the material of interest and require relatively large forces to deform it. The application of large strains might additionally trigger the onset of non-linear

behavior.

7 Outlook

The main goal of this thesis was to establish model systems to investigate the effect of boundaries for cytoskeletal organization. With the unraveling of the impact of boundaries for a contracting actomyosin network in bulk, these effects have already demonstrated their significance. Establishing a technique to measure the effective membrane tension of vesicles containing cytoskeletal components allows to investigate the role of boundaries in a reconstituted environment, reminiscent of cellular confinement. In the following some future perspectives on the follow-up studies of these organization principles will be given.

Studying the contractions of minimal reconstituted systems in bulk is important to unravel physical mechanisms governing dynamics of reorganization, these assays lack the mechanical constraints present in the cellular cytoskeleton. Minimal model systems encapsulated in unilamellar vesicles of different sizes are well-suited candidates to address confinement effects for active actin networks. Thereby vesicles with various lipid compositions might help to carve out the role of the membrane to cytoskeletal organization and dynamics Saarikangas et al. [2010].

In chapter 5 a method has been introduced to measure the apparent surface tension of a GUV. Application of a point force results in the formation of a lipid tube characterized by the tube force $f_{\text{tube}} = 2\pi\sqrt{2\kappa\gamma}$. Loiseau and co-workers established a technique to assemble reconstituted cortices in vesicles of controlled size. Thereby they reconstructed actomyosin vesicles in which the coupling of the cytoskeleton to the membrane, the topology of the cytoskeletal network, and the contractile activity can all be precisely controlled and tuned Loiseau et al. [2016]. Depending on the density of attachment sites and crosslinker concentrations they observe a rich phase behavior, including bulk vs network morphologies, blebbing and vesicularization. These shape transformations are reminiscent dynamic behaviors observed in cells, albeit a more concerted organization of active forces seems

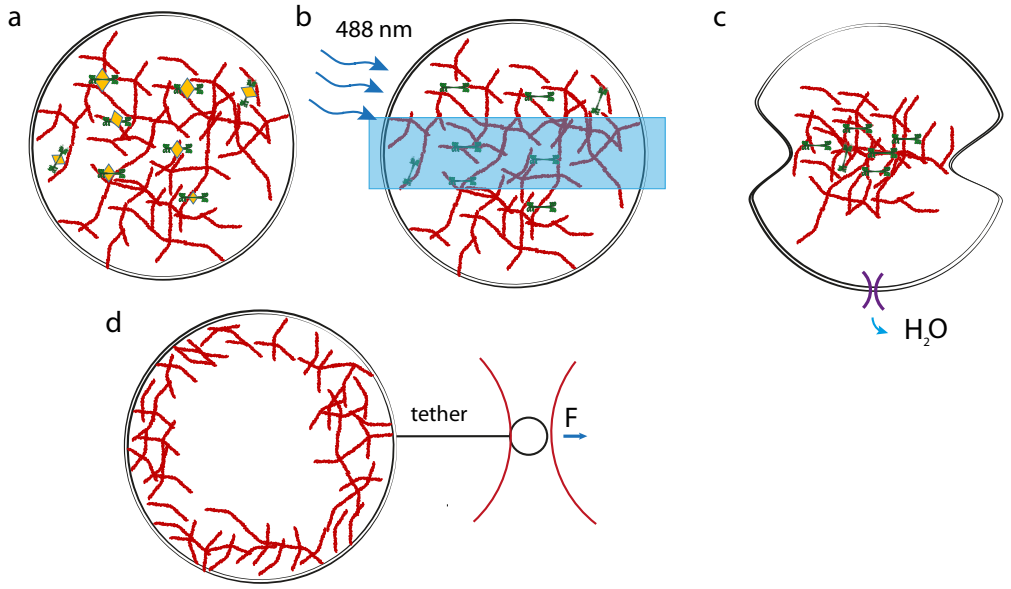

Figure 7.1 **Mechanics of active actin networks in liposomes**Light activated contraction in vesicles with tunable geometry **(a)** Initially blebbistatin (yellow diamonds) prevents rearrangements of molecular motors (green) resulting in a filamentous actin network (red curves) **(b)** Illumination of gel with blue light (blue arrows) inactivates blebbistatin. Consequently motors are activated with a precisely controlled geometry inside the liposom **(c)** Large scale rearrangements reminiscent of cellular dynamics (e.q. cytokinesis) could be studied, if aquaporins were incorporated into the membrane to release pressure. **(d)** A footprint of different network morphologies encapsulated in the vesicle should be the tube force, that can be measured by means of optical tweezers.

important in living cells Almeida et al. [2011], Miserey-Lenkei et al. [2010].

Because of the coupling between the network and the membrane, the network cannot rearrange freely. Contractions are instead constrained by the membrane being pulled against the volume of the vesicle. Consequently, mentioned behaviors should add specific contributions to the tube force of empty vesicles. This would allow to account quantitatively for mechanical properties inside the vesicle, which might be a valuable tool to gain deeper insight on the mechanics of active, cell-sized, biomimetic vesicles.

In chapter 3 it has been demonstrated that inactivation of blebbistatin is a valuable tool to control motor activity in space and time. The light induced transition from passive to active state could also be employed to switch motors embedded in vesicles from a non-contractile to a contractile state. This technique can be used to

separate cortex/network formation and force generation onto different time scales.

Bibliography

Elio A Abbondanzieri, William J Greenleaf, Joshua W Shaevitz, Robert Landick, and Steven M Block. Direct observation of base-pair stepping by rna polymerase. *Nature*, 438(7067):460–465, 2005. (Cited on page 15.)

Manouk Abkarian, Etienne Loiseau, and Gladys Massiera. Continuous droplet interface crossing encapsulation (cdice) for high throughput monodisperse vesicle design. *Soft Matter*, 7(10):4610–4614, 2011. (Cited on page 13.)

Antonina Y Alexandrova, Katya Arnold, Sébastien Schaub, Jury M Vasiliev, Jean-Jacques Meister, Alexander D Bershadsky, and Alexander B Verkhovsky. Comparative dynamics of retrograde actin flow and focal adhesions: formation of nascent adhesions triggers transition from fast to slow flow. *PloS one*, 3(9): e3234–e3234, 2008. (Cited on page 60.)

Claudia G Almeida, Ayako Yamada, Danièle Tenza, Daniel Louvard, Graça Raposo, and Evelyne Coudrier. Myosin 1b promotes the formation of post-golgi carriers by regulating actin assembly and membrane remodelling at the trans-golgi network. *Nature cell biology*, 13(7):779–789, 2011. (Cited on page 92.)

José Alvarado, Michael Sheinman, Abhinav Sharma, Fred C MacKintosh, and Gijsje H Koenderink. Molecular motors robustly drive active gels to a critically connected state. *Nat. Phys.*, 9(9):591–597, 2013. (Cited on pages 3, 38, and 62.)

Yvonne Aratyn-Schaus, Patrick W Oakes, and Margaret L Gardel. Dynamic and structural signatures of lamellar actomyosin force generation. *Molecular biology of the cell*, 22(8):1330–1339, 2011. (Cited on page 70.)

Arthur Ashkin, JM Dziedzic, JE Bjorkholm, and Steven Chu. Observation of a

single-beam gradient force optical trap for dielectric particles. *Optics letters*, 11 (5):288–290, 1986. (Cited on page 15.)

F. Backouche, L. Haviv, D. Groswasser, and A. Bernheim-Groswasser. Active gels: dynamics of patterning and self-organization. *Phys. Biol.*, 3(4):264, 2006. (Cited on pages 3 and 38.)

M. Ballerini, N. Cabibbo, R. Candelier, A. Cavagna, E. Cisbani, I. Giardina, A. Orlandi, G. Parisi, A. Procaccini, M. Viale, and V. Zdravkovic. Empirical investigation of starling flocks: a benchmark study in collective animal behaviour. *Animal Behaviour*, 76:201–215, 2008a. (Cited on page 55.)

M. Ballerini, N. Cabibbo, R. Candelier, A. Cavagna, E. Cisbani, I. Giardina, A. Orlandi, G. Parisi, A. Procaccini, M. Viale, and V. Zdravkovic. Interaction ruling animal collective behavior depends on topological rather than metric distance: Evidence from a field study. *Proc. Natl. Acad. Sci.*, 105:1232–1237, 2008b. (Cited on page 55.)

Erin Barnhart, Kun-Chun Lee, Greg M Allen, Julie A Theriot, and Alex Mogilner. Balance between cell- substrate adhesion and myosin contraction determines the frequency of motility initiation in fish keratocytes. *Proceedings of the National Academy of Sciences*, 112(16):5045–5050, 2015. (Cited on page 61.)

Erin L Barnhart, Kun-Chun Lee, Kinneret Keren, Alex Mogilner, and Julie A Theriot. An adhesion-dependent switch between mechanisms that determine motile cell shape. *PLoS Biol*, 9(5):e1001059, 2011. (Cited on page 70.)

AR Bausch and K Kroy. A bottom-up approach to cell mechanics. *Nature physics*, 2(4):231–238, 2006. (Cited on pages 37 and 65.)

Poul M Bendix, Gijsje H Koenderink, Damien Cuvelier, Zvonimir Dogic, Bernard N Koeleman, William M Brieher, Christine M Field, L Mahadevan, and David A Weitz. A quantitative analysis of contractility in active cytoskeletal protein networks. *Biophys. J.*, 94(8):3126–3136, 2008. (Cited on pages 3, 37, 62, and 69.)

Kirstine Berg-Sørensen and Henrik Flyvbjerg. Power spectrum analysis for optical tweezers. *Rev. Scient. Instr.*, 75(3):594–612, 2004. (Cited on page 19.)

J Berthelot, SS Acimovic, ML Juan, MP Kreuzer, J Renger, and R Quidant. 3d manipulation with scanning near field optical nanotweezers. *arXiv preprint arXiv:1311.1740*, 2013. (Cited on page 15.)

Laurent Blanchoin, Rajaa Boujemaa-Paterski, Cécile Sykes, and Julie Plastino. Actin dynamics, architecture, and mechanics in cell motility. *Physiological reviews*, 94(1):235–263, 2014. (Cited on pages 1 and 37.)

Bernhard Brenner and Evan Eisenberg. Rate of force generation in muscle: correlation with actomyosin atpase activity in solution. *Proceedings of the National Academy of Sciences*, 83(10):3542–3546, 1986. (Cited on page 10.)

ES Bullitt, David J DeRosier, Lynne M Coluccio, and Lewis G Tilney. Three-dimensional reconstruction of an actin bundle. *J. Cell Biol.*, 107(2):597–611, 1988. (Cited on page 7.)

Peter B Canham. The minimum energy of bending as a possible explanation of the biconcave shape of the human red blood cell. *Journal of Theoretical Biology*, 26(1):61–81, 1970. (Cited on page 74.)

M. M. A. E. Claessens, C. Semmrich, L. Ramos, and A. R. Bausch. Helical twist controls the thickness of F-actin bundles. *Proc. Natl. Acad. Sci. USA*, 105 (26): 8819–8822, 2008. (Cited on page 8.)

Jennifer E Curtis, Brian A Koss, and David G Grier. Dynamic holographic optical tweezers. *Optics Communications*, 207(1):169–175, 2002. (Cited on page 15.)

J. Deek, F. Hecht, L. Rossetti, and A. Bausch. Modulating structure and mechanics of keratin networks by site-specific phosphorylation. (Cited on page 86.)

Tobias T Falzone, Martin Lenz, David R Kovar, and Margaret L Gardel. Assembly kinetics determine the architecture of α-actinin crosslinked f-actin networks. *Nature communications*, 3:861, 2012. (Cited on page 80.)

Tobias T Falzone, Patrick W Oakes, Jennifer Sees, David R Kovar, and Margaret L Gardel. Actin assembly factors regulate the gelation kinetics and architecture of f-actin networks. *Biophysical journal*, 104(8):1709–1719, 2013. (Cited on page 80.)

Wallace O Fenn. A quantitative comparison between the energy liberated and the work performed by the isolated sartorius muscle of the frog. *The Journal of Physiology*, 58(2-3):175–203, 1923. (Cited on page 61.)

ML Gardel, MT Valentine, John C Crocker, AR Bausch, and DA Weitz. Microrheology of entangled f-actin solutions. *Physical review letters*, 91(15):158302, 2003. (Cited on page 82.)

Nils C Gauthier, Thomas A Masters, and Michael P Sheetz. Mechanical feedback between membrane tension and dynamics. *Trends in cell biology*, 22(10):527–535, 2012. (Cited on page 73.)

Alan A Griffith. The phenomena of rupture and flow in solids. *Philosophical transactions of the royal society of london. Series A, containing papers of a mathematical or physical character*, 221:163–198, 1921. (Cited on page 39.)

L. Haviv, D. Gillo, F. Backouche, and A. Bernheim-Groswasser. A cytoskeletal demolition worker: Myosin ii acts as an actin depolymerization agent. *J. Mol. Biol.*, 375:325–330, 2008. (Cited on page 60.)

Wolfgang Helfrich. Elastic properties of lipid bilayers: theory and possible experiments. *Zeitschrift für Naturforschung C*, 28(11-12):693–703, 1973. (Cited on page 74.)

Harald Herrmann, Markus Häner, Monika Brettel, Nam-On Ku, and Ueli Aebi. Characterization of distinct early assembly units of different intermediate filament proteins. *Journal of molecular biology*, 286(5):1403–1420, 1999. (Cited on page 11.)

Claus Heussinger. Stress relaxation through crosslink unbinding in cytoskeletal networks. *New Journal of Physics*, 14(9):095029, 2012. (Cited on page 39.)

Nobutaka Hirokawa. Kinesin and dynein superfamily proteins and the mechanism of organelle transport. *Science*, 279(5350):519–526, 1998. (Cited on page 1.)

D Humphrey, C Duggan, D Saha, D Smith, and J Käs. Active fluidization of polymer networks through molecular motors. *Nature*, 416(6879):413–416, 2002. (Cited on page 69.)

Andrew F Huxley and Ro M Simmons. Proposed mechanism of force generation in striated muscle. *Nature*, 233(5321):533–538, 1971. (Cited on page 61.)

Pablo A Iglesias and Peter N Devreotes. Navigating through models of chemotaxis. *Current opinion in cell biology*, 20(1):35–40, 2008. (Cited on page 70.)

Ryoki Ishikawa, Takeshi Sakamoto, Toshio Ando, Sugie Higashi-Fujime, and Kazuhiro Kohama. Polarized actin bundles formed by human fascin-1: their sliding and disassembly on myosin ii and myosin v in vitro. *Journal of neurochemistry*, 87(3):676–685, 2003. (Cited on page 38.)

Lee W Janson, John Kolega, and D Lansing Taylor. Modulation of contraction by gelation/solation in a reconstituted motile model. *The Journal of cell biology*, 114(5):1005–1015, 1991. (Cited on page 69.)

RE Kane. Interconversion of structural and contractile actin gels by insertion of myosin during assembly. *The Journal of cell biology*, 97(6):1745–1752, 1983. (Cited on page 69.)

Kazuo Katoh, Yumiko Kano, Michitaka Masuda, Hirofumi Onishi, and Keigi Fujiwara. Isolation and contraction of the stress fiber. *Molecular Biology of the Cell*, 9(7):1919–1938, 1998. (Cited on page 69.)

Jona Kayser, Heinrich Grabmayr, Markus Harasim, Harald Herrmann, and Andreas R Bausch. Assembly kinetics determine the structure of keratin networks. *Soft Matter*, 8(34):8873–8879, 2012. (Cited on pages 14, 85, and 86.)

Jona Kayser et al. *Non-equilibrium Effects in Cytoskeletal Networks*. PhD thesis, Technische Universität München, 2013. (Cited on page 80.)

MW Kilimann and G Isenberg. Actin filament capping protein from bovine brain. *The EMBO journal*, 1(7):889, 1982. (Cited on page 8.)

Gijsje H Koenderink, Zvonimir Dogic, Fumihiko Nakamura, Poul M Bendix, Frederick C MacKintosh, John H Hartwig, Thomas P Stossel, and David A Weitz. An active biopolymer network controlled by molecular motors. *Proceedings of the National Academy of Sciences*, 106(36):15192–15197, 2009. (Cited on page 3.)

S. Köhler and A. R. Bausch. Contraction mechanisms in composite active actin networks. *PLoS One*, 7(7), 2012. (Cited on pages 38 and 60.)

Simone Köhler, Volker Schaller, and Andreas R. Bausch. Structure formation in active networks. *Nat. Mater.*, 10(6):462–468, 2011. (Cited on pages 3 and 37.)

Simone Köhler, Kurt M Schmoller, Alvaro H Crevenna, and Andreas R Bausch. Regulating contractility of the actomyosin cytoskeleton by ph. *Cell reports*, 2 (3):433–439, 2012. (Cited on pages 3, 62, and 69.)

J. Kolega. Phototoxicity and photoinactivation of blebbistatin in UV and visible light. *Biochem. Biophys. Res. Commun.*, 320:1020–1025, 2004. (Cited on page 11.)

M. Kovács, J. Toth, C. Hetenyi, A. Malnasi-Csizmadia, and J. R. Sellers. Mechanism of blebbistatin inhibition of myosin II. *J. Biol. Chem.*, 279:35557–35563, 2004. (Cited on page 11.)

David R Kovar and Thomas D Pollard. Insertional assembly of actin filament barbed ends in association with formins produces piconewton forces. *Proceedings of the National Academy of Sciences of the United States of America*, 101(41): 14725–14730, 2004. (Cited on page 9.)

David R Kovar, Elizabeth S Harris, Rachel Mahaffy, Henry N Higgs, and Thomas D Pollard. Control of the assembly of atp-and adp-actin by formins and profilin. *Cell*, 124(2):423–435, 2006. (Cited on page 9.)

Cécile Leduc, Otger Campàs, Jean-François Joanny, Jacques Prost, and Patricia Bassereau. Mechanism of membrane nanotube formation by molecular motors.

Biochimica et Biophysica Acta (BBA)-Biomembranes, 1798(7):1418–1426, 2010. (Cited on page 73.)

Martin Lenz, Todd Thoresen, Margaret L Gardel, and Aaron R Dinner. Contractile units in disordered actomyosin bundles arise from F-actin buckling. *Phys. Rev. Lett.*, 108(23):238107, 2012. (Cited on page 46.)

Romain Levayer and Thomas Lecuit. Biomechanical regulation of contractility: spatial control and dynamics. *Trends in cell biology*, 22(2):61–81, 2012. (Cited on page 69.)

O. Lieleg, M. M. A. E. Claessens, C. Heussinger, E. Frey, and A. R. Bausch. Mechanics of bundled semiflexible polymer networks. *Phys. Rev. Lett.*, 99:088102, 2007. (Cited on pages 65 and 83.)

O. Lieleg, M. M. A. E. Claessens, Y. Luan, and A. R. Bausch. Transient binding and dissipation in semi-flexible polymer networks. *Phys. Rev. Lett.*, 101:108101, 2008. (Cited on page 65.)

O Lieleg, J Kayser, Giovanni Brambilla, Luca Cipelletti, and AR Bausch. Slow dynamics and internal stress relaxation in bundled cytoskeletal networks. *Nature materials*, 10(3):236–242, 2011. (Cited on pages 38 and 65.)

Zhi-Qiang Liu. Scale space approach to directional analysis of images. *Applied optics*, 30(11):1369–1373, 1991. (Cited on page 13.)

Etienne Loiseau, Jochen AM Schneider, Felix C Keber, Carina Pelzl, Gladys Massiera, Guillaume Salbreux, and Andreas R Bausch. Shape remodeling and blebbing of active cytoskeletal vesicles. *Science Advances*, 2(4):e1500465, 2016. (Cited on pages 76 and 91.)

Susan MacLean-Fletcher and Thomas D. Pollard. Identification of a factor in conventional muscle actin preparations which inhibits actin filament self-association. *Biochem. Biophys. Res. Commun.*, 96(1):18–27, 1980. (Cited on page 7.)

Amy Shaub Maddox, Lindsay Lewellyn, Arshad Desai, and Karen Oegema. Anillin and the septins promote asymmetric ingression of the cytokinetic furrow. *Developmental cell*, 12(5):827–835, 2007. (Cited on page 8.)

Vincent Maier. Charakterisierung von keratin mit der optischen pinzette. 2014. (Cited on page 36.)

Pierre Mangeol and Ulrich Bockelmann. Interference and crosstalk in double optical tweezers using a single laser source. *Review of Scientific Instruments*, 79 (8):083103, 2008. (Cited on page 26.)

Sarkis S. Margossian and Susan Lowey. Preparation of myosin and its subfragments from rabbit skeletal muscle. *Meth. Enzymology*, 85:55–71, 1982. (Cited on page 11.)

S Miserey-Lenkei, G Chalancon, S Bardin, E Formstecher, B Goud, and A Echard. Rab and actomyosin-dependent fission of transport vesicles at the golgi complex. *Nature cell biology*, 12(7):645–654, 2010. (Cited on page 92.)

TJ Mitchison and LP Cramer. Actin-based cell motility and cell locomotion. *Cell*, 84(3):371–379, 1996. (Cited on page 1.)

Daisuke Mizuno, Catherine Tardin, CF Schmidt, and FC MacKintosh. Nonequilibrium mechanics of active cytoskeletal networks. *Science*, 315(5810):370–373, 2007. (Cited on page 15.)

Alex Mogilner and Kinneret Keren. The shape of motile cells. *Current Biology*, 19(17):R762–R771, 2009. (Cited on pages 1 and 37.)

Akankshi Munjal and Thomas Lecuit. Actomyosin networks and tissue morphogenesis. *Development*, 141(9):1789–1793, 2014. (Cited on pages 37 and 60.)

Michael Murrell, Patrick W Oakes, Martin Lenz, and Margaret L Gardel. Forcing cells into shape: the mechanics of actomyosin contractility. *Nat. Rev. Molec. Cell Biol.*, 16(8):486–498, 2015. (Cited on pages 1, 2, and 37.)

Michael P Murrell and Margaret L Gardel. F-actin buckling coordinates contractility and severing in a biomimetic actomyosin cortex. *Proceedings of the National Academy of Sciences*, 109(51):20820–20825, 2012. (Cited on page 60.)

Patrick W Oakes, Shiladitya Banerjee, M Cristina Marchetti, and Margaret L Gardel. Geometry regulates traction stresses in adherent cells. *Biophysical journal*, 107(4):825–833, 2014. (Cited on page 60.)

S. Ono, Y. Yamakita, S. Yamashiro, P. T. Matsudaira, J. R. Gnarra, T. Obinata, and F. Matsumura. Identification of an actin binding region and a protein kinase c phosphorylation site on human fascin. *J. Biol. Chem.*, 272:2527–2533, 1997. (Cited on page 8.)

D. A. Paley and A. K. Baharani. Critical damping in a kinetic interaction network. *Proc. Amer. Control Conf.*, pages 4628–4633, 2010. (Cited on page 55.)

Carina Pelzl. *In vitro studies of cytoskeletal structure formation*. PhD thesis, München, Technische Universität München, Diss., 2015, 2015. (Cited on pages 81 and 83.)

Erwin JG Peterman, Frederick Gittes, and Christoph F Schmidt. Laser-induced heating in optical traps. *Biophysical journal*, 84(2):1308–1316, 2003. (Cited on pages 20 and 88.)

Thomas D Pollard and Gary G Borisy. Cellular motility driven by assembly and disassembly of actin filaments. *Cell*, 112(4):453–465, 2003. (Cited on pages 1 and 5.)

Thomas D Pollard and John A Cooper. Actin, a central player in cell shape and movement. *Science*, 326(5957):1208–1212, 2009. (Cited on page 1.)

Thomas D Pollard, William C Earnshaw, and Jennifer Lippincott-Schwartz. *Cell biology*. Elsevier Health Sciences, 2007. (Cited on page 9.)

J Prost, F Jülicher, and JF Joanny. Active gel physics. *Nat. Phys.*, 11(2):111–117, 2015. (Cited on page 37.)

Yixin Ren, Janet C Effler, Melanie Norstrom, Tianzhi Luo, Richard A Firtel, Pablo A Iglesias, Ronald S Rock, and Douglas N Robinson. Mechanosensing through cooperative interactions between myosin ii and the actin crosslinker cortexillin i. *Current Biology*, 19(17):1421–1428, 2009. (Cited on page 4.)

Anne J Ridley. Life at the leading edge. *Cell*, 145(7):1012–1022, 2011. (Cited on page 1.)

THOMAS M Roberts, S Sepsenwol, and HANS Ris. Sperm motility in nematodes: Crawling movement without actin. 1989. (Cited on page 7.)

Douglas N Robinson and James A Spudich. Mechanics and regulation of cytokinesis. *Current opinion in cell biology*, 16(2):182–188, 2004. (Cited on page 2.)

Stéphane Romero, Christophe Le Clainche, Dominique Didry, Coumaran Egile, Dominique Pantaloni, and Marie-France Carlier. Formin is a processive motor that requires profilin to accelerate actin assembly and associated atp hydrolysis. *Cell*, 119(3):419–429, 2004. (Cited on page 9.)

Juha Saarikangas, Hongxia Zhao, and Pekka Lappalainen. Regulation of the actin cytoskeleton-plasma membrane interplay by phosphoinositides. *Physiological reviews*, 90(1):259–289, 2010. (Cited on page 91.)

E Sackmann. Physical basis of self-organization and function of membranes: physics of vesicles. *Handbook of Biological Physics*, 1:213–304, 1995. (Cited on page 74.)

Takeshi Sakamoto, John Limouze, Christian A Combs, Aaron F Straight, and James R Sellers. Blebbistatin, a myosin ii inhibitor, is photoinactivated by blue light. *Biochem.*, 44(2):584–588, 2005. (Cited on page 40.)

Guillaume Salbreux, Guillaume Charras, and Ewa Paluch. Actin cortex mechanics and cellular morphogenesis. *Trends Cell Biol.*, 22(10):536–545, 2012. (Cited on pages 37 and 73.)

Dorothy A Schafer. Cell biology: barbed ends rule. *Nature*, 430(7001):734–735, 2004. (Cited on page 5.)

Dorothy A Schafer, Phillip B Jennings, and John A Cooper. Dynamics of capping protein and actin assembly in vitro: uncapping barbed ends by polyphosphoinositides. *The Journal of Cell Biology*, 135(1):169–179, 1996. (Cited on page 8.)

K. M. Schmoller, O. Lieleg, and A. R. Bausch. Internal stress in kinetically trapped actin bundle networks. *Soft Matter*, 4:2365 – 2367, 2008. (Cited on page 80.)

K. M. Schmoller, O. Lieleg, and A. R. Bausch. Structural and viscoelastic properties of actin/filamin networks: Cross-linked versus bundled networks. *Biophys. J.*, 97:83–89, 2009. (Cited on page 65.)

Matthias Schuppler, Keber Felix, Kroeger Martin, and Bausch Andreas. Boundaries steer the contraction of active gels. *Nature Communications*, 2016. (Cited on page 40.)

U Seifert and R Lipowsky. Morphology of vesicles. *Handbook of biological physics*, 1:403–464, 1995. (Cited on page 74.)

M Sheinman, A Sharma, J Alvarado, GH Koenderink, and FC MacKintosh. Active biopolymer networks generate scale-free but euclidean clusters. *arXiv preprint arXiv:1402.2623*, 2014. (Cited on page 38.)

M. Sheinman, A. Sharma, J. Alvarado, G. H. Koenderink, and F. C. MacKintosh. Anomalous discontinuity at the percolation critical point of active gels. *Phys. Rev. Lett.*, 114:098104, 2015. (Cited on page 37.)

David Smith, Falko Ziebert, David Humphrey, Cynthia Duggan, Matthias Steinbeck, Walter Zimmermann, and J Käs. Molecular motor-induced instabilities and cross linkers determine biopolymer organization. *Biophysical journal*, 93 (12):4445–4452, 2007. (Cited on page 3.)

J. A. Spudich and S. Watt. Regulation of rabbit skeletal muscle contraction .1. biochemical studies of interaction of tropomyosin-troponin complex with actin and proteolytic fragments of myosin. *J. Biol. Chem.*, 246:4866–71, 1971. (Cited on page 7.)

Dietrich Stauffer and Ammon Aharony. *Introduction to percolation theory*. CRC press, 1994. (Cited on page 38.)

Patrick RH Steinmetz, Johanna EM Kraus, Claire Larroux, Jörg U Hammel, Annette Amon-Hassenzahl, Evelyn Houliston, Gert Wörheide, Michael Nickel,

Bernard M Degnan, and Ulrich Technau. Independent evolution of striated muscles in cnidarians and bilaterians. *Nature*, 487(7406):231–234, 2012. (Cited on page 1.)

Olle I Stendahl and Thomas P Stossel. Actin-binding protein amplifies actomyosin contraction, and gelsolin confers calcium control on the direction of contraction. *Biochemical and biophysical research communications*, 92(2):675–681, 1980. (Cited on page 69.)

Yohko Tanaka-Takiguchi, Toshihito Kakei, Akinori Tanimura, Aya Takagi, Makoto Honda, Hirokazu Hotani, and Kingo Takiguchi. The elongation and contraction of actin bundles are induced by double-headed myosins in a motor concentration-dependent manner. *Journal of molecular biology*, 341(2):467–476, 2004. (Cited on page 69.)

Todd Thoresen, Martin Lenz, and Margaret L Gardel. Reconstitution of contractile actomyosin bundles. *Biophysical journal*, 100(11):2698–2705, 2011. (Cited on page 60.)

Todd Thoresen, Martin Lenz, and Margaret L Gardel. Thick filament length and isoform composition determine self-organized contractile units in actomyosin bundles. *Biophysical journal*, 104(3):655–665, 2013. (Cited on pages 2, 37, and 59.)

Jean-Yves Tinevez, Ulrike Schulze, Guillaume Salbreux, Julia Roensch, Jean-François Joanny, and Ewa Paluch. Role of cortical tension in bleb growth. *Proceedings of the National Academy of Sciences*, 106(44):18581–18586, 2009. (Cited on page 73.)

Simon F Tolić-Nørrelykke, Erik Schäffer, Jonathon Howard, Francesco S Pavone, Frank Jülicher, and Henrik Flyvbjerg. Calibration of optical tweezers with positional detection in the back focal plane. *Review of scientific instruments*, 77 (10):103101, 2006. (Cited on page 20.)

Qingzong Tseng, Eve Duchemin-Pelletier, Alexandre Deshiere, Martial Balland, Hervé Guillou, Odile Filhol, and Manuel Théry. Spatial organization of the

extracellular matrix regulates cell–cell junction positioning. *Proc. Natl. Acad. Sci.*, 109(5):1506–1511, 2012. (Cited on page 13.)

Ernst J Ungewickell and Lars Hinrichsen. Endocytosis: clathrin-mediated membrane budding. *Current opinion in cell biology*, 19(4):417–425, 2007. (Cited on page 2.)

Taro QP Uyeda, Stephen J Kron, and James A Spudich. Myosin step size: estimation from slow sliding movement of actin over low densities of heavy meromyosin. *Journal of molecular biology*, 214(3):699–710, 1990. (Cited on page 10.)

Dimitrios Vavylonis, Jian-Qiu Wu, Steven Hao, Ben O'Shaughnessy, and Thomas D Pollard. Assembly mechanism of the contractile ring for cytokinesis by fission yeast. *Science*, 319(5859):97–100, 2008. (Cited on page 2.)

D. Vignjevic, D. Yarar, M.D. Welch, J. Peloquin, T. Svitkina, and G.G. Borisy. Formation of filopodia-like bundles in vitro from a dendritic network. *J. Cell Biol.*, 160(6):951–962, 2003. (Cited on page 8.)

D. Vignjevic, S. Kojima, Y. Aratyn, O. Danciu, T. Svitkina, and G. G. Borisy. Role of fascin in filopodial protrusion. *J. Cell Biol.*, 174(6):863–785, 2006. (Cited on page 8.)

R Waugh and EA Evans. Thermoelasticity of red blood cell membrane. *Biophysical journal*, 26(1):115, 1979. (Cited on page 76.)

Manuela Weitkunat, Aynur Kaya-Çopur, Stephan W Grill, and Frank Schnorrer. Tension and force-resistant attachment are essential for myofibrillogenesis in drosophila flight muscle. *Current Biology*, 24(7):705–716, 2014. (Cited on pages 4 and 57.)

Cyrus A Wilson, Mark A Tsuchida, Greg M Allen, Erin L Barnhart, Kathryn T Applegate, Patricia T Yam, Lin Ji, Kinneret Keren, Gaudenz Danuser, and Julie A Theriot. Myosin ii contributes to cell-scale actin network treadmilling through network disassembly. *Nature*, 465(7296):373–377, 2010. (Cited on page 60.)

Patricia T Yam, Cyrus A Wilson, Lin Ji, Benedict Hebert, Erin L Barnhart, Natalie A Dye, Paul W Wiseman, Gaudenz Danuser, and Julie A Theriot. Actin–myosin network reorganization breaks symmetry at the cell rear to spontaneously initiate polarized cell motility. *The Journal of cell biology*, 178(7):1207–1221, 2007. (Cited on page 70.)

Shigenobu Yonemura. Cadherin–actin interactions at adherens junctions. *Current opinion in cell biology*, 23(5):515–522, 2011. (Cited on page 4.)

Li Zhang and Amy Shaub Maddox. Anillin. *Current Biology*, 20(4):R135–R136, 2010. (Cited on page 8.)

F Ziemann, J Rädler, and E Sackmann. Local measurements of viscoelastic moduli of entangled actin networks using an oscillating magnetic bead micro-rheometer. *Biophysical Journal*, 66(6):2210, 1994. (Cited on page 35.)

Sally H Zigmond, Hyam I Levitsky, and Barbara J Kreel. Cell polarity: an examination of its behavioral expression and its consequences for polymorphonuclear leukocyte chemotaxis. *The Journal of cell biology*, 89(3):585–592, 1981. (Cited on page 70.)

Danksagung

Abschließend möchte ich mich ganz herzlich bei all jenen bedanken, die zum Gelingen dieser Arbeit beigetragen und mich auf unterschiedliche Weise begleitet und unterstützt haben:

... Prof. Andreas Bausch für die Möglichkeit in seiner Arbeitsgruppe promovieren zu dürfen.

... Allen, die unmittelbar an den Projekten dieser Dissertation beteiligt waren, für die produktive Zusammenarbeit: Felix Keber, Etienne Loiseau, Carina Pelzl und Prof. Martin Kröger.

... meinen Werkstudenten und Bacheloranden: Vincent Maier, Ariane Leone und Moritz Thiele

... Beim gesamten E27-Personal der letzten 6 Jahre für die freundschaftliche Arbeitsatmosphäre: Christine, Simone, Volker, Jona, Kurt, Uli, Heinrich, Markus, Sebastian, Martina, Carina, Felix, Etienne, Leo, Joanna, Katharina, Matthias, Pablo, Bernhard, Fabian, Henri, Ben, ... für Euere Hilfsbereitschaft, die konstruktiven Diskussionen, die Exkursionen, etwa in den Biergarten oder zum Squashen.

... Den TAs: Monika Rusp, Gabriele Chmel, Karin Vogt und Thi-Hieu Ho für die kontinuierliche Unterstützung im Labor, die diversen Proteinpräparationen und das beste Aktin.

... Den Sekretärinnen, Katerina Girgensohn, Iris König-Decker, Katharina Scholz, Nicole Mittermüller, Elke Fehsenfeld, Anne Ploß für die unbürokratische Hilfe im Bürokratiedschungel.

... Allen meinen Bürokollegen für das Teilen von lustigen, ernsten, faktischen, phantastischen, zukünftigen, vergangenen und kulinarischen Geschichten.

... Kurt und Benni für das regelmäßige Anrichten des blutigen Würmerchaos.

... Den Kaffeefeen (Markus, Christina, Uli, Sonja und Fabi), für die gewährleistete Versorgung mit Energieelixier.

... Marco, Etienne, Joanna und Leone fürs Korrekturlesen.

... IGSSE für die finanzielle Unterstützung.

... meinen Eltern, die mich und meine kleine Familie seit jeher liebevoll begleiten und schützen.

... meiner Frau Barbara und meinen Kindern Emil und Mathilda: Ihr seid die beste Familie, die ich mir wünschen und vorstellen kann. Vielen Dank für die ausdauernde und motivierende Unterstützung, für das Fernhalten von vielerlei Problemen des Alltags, für das Aushalten meiner geistigen Abwesenheit und des Rückhalts trotz der gegen Ende prekären wirtschaftlichen Verhältnisse. Ich liebe Euch!